Ministry of Higher Education and Scientific Research
University of Baghdad
Institute of Laser for Postgraduate Studies

Investigation of the influence of the Plateau-Rayleigh instability in fibre drawn indium-PMMA metamaterial

A Thesis

Submitted to the Institute of Laser for Postgraduate Studies, University of Baghdad in Partial Fulfillments for the Requirements for the Degree of Doctor of Philosophy in Laser/Electronics and Communication Engineering

by

Ahmed Abd Al-Kareem Ali Al-Chalaby

B.Sc. Laser and Optoelectronics Engineering 2005

M.Sc. Laser and Optoelectronics Engineering 2008

Supervised by

Prof. Abdul-Hadi M. Al-Janabi

1436 AH **2015 AD**

Certification

I certify that this thesis was prepared under my supervision at the institute of laser for postgraduate studies, university of Baghdad as a partial requirement for the Degree of a Doctor of Philosophy of laser.

Signature

Name: Dr. Abdul Hadi M. Al-Janabi

Title: Professor

Address: The Institute of Laser for Postgraduate Studies,

University of Baghdad

Date: / / 2015

(Supervisor)

In view of a available recommendation, I forward this thesis for debate by the examination committee.

Signature:

(Advisor): Dr. Shelan Khasro Tawfeeq

Title: Asst. Professor

Address: Head of Scientific Committee

Institute of Laser for Postgraduate Studies,

University of Baghdad

Date: / / 2015

بِسْمِ اللهِ الرَّحْمنِ الرَّحِيم

وَيَرَى الَّذِينَ أُوتُوا الْعِلْمَ
الَّذِي أُنزِلَ إِلَيْكَ
مِن رَّبِّكَ هُوَ الْحَقَّ وَيَهْدِي
إِلَى صِرَاطِ الْعَزِيزِ الْحَمِيدِ

صَدَقَ اللّهُ الْعَلِيُّ الْعَظِيم

{ سبأ٦}

Dedication

I would like to dedicate my Thesis to

my parents and family

Acknowledgement

The first thanking is to the first giver "glorious ALLAH"

I would like to express my deep gratitude to my supervisor, **Prof. Dr. Abdul Hadi M. Al-Janabi** for his continuous help and encouragement during the research period. My grateful thanks go to all the faculty members of the institute of laser for postgraduate studies in university of Baghdad, especially **Prof. Khalil Ibrahim Hajim, Prof. Mazin M. Elias** and **Dr. Hussein A. Jawad,** for their valuable suggestions and advices.

Special thanks to **Prof. Raad Sami Fyath**, College of engineering, Nahrain University, and **Dr. Ziad Ayad Taha**, Head of the engineering and industrial application dept. ILPS for their support during my research work.

Special thanks to **Ministry of Higher Education and Scientific Research- Iraq** for giving the opportunity to visit University of Sydney and doing a part of this work through funded research fellowship

I am indebted to the Institute of Photonics and Optical Science (IPOS), The university of Sydney, for their approval to register me as a visiting researcher. Especially, I would like to express my deep appreciation to **Assist Prof. Alexander Argyros**, for the outstanding effort that he made to provide me with whatever was needed to finish this work; his support and guidance is extraordinary. I would like also to thank the other group members **Boris T. Kuhlmey, Richard Lwin, Alessandro Tuniz, Simon C. Fleming;** they were great colleagues.

I would like to extend my gratitude to all my friends and colleagues in the institute of laser for postgraduate studies. Finally I am indebted to my wife and family who were very patient and encouraging during all the period of my study.

Ahmed Abd Al-kareem Ali Al-Chalaby

December 2014

Abstract

Metamaterial is a synthetic composite material with a structure such that it exhibits properties not usually found in natural materials. Fibre drawing method has been used in producing Poly-methyl methacrylate (PMMA)-indium wires metamaterials. PMMA and indium are having relatively the same glass transition temperature making them suitable for co-drawing. The fiber filaments must be drawn to smaller diameters to shift the metamaterials response to higher frequency. At these dimensions the metal filaments inside the fiber become unstable and break-up at random intervals. This instability is due to a phenomenon known as the Plateau-Rayleigh Instability

Well known Tomotika model for the growth in the varicosity in the surface of fluid extended inside another fluid was modified to describe the fluctuations (instability) of inner core diameter for metamaterials drawing inside radiative furnace. Modified Tomotika model was used to investigate the instability growth of the indium wire diameter produced by co-drawing of indium metal embedded in a PMMA polymer.

The critical parameter for the wire breaks is the wavelength of perturbations. A MATLAB model was used to describe a small drawing ratio (neglecting the wavelength of fluctuations effect). The experimental and modeling results are almost match when a very small temperature variation occurred. So the observed fluctuations in diameter can be reconciled with the Plateau-Rayleigh instability.

For larger fluctuations (large drawing ratio) the wavelength of fluctuations was analyzed and sequential breakup on different length scales was observed. We infer limits to wire dimensions that can be

achieved using the chosen material system and identify a path for extending drawing methods to fabricate smaller wires.

Finally, simulation for deep subwavelength wave propagation inside wire metamaterials depending on the unit cell manipulation was performed. CST microwave studio software had been used to simulate wave propagation inside linear and 90° corner waveguide as well as equal arms beam splitter (50/50). It's applicable to waveguiding 40cm wavelength in about 2.4 cm waveguide.

List of Contents

Abstract

List of Symbols

Symbols	Description	Units
λ	Wavelength	m
E	Electric field vector	V/m
H	Magnetic field vector	A/m
ε_o	Permittivity of free space = $8.85*10^{-12}$	F/m
μ_0	Permeability of free space = $4\pi*10^{-7}$.	H/m
ε	*Permittivity* of the medium	F/m
μ	*Permeability* of the medium	H/m
ε_r	Relative permittivity	
μ_r	Relative permeability	
σ	Conductivity of the material	S/m
D	Electric flux density	C/m^2
B	Magnetic flux density	T
ρ	**C**harge density	C/m3
J	Current density	A/m^2
P	Vector sum of the electric dipole moments per unit volume	
M	Vector sum of the magnetic dipole moments per unit volume	
ω_p	Plasma frequency	rad
c	Speed of light $=3*10^8$	m/s
Tg	Glass Transition Temperature	C
a_0	Initial radius of the inner fluid	m
a	Radius of inner fluid	m
$\bar{\varepsilon_0}$	Initial amplitude of perturbation	m
$\bar{\varepsilon_0}$	Amplitude of perturbation	m
λ_0	Initial wavelength of perturbation	m
λ_{final}	Final wavelength of perturbation	m
n	Rate of Growth	1/s
$f(t)$	Arbitrary function of time	
$g(z)$	Arbitrary function of position	

List of Abbreviations

PMMA	Poly(methyl methacrylate)
PCs	Photonic Crystals
PBG	Photonic Band Gap
EBL	Electron-Beam Lithography
FIB	Focused Ion Beam
NIL	Nanoimprint Lithography
IL	Interference Optical Lithography
DLW	Direct Laser Writing
SEM	Scanning Electron Microscope
LIFT	Laser-Induced Forward Transfer
CST	Computer Simulation Technology

List of Figures

List of Tables

CHAPTER ONE: Theoretical Concept

1.1 Introduction

Metamaterial is an artificial composite material designed to control and manipulate the flow of electromagnetic or acoustic waves. It is made up of periodic arrays of metallic resonant elements. Both the size of the element and the unit cell are small relative to the wavelength. Electromagnetic properties of metamaterial owing to their unit cell structure rather than its composition materials [1].

The subwavelength structures allow the realization of many new and unusual optical properties such as magnetism at optical frequency, negative refractive index, large possible refractive index, perfect absorption [2].

The requirement of sub-wavelength structure creates difficulties in the fabrication of large volumes of metamaterials, specifically as shorter wavelengths are considered – for microwaves, millimetre-scale structures are sufficient [3], whilst heading into the optical and UV, structure on 10-100 nm scale is required [4,5].

Recently, group on the IPOS, University of Sydney, were using fiber drawing as a novel way of inexpensively producing large amounts of metamaterials [6]. The fabrication of metamaterials with response at higher frequencies, like further into the mid-IR, near-IR and the visible, becomes more difficult but of interest. The structure should be minimized by e.g. reducing the wire diameter and the spacing between wires[7]. For the fibre drawing method, the fiber filaments should be drawn to smaller diameters. Through the drawing process, a liquid phase is presented. The

metal-PMMA preform may shows a break up during drawing for submicron range. This instability is due to a phenomenon known as the Plateau-Rayleigh instability addressed in 1935 by Tomotika [8] for a long cylindrical column of an incompressible viscous fluid surrounded by another viscous fluid. A direct consequence of this uncontrolled break-up is the inability to effectively control the permittivity and permeability of the produced metamaterials.

1.2 Natural and Artificial Materials

Natural materials are made up by lots and lots of small elements like atoms and molecules. Some of these materials are amorphous, others are crystalline[9]. The main interest in optical materials in general and in metamaterials is in the interplay of waves and materials which is restricted to classical physics. The key parameter is a/λ, where a is the distance between elements in the material and λ is the free-space wavelength.

If the wavelength λ is highly longer than a the properties of interaction can be described by geometrical optics and ray tracing. When the wavelength λ is comparable with the a, Bragg effect comes into play. The wave is scattered in a specular fashion by the atoms in the system, and undergo constructive interference in accordance to Bragg's law. For a crystalline solid, the waves are scattered from lattice planes separated by the interplanar distance d, where the scattered waves interfere constructively. They remain in phase since the path length of each wave equals to an integer multiple of the wavelength. The path difference

between two waves undergoing constructive interference is given by $2d\sin\theta$, where θ is the scattering angle[10].

In another side when the wavelength is much larger than the lattice period. Then no such dramatic effect occurs, but it is nonetheless significant. There may not be major reflection or diffraction but the electromagnetic wave is still considerably affected when it enters a material. One may then ignore the details and pretend that there is no discrete structure: the material is homogeneous and continuous. The aim is then to find some effective parameters like electric permittivity ε and magnetic permeability μ. This is known as the effective-medium approximation[11].

In the case of artificial materials in which atoms and molecules are replaced by macroscopic, man-made, elements. Now, all dimensions are larger than in natural materials but the division into the above two categories (discrete, homogeneous) is still valid. When the separation between the elements a is comparable with the wavelength λ Bragg effect is dominated. When the separation is much smaller than the wavelength can be resort to effective-medium theory. Photonic bandgap materials relies in the former case [9] and metamaterials relies in the latter case [12], as shown in figure (1.1)

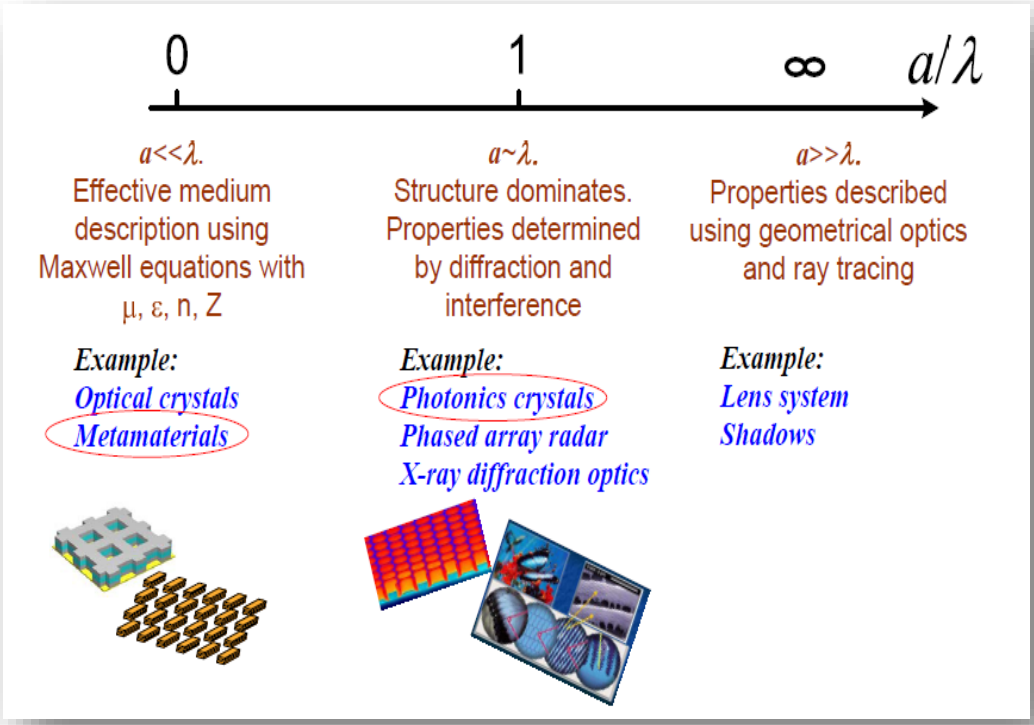

Figure (1.1) Analogy of wave-crystal interaction with respect to a/λ [13]

1.3 Theoretical aspect of metamaterials

Metamaterials can be characterized by using Maxwell's equations**.** Maxwell's equations are a set of partial differential equations that describe how electric and magnetic fields are generated and altered by each other and by charges and currents inside the matter. They are named after the Scottish physicist and mathematician James Clerk Maxwell, who published an early form of those equations between 1861 and 1862. Maxewll's equation for Electromagnetic wave interaction with matter [11]:

$$\nabla \times \boldsymbol{E} = -\frac{\partial \boldsymbol{B}}{\partial t} \tag{1.1a}$$

$$\nabla \times \boldsymbol{H} = \frac{\partial D}{\partial t} + \boldsymbol{J} \tag{1.1b}$$

$$\nabla . \boldsymbol{B} = 0 \tag{1.1c}$$

$$\nabla . \boldsymbol{D} = \rho \tag{1.1d}$$

Where **E:** Electric field vector, **H:** Magnetic field vector, **D**=Electric flux density, **B**=Magnetic flux density, ρ=charge density [C/m^3] and **J**=current density [A/m^2]. When an electromagnetic field is applied to material media, the phenomena of conduction, polarization, and magnetization occur [14]. Polarization causes the appearance of aligned electric dipole moments or a bound charge density. Magnetization is the appearance of aligned magnetic dipole moments or a molecular current density.

**Total electric flux density = Flux from external E-field + flux due to material polarization*

$$\boldsymbol{D} = \varepsilon_o \boldsymbol{E} + \boldsymbol{P}(\boldsymbol{E}) \tag{1.2}$$

**Total magnetic flux density = Flux from external H-field + flux due to material magnetization*

$$\boldsymbol{B} = \mu_o \boldsymbol{H} + \boldsymbol{M}(\boldsymbol{H}) \tag{1.3}$$

where $\boldsymbol{P}$ is the vector sum of the electric dipole moments per unit volume and $\boldsymbol{M}$ is the vector sum of the magnetic dipole moments per unit volume. ε_o: permittivity of free space = 8.85*10^{-12} [F/m], μ_0= permeability of free space = 4π*10^{-7}H/m. For non-dispersive, linear and isotropic media (simple media) where vector $\boldsymbol{P}$ is parallel to and proportional to vector $\boldsymbol{E}$ and vector $\boldsymbol{M}$ is parallel to and proportional to vector $\boldsymbol{B}$, the relationships can be expressed as follows:

$$\boldsymbol{P} = \varepsilon_o \chi_e \boldsymbol{E} \tag{1.4}$$

$$\boldsymbol{M} = \mu_o \chi_m \boldsymbol{H} \tag{1.5}$$

where χ_e is the electric susceptibility and χ_m is the magnetic susceptibility of the medium, both of which are dimensionless quantities. Substituting (1.4) and (1.5) into (1.2) and (1.3), respectively, we have

$$\boldsymbol{D} = \varepsilon_o(1+\chi_e)\boldsymbol{E} = \varepsilon_o\varepsilon_r\boldsymbol{E} \quad \text{or} \quad \boldsymbol{D} = \varepsilon\boldsymbol{E} \tag{1.6}$$

$$\boldsymbol{B} = \mu_o(1+\chi_m)\boldsymbol{H} = \mu_o\mu_r\boldsymbol{H} \quad \text{or} \quad \boldsymbol{B} = \mu\boldsymbol{H} \tag{1.7}$$

In the above equations,

$$\varepsilon_r = 1+\chi_e, \qquad \varepsilon = \varepsilon_o\varepsilon_r = \varepsilon_o(1+\chi_e) \tag{1.8}$$

$$\mu_r = 1+\chi_m, \qquad \mu = \mu_o\mu_r = \mu_o(1+\chi_m) \tag{1.9}$$

where ε is the permittivity, μ is the permeability of the medium, and ε_r and μ_r are the relative permittivity and relative permeability, respectively.

Substitute (1.8), (1.9) in (1.1) and for sinusoidal excitation

$$\nabla \times \boldsymbol{E} = -j\omega\mu\boldsymbol{H} \tag{1.10a}$$

$$\nabla \times \boldsymbol{H} = j\omega\varepsilon\boldsymbol{E} + \boldsymbol{J} \tag{1.10b}$$

$$\nabla.\boldsymbol{B} = 0 \tag{1.10c}$$

$$\nabla.\boldsymbol{D} = \rho \tag{1.10d}$$

For the plane wave eq. (1.10) can be reduced to [15]

$$\boldsymbol{K} \times \boldsymbol{E} = \omega\mu\boldsymbol{H} \tag{1.11a}$$

$$\boldsymbol{K} \times \boldsymbol{H} = -\omega\varepsilon\boldsymbol{E} \tag{1.11b}$$

Therefore for positive ε and μ, $\boldsymbol{E}$, $\boldsymbol{H}$ and $\boldsymbol{K}$ (Wave Vector) form a right handed orthogonal system. When ε and μ are negative eq. (1.10) becomes

$$\boldsymbol{K} \times \boldsymbol{E} = -\omega\mu\boldsymbol{H} \tag{1.12a}$$

$$\boldsymbol{K} \times \boldsymbol{H} = \omega\varepsilon\boldsymbol{E} \tag{1.12b}$$

Which shows left handed material and their opposite direction and left handed triplet of ***E***, ***H*** and ***K.***

1.4 Types of metamaterials

Since the response of a material to external fields is largely determined only by the two material parameters μ and ε, one can use an electromagnetic parameter space to classify materials based on the two values [16]. As shown in figure (1.2), the real part of permittivity ε_r is plotted to the horizontal axis of the parameter space, while the vertical axis corresponds to the real part of permeability μ_r. Therefore materials with all possible combinations of ε_r and μ_r can be placed in the parameter space.

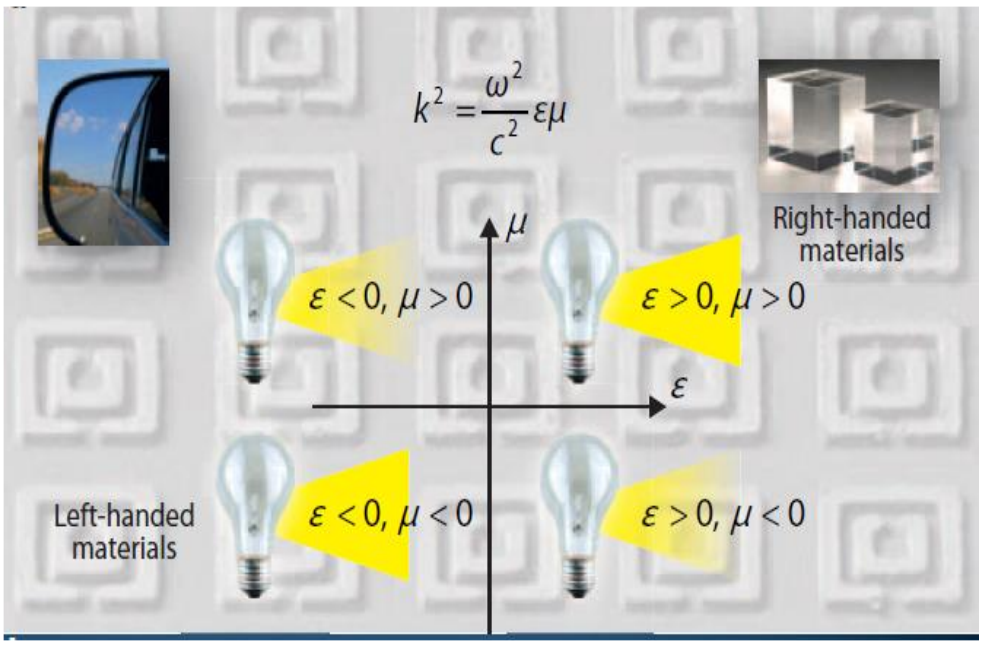

Figure (1.2) Regions of possible permittivity (*ε*) and permeability (*μ*), showing normal refraction (top right) and negative refraction (bottom left). [12].

Conventional materials known to be transparent are found in the first quadrant, where both ε_r and μ_r have positive values. A negative value of

ε(μ) indicates that the direction of the electric (magnetic) field induced inside the material is in the opposite direction to the incident field. Noble metals at optical frequencies are good examples for materials with negative ε and negative μ can be found in ferromagnetic media near a resonance [17]. No propagating waves can be supported in materials represented by the second and fourth quadrants, where one of the two parameters is negative and the index of refraction becomes purely imaginary [16].

1.5 Electric Response Metamaterials

The electric response of a medium was described by using its electric permittivity ε, so the main purpose of studying electric metamaterials is to create artificial metal-dielectric structures that possess a permittivity of a desired value at the given frequency[11]. The wire medium (or the rodded medium) consisting of a two-dimensional (2D) or three dimensional (3D) rectangular lattice of low-loss wire grids (Figure 1.3) has been known for a long time, and it has been extensively studied in microwave lens design [18-20] and for the synthesis of surface reactance [21].

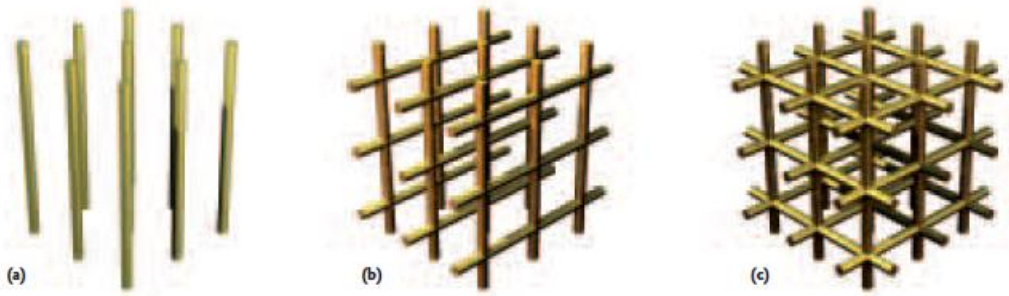

Figure (1.3) Wire media. (a) 2D lattice (a single WM), electric field in *z*-direction. (b) 3D lattice (a double WM), electric field in *y*−*z* plane. (c)Three-dimensional lattice (a triple WM), arbitrary polarization [11].

Wires at microwaves can be considered with high accuracy to be perfectly electrically conducting (PEC). A simple wire medium of PEC wires was considered a uniaxial material without spatial dispersion. The relative permittivity tensor of a simple wire medium was presented in the form [22]:

$$\bar{\bar{\varepsilon}} = \begin{pmatrix} \varepsilon_{xx} & 0 & 0 \\ 0 & \varepsilon_t & 0 \\ 0 & 0 & \varepsilon_t \end{pmatrix}, \quad \varepsilon_{xx} = \varepsilon_h (1 - \frac{k_p^2}{k^2}) \tag{1.13}$$

Here axis x is chosen in parallel to the wires, ε_h is the host medium permittivity, k is the wave number of the host medium, and $k_p = \omega_p / c$ is the wave number corresponding to the plasma frequency ω_p that gives grounds to call the wire medium as "artificial plasma". Different models exist for the plasma frequency, as will discussed later

Interest in wire media was renewed at the end of the last decade in connection with engineering of materials with negative parameters, sometimes called double-negative materials (DNM). The first DNM proposed by Smith et al. consists of a lattice of long metal strips and split-ring resonator [23]. Now the wire medium is a commonly used component of artificial metamaterials for microwave and optical applications [24]. Despite the conventional Drude formula eq. (1.13) examined experimentally in early works, only waves propagating normally to the wires were investigated. However, it has been shown that if the wave vector in a wire medium has a nonzero component along the wires, equation (1.13) gives nonphysical results [25]. The plasma model has been corrected introducing terms describing the spatial dispersion (SD) into eq. (1.13)

1.5.1 Plasma Frequency for Wire Media

As mentioned before the Drude formula (Eq. 1.13) for effective permittivity leads to unphysical results and must be substituted by a nonlocal dispersive relation. The plasma frequency corresponding to collective oscillations of electron density is expressed as [25].

$$\omega_p^2 = \frac{ne^2}{\epsilon_o m_{eff}} \qquad \text{[rad/s]} \qquad (1.14)$$

where n, e, and m_{eff} are the density, charge, and effective mass of the electron, respectively. For metals ω_p typically is in the ultraviolet region. It seems to be reasonable to reduce the plasma frequency to the microwave range cutting thin wires, forming a 2D periodic structure, from a bulk metal. Then we obtain collective oscillations of electrons along wires. The density of these active electrons will be

$$n_{eff} = n\frac{\pi r^2}{a^2} \qquad \text{[rad/m]} \qquad (1.15)$$

where a and r are the lattice constant and radius of a wire, respectively. It turned out that in contrast to the case of natural plasma, a restoring force acting on the electron not only has to work against the rest mass of the electrons but also against self-inductance of the wire structure [26]. Moreover, the effect of self-inductance considerably exceeds the effect of the rest mass, and one can neglect the last one for high-conductive metals in the microwave range. After that both the electron density and the effective mass drop from the final expression for the plasma frequency. The most generally used formulas for the plasma frequency were proposed in [26-28].

In his derivative Pendry [26] didn’t not take into account interaction between the wires

$$k_p^2 = \frac{2\pi}{a^2 \ln(a/r)} \tag{1.16}$$

While Blove et al. [27] were derived formula from consideration of wire metamaterials as a photonic crystal

$$k_p^2 = \frac{2\pi}{a^2(\ln(a/2\pi r))+0.5275} \tag{1.17}$$

Finally Masloviski et al. [28] were derived their formula using a quasistatic model

$$k_p^2 = \frac{2\pi}{a^2} \frac{1}{\ln(a^2/4r(a-r))} \tag{1.18}$$

Figure (1.4) illustrates comparison between the f_p, calculated using different formulas for thin wires ($r/a < 0.1$) and $a = 1$ cm.

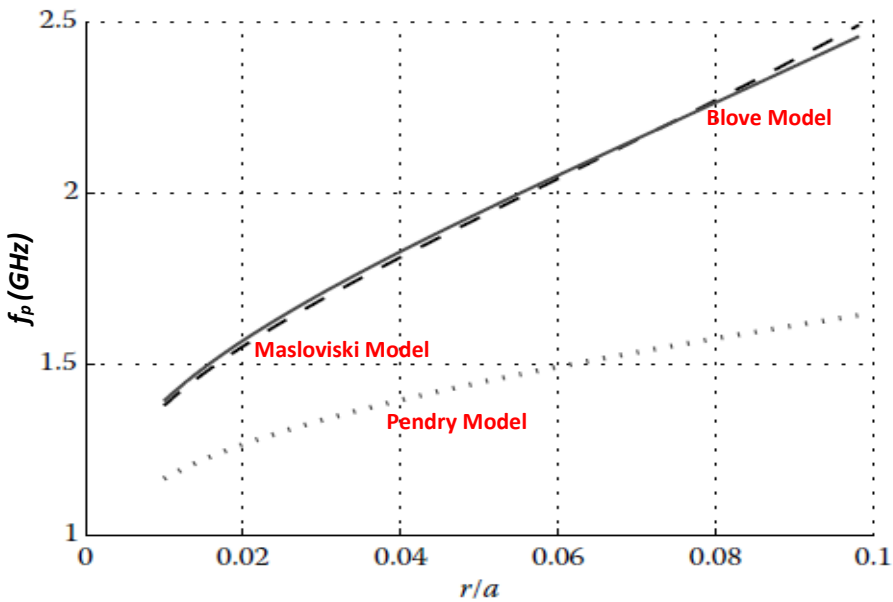

Figure (1.4) Plasma frequency f_p in GHz, calculated using Pendry model: dotted line, Blove model: solid line, Masloviski: dashed line [29]**.**

1.6 Metamaterials Applications

Despite all the differences between the electromagnetic behavior of ordinary materials and metamaterials, they are both governed by the same set of Maxwell equations. Therefore, it is the new functionalities and

design guidelines enabled by the metamaterial paradigm—rather than new physics—that have aroused a relentless interest in metamaterials. This interest remains equally strong from both the physics and engineering communities since the field of metamaterials mediates science and technology. It is therefore not surprising that in recent years we have witnessed a rapidly escalating number of publications on the physics, design, and applications of various types of metamaterials [30].

1.6.1 Metamaterials antenna

Metamaterial coatings have been used to enhance the radiation and matching properties of electrically small electric and magnetic dipole antennas [31]. Patch antenna with metamaterial cover have increased directivity [32] . Also metamaterial can enhance the gain and reduce the return loss of a patch antenna [33]. Flat horn antenna with flat aperture constructed of zero index metamaterial has advantage of improved directivity [34]. Because a signal Propagating in a zero-index metamaterial will stimulate a spatially static field structure that varies in time; the phase at any point in a zero-index metamaterial will have the same constant value once steady state is reached [15].

1.6.2 Metamaterials sensing

One of the most intriguing possibility offered by metamaterials is the large flexibility in their dispersion engineering properties, which may provide novel tools to significantly enhance the sensitivity of practical devices [35].

1.6.2.1 Biosensor

Biosensors are essential in many areas, such as disease diagnostics, environmental monitoring, and food safety. Fluorescence-based methods have proven useful in analyzing both genomic and proteomic microarrays. However, labeling molecules with fluorophores can be expensive and time-consuming. It may even be infeasible for certain applications. Recently, biosensing technologies based on metamaterials have attracted significant attentions from the microwave to optical frequency because of their cost-efficient and label-free biomolecule detection [35] .

1.6.2.2 Planar Waveguide Sensor

Waveguide sensors have found a wide range of applications such as the detection of harmful gases [36]. Such sensors are also known as evanescent wave sensors because of the evanescent wave entering into the analyte whose refractive index is to be measured. The amplification of evanescent wave forms the basis for increasing the sensitivity. Through inserting a layer of metamaterials with negative permittivity and negative permeability between the cladding and the guiding layer, they found that the sensitivity of the waveguide sensor can be dramatically enhanced [37]

1.6.2.3 Thin-Film Sensor

Thin-film sensing utilizing interaction between electromagnetic waves and unidentified thin-film sample substance can provide important information for many chemical and biological applications. To achieve efficient thin-film sensing, some thin-film sensors based on metamaterials are proposed and fabricated [38,39]. For example, the Frequency-

Selective Surfaces (FSS) metamaterials consisting of periodic two-dimensional arrays of identical resonators, have arisen as candidates for highly sensitive chemical or biological thin film detection because it can be small and show a resonant frequency response that is tunable by design [35,40].

1.6.3 Metamaterials Filter

There are a number of resonator types that can be useful in RF and microwave filter applications. The favored resonator types that can be of use are cavity resonators, dielectric resonators, lumped element resonators, transmission line resonators and semi-lumped resonators [41]. Chang [42] recommended that the perfect examples of such microwave applications are filters where the transmission line resonators can be effectively used. The frequency selectivity of resonant-type metamaterial transmission lines suggests their application in filter design. Furthermore, the possibility of obtaining such broad responses by means of balanced lines opens the door to the application of these structures in the design of broad-band filters [43]. M. Gil et al. suggested that Characteristic impedance and phase shift are among the chief properties of such transmission lines [44]. As an example, In 2007 Li Jiusheng proposed, a new kind of a left handed metamaterial unit cell based on microstrip technology [45]. The metamaterial unit cell is a combination of a series microstrip gap and a hole for the series capacitor and the shunt inductor, respectively. By using the metamaterial unit cell, a new structure band pass filter is designed and fabricated. The newly developed band pass filter gain the advantages of low transmission loss, high return loss, and low fabrication cost. Recently, Naima Benmostefa et.al [46] were successfully

designed a tunable stop band filters. They presented a new concept to implement a tunable filter metamaterial with dual negative refraction composed of ferrite slabs and metallic resonators, including Split-Ring Resonators (SRR), and short wire pairs. The ferrite slabs under an applied magnetics bias provide one magnetic resonance frequency band and the metallic resonators provide another one. The continuous wires within the metamaterials provide the negative permittivity in a wide frequency band covering the two magnetic resonance bands [46].

1.6.4 Metamaterial Waveguide

Since optical waveguides play an important role in many fundamental studies of optical physics and in exciting applications in optical communications, optical waveguides based on indefinite metamaterials have been recently studied [47-52], in order to obtain novel optical properties beyond the conventional dielectric waveguides, especially slow light propagation [49,50], surface modes guidance [47,48], as well as subwavelength mode compression [51,52]. Also Waveguides loaded with metamaterials are of interest because the metamaterials can change the dispersion relation of the waveguide significantly. Slow backward waves, for example, can be produced in Left Handed Metamaterials [LHM]-loaded waveguide without corrugations.

1.6.5 Subwavelength guiding inside wire metamaterials

Generally, Photonic Crystals (PCs) are composed of periodic dielectric or metallo-dielectric nanostructures that have alternating low and high dielectric constant materials (refractive index) in one, two, and

three dimensions, which affect the propagation of electromagnetic waves inside the structure [53]. Due to this periodicity, PCs exhibit a unique optical property, namely, a photonic band gap (PBG) where electromagnetic mode propagation is absolutely zero due to reflection. PBG is the range of frequencies that neither absorbs light nor allows light propagation. By introducing a defect (point or line or both) in these structures, the periodicity and thus the completeness of the band gap are broken and the propagation of light can be localized in the PBG region [9]. Such an outcome allows realization of a wide variety of active and passive devices for signal processing such as, add-drop filters [54] power splitters [55], multiplexers[56], triplexers [57], switches [58], and waveguides [59].

However, because of their wavelength-scale period, PCs result in large devices. This seriously restrains the range of applications, specifically in the low-frequency regimes where the wavelength is large. Metamaterials, on the contrary, possess spatial scales typically much smaller than the wavelength [60]

Metamaterials are usually studied under the approach of the effective medium theory as explained in the previous section and experimentally measured from the far field [61]. They are mainly considered for their macroscopic properties owing to the subwavelength nature of their unit cells.

Recently, Lemoult et al. [62] have merged the wave guiding possibilities offered by PCs and the deep subwavelength nature of metamaterials by focusing on the propagation of waves in metamaterials made of resonant unit cells that are arranged on a deep subwavelength scale to go beyond the effective medium approximation. By manipulating the unit cell of the

wire they were able to experimentally investigate the main components that can be used to control waves at the deep subwavelength scale: a cavity, a linear waveguide, bending as well as the beam splitter

1.7 Fabrication methods of Metamaterials

The reality of metamaterials and their huge potential for novel applications have been demonstrated in a number of experiments that span from radio waves all the way to visible light [12]. The fabrication techniques for metamaterials in these experiments are depend largely on the wavelength of operation. For radio- and microwaves, individual resonators are millimeters or even centimeters in size[63], and can readily be made using printed circuit board technology. However, creating 3D materials requires a large number of such boards to be assembled. Printed circuit boards can still be used for planar terahertz metamaterials, where resonators are tens to hundreds of micrometers, but volumetric assemblies become more difficult to achieve in this regime. In the infrared and visible range, however, higher precision fabrication tools are required.[12]

Undertaking such relies on quite complicated techniques such as Electron-Beam Lithography, Focused Ion Beam milling, Nanoimprint Lithography, Interference Optical Lithography, direct laser writing [11]. While a recenty deployed technique, namely wire drawing, shows a reliable outcome [64].

1.7.1- Electron-Beam Lithography method

EBL were used due to the fact that the required feature sizes for optical metamaterials fabrication are smaller than the resolution of state-of-the-art photolithography, 2D metamaterial layers are normally fabricated using electron-beam lithography [65]. In EBL, a beam of electrons is used to generate patterns on a surface. Beam widths can be on the order of nanometers, which gives rise to the high nanoscale resolution of the technique. EBL is a serial process wherein the electron beam must be scanned across the surface to be patterned. The EBL technique is quite versatile at the point of initial design and preliminary studies of optical properties of metamaterials since it offers sub-wavelength resolution and almost complete pattern flexibility. Moving to shorter wavelengths group at Purdue University reported negative refractive index results in the visible range (n_{eff}=−0.9 and −1.1 at about 770 nm and 810 nm, respectively) [66].

1.7.2- Focused-Ion Beam (FIB) milling Method

FIB was another serial fabrication technique that can be used to make optical metamaterials. Instead of an electron beam, a FIB system uses a focused beam of gallium ions to modify or pattern a design. While the electron beam in EBL only modifies the exposable resist, the accelerated ions in FIB have energies of tens of keV and are “strong” enough to sputter atoms – both metal and dielectric – from the surface of the specimen. FIB is primarily used as a micro-machining tool for purposes such as circuit modification and read-write head trimming. The focused spot size of the

ion beam is around 10 nm, which make FIB an alternative technique for the fabrication of photonic metamaterials [11].

1.7.3- Nanoimprint Lithography (NIL) method

NIL used for volume production of nanostructures with low processing cost, the recently developed process of nanoimprint lithography offers a promising possibility[67]. In NIL a hard mold that contains nanoscale surface-relief features is pressed into a polymeric material cast on a substrate at a controlled temperature and pressure, thereby creating a thickness contrast in the polymeric material. A thin residual layer of polymeric material is intentionally left underneath the mold protrusions, and acts as a soft cushioning layer that prevents direct impact of the hard mold on the substrate and effectively protects the delicate nanoscale features on the mold surface. For most applications, this residual layer needs to be removed by an anisotropic O_2 plasma-etching process to complete the pattern definition.[68]

1.7.4- Direct Laser Writing (DLW) method

In normal DLW, femtosecond laser pulses are tightly focused into the volume of a photoresist. Two-photon absorption ensures that only a tiny volume of the photoresist is sufficiently exposed by the light. Computer-controlled scanning of the focus and resist using piezoelectric actuators allows almost arbitrary polymer structures to be fabricated with lateral resolutions of up to 100 nm, which can readily access resolutions down to 10 nm. However, recent work using stimulated emission depletion DLW

has approached lateral resolutions of 50 nm, with potential for future improvements. [69]

The polymer structures produced through DLW lithography can be filled with gold using electroplating[70]. Electroplating setups can be extremely simple and inexpensive, often requiring only a bias voltage between a transparent electrode on the substrate and a macroscopic counter electrode within a beaker. The metamaterial sample footprint and height is therefore limited only by the DLW lithography process itself.

1.7.5- Laser-Induced Forward Transfer (LIFT) method

As a kind of LDW is a versatile fabrication technique. The principle of LIFT technique is as follows: The laser beam passes through the supporting transparent substrate and focuses on the thin film (donor), and then the illuminated materials can be ablated forward and deposited on the opposite substrate (receiver). Generally speaking, the separation between the receiver and donor in the LIFT technique can be varied from a few micrometers (noncontact-mode LIFT) to zero (contact-mode LIFT), that can lead to different fabricated structures on the donor [71]

1.7.6- Fiber drawing method

Most optical fibers are mainly made of a single material, silica glass or polymer that drawn from the original preform (a cylindrical shape of the raw materials that provides the source material from which the fiber will be drawn in a single, continuous strand). The preform is then fed into a furnace at a rate that allows the temperature of preform to be raised

sufficiently above its glass transition temperature (Tg) of the raw materials to allow its viscosity to fall to a level where it can be readily deformed. As the heated material is pulled down, a characteristic neckdown region forms where a rapid change in diameter occurs [72]. Figure (1.5) shows the fiber drawing tower.

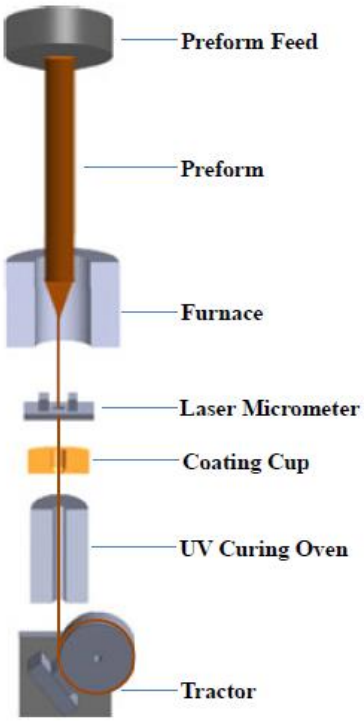

Figure (1.5) Schematic of the thermal fiber drawing process in a drawing tower [73]

Other work, however, generalized optical fiber manufacturing to include microstructured fibers that combine multiple distinct materials. This includes metals, semiconductors, and insulators, which expand fiber-device functionalities while retaining the simplicity of the thermal-drawing fabrication approach [74-79]. This new type of microstructured fibers made of glass and polymer is typically characterized by an embedded geometry of concentric cylindrical shells, acting as an

omnidirectional reflector. For example, a periodic cylindrical-shell multilayer structure has been incorporated into a fiber to guide light in a hollow core with significantly reduced loss for laser surgery [80].

Recently, group on the IPOS, University of Sydney, were using fiber drawing as a novel way of inexpensively producing large amounts of metamaterials [6] potentially kilometers in length. using stuck and draw technique illustrated in figure (1.6). With this technique, a macroscopic dielectric preform containing metals or semiconductors is heated and stretched to fiber, preserving the transverse structure, and reducing the scale while increasing the length. Clearly, this technique is well-suited for the mass production of longitudinally-invariant geometries[81,82].

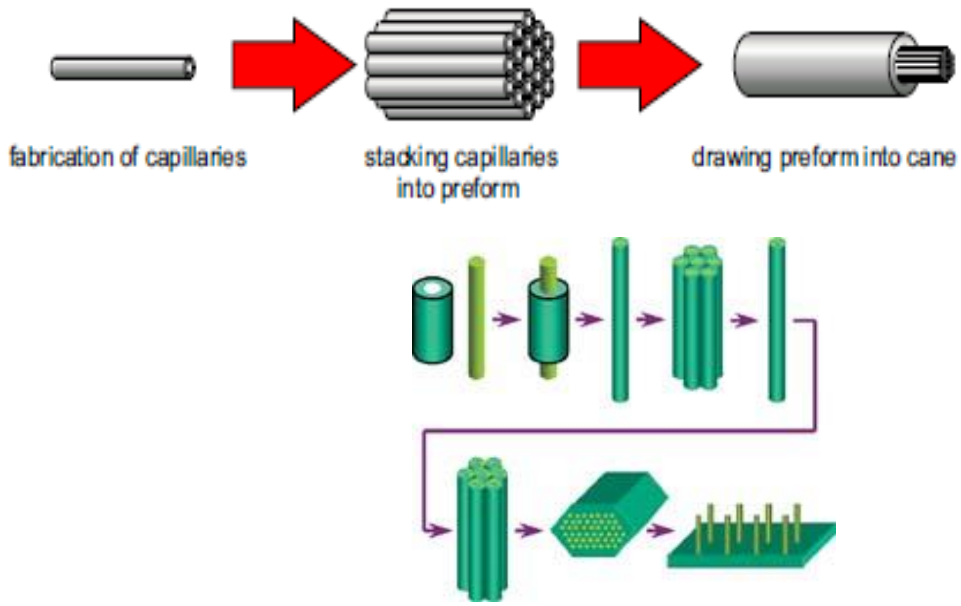

Figure (1.6) Stack and draw method for PCF, Multimaterial production [73]

Drawing has been used to produce fibers containing metallic micro- and nano-structured wires with diameters as small as 50 nm [83], and metamaterial high-pass filtering [76,84] where the effective electric permittivity ε of the fiber can be tailored from THz to visible frequencies [85]. Fibers with retrieved negative effective permeability μ in the THz have also been produced, via a two-step procedure in which metal is sputtered onto a dielectric fiber of appropriate external shape [82,86]. It is worth noting that using this one technique, metamaterials over many frequency ranges can be realized.[82]. Most recently, tapered wire arrays were used to demonstrate a THz hyperlens, which allowed focusing and a resolution an order of magnitude beyond the diffraction limit [87]. The above examples required structures on the 1-10 μm scale, however, the application of this technique to metamaterials for higher frequencies into the mid- and near-IR and optical, which require smaller structures, remains to be investigated.

1.8 Limitations with wire drawing

Fiber drawing method widely used in production of micro wires of conducting or semiconducting materials used in many application such as micro sensors [74] or longitudinal capacitors[88].

For the producing of nanowires limitations of precision take place. Also drawing instabilities and rupture are a serious limitation in polymer fiber and film processing. Onset of these defects depends on the processing conditions, on heat transfer, and on the rheology of the polymer [89]. Plateau-Rayleigh instability was addressed as the most instability affect the production of the relatively long nanowires with fixed diameters

especially when there's a different in viscosities of the multimaterilas consistent a drawing temperature. This phenomenon is under investigation in the present work.

1.8.1 Plateau-Rayleigh instability

Fiber drawing of cylindrical shells and other microstructured geometries clearly opens up rich new areas for fluid instabilities and other phenomena, and it is necessary to understand these phenomena in order to determine what structures are attainable in drawn fibers [90].

Stretching viscous fluids into long thin threads is important in a broad range of applications. Examples include the use of polymeric materials and glass to produce textiles and fibre optics [91]. The production process often requires high temperatures to facilitate stretching with moderate forces. The viscosity of the materials that are typically used can vary dramatically with temperature. Therefore, the resulting thermal gradients can be significant, leading to large gradients in the viscosity of the thread [92].

The convex surfaces of a cylindrical element, such as a fiber, indicate that positive curvatures will exist on any coating films that develop, leading to a positive Laplace excess pressure acting on the film−air surface [93]. The Laplace pressure will generally try to spread a liquid over a surface. In the case of a fiber where the film radius at the solid−liquid interface is different from that at the liquid−vapor interface, this pressure will act to force the liquid out of the film and in doing so will introduce an instability. Here, the liquid surface tension will act to minimize the free surface area, thereby creating the instability [94]. This

instability will cause the liquid film to undulate and break up into an array of droplets. This was first observed by Plateau [95] who demonstrated that all axisymmetric wavelengths greater than the liquid cylinder (film) circumference will be unstable. Of all possible wavelengths, the fastest mode will predominate [96]. This is the commonly known phenomenon of Plateau−Rayleigh instability,

The problem of instabilities was addressed by Tomotika [97], under specific conditions, which are:

1- No general flows in either of the fluids.

2- No slipping at the interface between the column and the surrounding fluid.

3- The difference in normal stress on the inside and outside of the fluid column is purely due to interfacial surface tension.

4- The tangential stress parallel to the surface of the fluid column is continuous at the surface of the column.

With his analysis considering a tapering fluid column within a second fluid, with an exponential decrease in the inner fluid's radius a.The motion of the fluid along the elongation direction to smaller diameters was described in the time domain. The instability was decomposed into a Fourier series, and a component with a particular initial wavelength λ_0, and amplitude $\bar{\varepsilon_0}$ was considered. The growth of that instability component to an amplitude $\bar{\varepsilon}$ was described by

$$\ln\left[\frac{\bar{\varepsilon}/a}{\bar{\varepsilon}_0/a_0}\right] = \frac{\sigma x_0^{1/3}}{3\mu a_0 C}\int_x^{x_0} x^{-\frac{4}{3}}(1-x^2)\Phi(x,\mu'/\mu)dx \qquad (1.19)$$

Where σ the interfacial tension of the fluids, μ the outer fluid's viscosity, and C a constant describing the evolution of the fluid column such that the radius decreased as $a = a_0 e^{-\frac{1}{2}Ct}$. Consequently, the wavelength of the instability component increased as $\lambda = \lambda_0 e^{Ct}$, and the variable $x = \frac{2\pi}{\lambda}a = x_0 e^{-\frac{3}{2}Ct}$ represents a normalized wavenumber and $\Phi(x,\mu'/\mu)$ are given by [97], depending on x and the ratio of the viscosity of the inner fluid column (here: metal) μ' and that of the surrounding fluid μ:

$$\Phi(x,\mu'/\mu) = \frac{N(x)}{D(x)},$$

$$N(x) = I_1(x)\Delta_1 - \{xI_0(x) - I_1(x)\}\Delta_2,$$

$$D(x) = (\mu'/\mu)\{xI_0(x) - I_1(x)\}\Delta_1 - (\mu'/\mu)\{(x^2+1)I_1(x) - xI_0(x)\}\Delta_2 - \{xK_0(x) + K_1(x)\}\Delta_3 - \{(x^2+1)K_1(x) + xK_0(x)\}\Delta_4,$$

$$\Delta_1 = \begin{vmatrix} xI_0(x) - I_1(x) & K_1(x) & -xK_0(x) - K_1(x) \\ I_0(x) + xI_1(x) & -K_0(x) & -K_0(x) + xK_1(x) \\ (\mu'/\mu)xI_0(x) & K_1(x) & -xK_0(x) \end{vmatrix}$$

$$\Delta_2 = \begin{vmatrix} I_1(x) & K_1(x) & -xK_0(x) - K_1(x) \\ I_0(x) & -K_0(x) & -K_0(x) + xK_1(x) \\ (\mu'/\mu)I_1(x) & K_1(x) & -xK_0(x) \end{vmatrix}$$

$$\Delta_3 = \begin{vmatrix} I_1(x) & xI_0(x) - I_1(x) & -xK_0(x) - K_1(x) \\ I_0(x) & I_0(x) + xI_1(x) & -K_0(x) + xK_1(x) \\ (\mu'/\mu)I_1(x) & (\mu'/\mu)xI_0(x) & -xK_0(x) \end{vmatrix}$$

$$\Delta_4 = \begin{vmatrix} I_1(x) & xI_0(x) - I_1(x) & K_1(x) \\ I_0(x) & I_0(x) + xI_1(x) & -K_0(x) \\ (\mu'/\mu)I_1(x) & (\mu'/\mu)xI_0(x) & K_1(x) \end{vmatrix}$$

$I_n(x)$ and $K_n(x)$ are the modified Bessel functions of the *n*th order. Figure (1.7) presents the geometry of the multimaterial fiber.

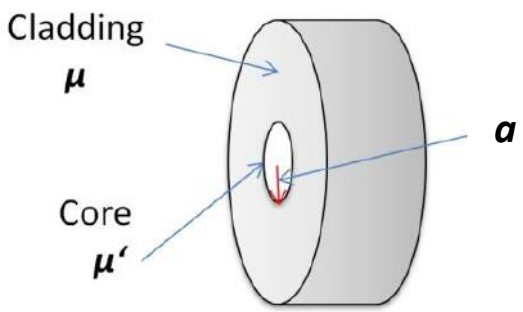

Figure (1.7) Geometry of a fiber with viscosity ratio μ′/μ and column radius, *a*

Return to (1.19)

$$\left[\frac{\bar{\varepsilon}/a}{\bar{\varepsilon}_0/a_0}\right] = e^{\frac{1}{2}\int_0^{t'} \frac{\sigma}{\mu a}(1-x^2)\Phi(x,\mu'/\mu)dt} \tag{1.20}$$

$$\left[\frac{\bar{\varepsilon}/a}{\bar{\varepsilon}_0/a_0}\right] = e^{\frac{\sigma}{2\mu a}(1-x^2)\Phi(x,\mu'/\mu)t} \tag{1.21}$$

by taken *n* as

$$n = \frac{\sigma}{2\mu a}(1-x^2)\Phi(x,\mu'/\mu). \quad [\mathrm{s}^{-1}] \tag{1.22}$$

$$\frac{\bar{\varepsilon}}{a} = \frac{\bar{\varepsilon}_o}{a_o} e^{nt} \tag{1.23}$$

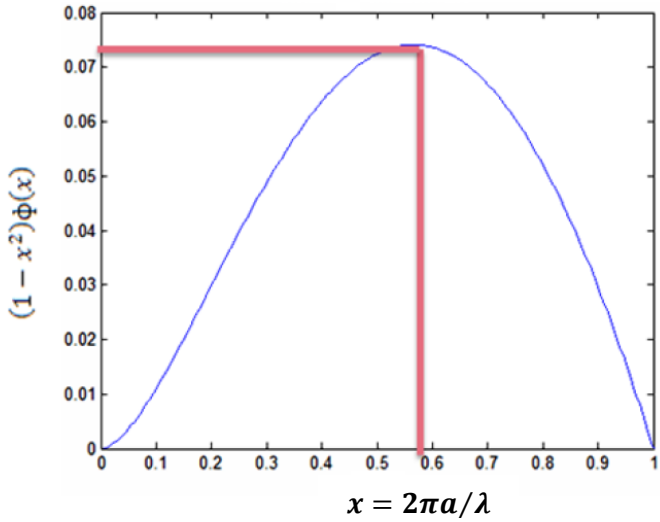

Figure (1.8) Curve of $(1-x^2)\Phi(x)$ when $\mu'/\mu = 0.91$. This viscosity ratio corresponds to a cylindrical thread of black lubricating oil surrounded by golden syrup. The red lines indicate the maximum [97].

A graphical representation of eq. (1.28) was shown in figure (1.8) for $\mu'/\mu = 0.91$. This viscosity ratio corresponds to a cylindrical thread of black lubricating oil surrounded by golden syrup. The red lines indicate the maximum . In this case only the term $(1-x^2)\Phi(x,\mu'/\mu)$ is shown as the term $\frac{\sigma}{2\mu a}$ is constant for a given temperature. The horizontal axis of figure (1.8) is $\frac{2\pi a}{\lambda}$ where a is the radius of the filament and λ is the wavelength of the perturbation. Values greater than unity indicate wavelengths smaller than the circumference of the filament, breakup at these dimensions would create spheres smaller than the radius of the cylinder increasing the final surface area of the shape. The gain rate for these wavelengths is below zero and hence these perturbations would decay. From the figure (1.8) it is obvious that the wavelength with the maximum gain occurs at an x or $\frac{2\pi a}{\lambda}$ value of around 0.56 and hence a wavelength of around $11a$ [97].

In 2011 S. Shabahang et al. group from MIT [98] were observed of the Plateau-Rayleigh capillary instability during the tapering of a multi-material optical fiber. The fiber core is a glass, and the cladding is an amorphous polymer. The instability is manifested in the breakup of the core into a periodic string of size-tunable micro-scale droplets embedded along the fiber axis as shown in figure (1.9). The particle diameters may be tuned in the 1–20 μm range through control of the tapering speed and temperature.

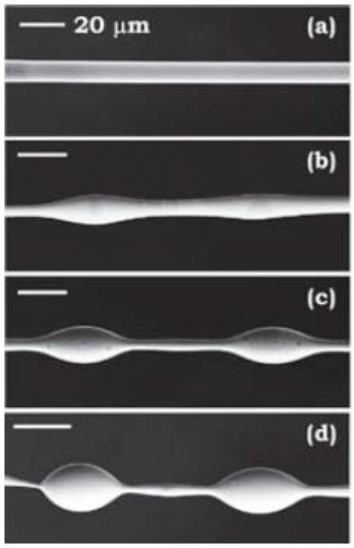

Figure (1.9) SEM micrographs of the fiber core at different stages of the PR instability during static heating at 287º C. Scale bars are all 20 μm. [98]

In their previous work [7], IPOS group mentioned that wires on the 1 μm scale appeared to be the limit for the indium /polymer platform. Large fluctuations in the wires' diameter were observed as the diameters approached 1 μm as shown in figure (1.10), and attempts at smaller wires lead to the wires breaking up into droplets. That fluctuations and break-up may arise from the above mentioned Plateau-Rayleigh instability.

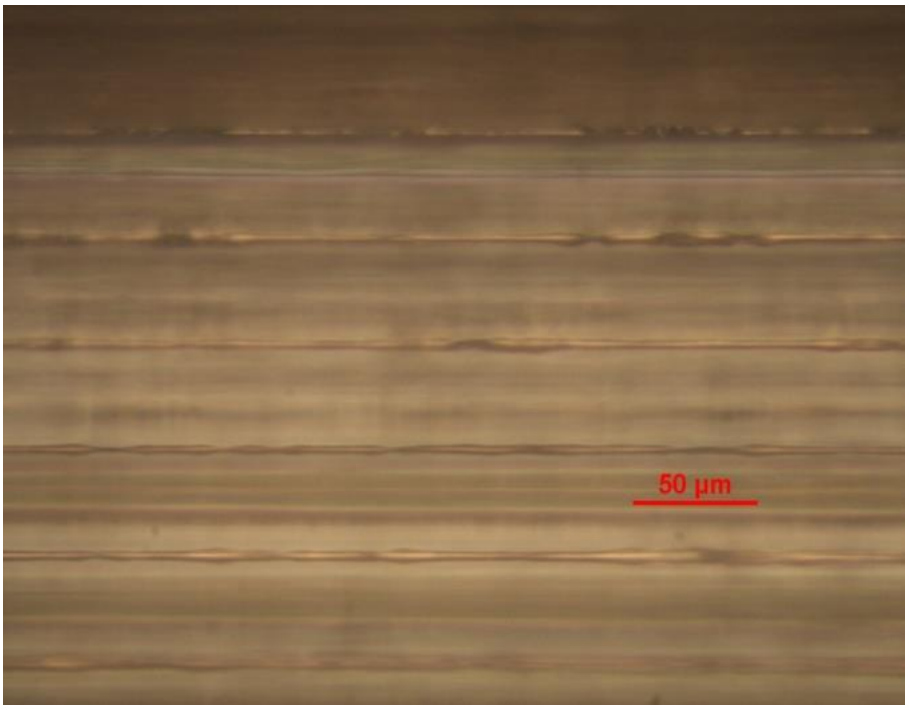

Figure (1.10) Example of fluctuations in the diameter of indium wires drawn inside a PMMA fibre.

1.9 Literature Survey

Multimaterial fibers is defined to be a high-aspect-ratio structures that comprise multiple distinct materials, typically produced by thermal drawing from a macroscopic scaled-up model (preform). With the evolution of multimaterial fibers come new ways of thinking about the fiber drawing process itself. Through dimensional reduction, nanostructures such as nanowires with few-nanometer diameters and unprecedented lengths have been produced. Drawing multimaterials with different viscosities arising specific kind of instability which alter the diameter of produced core

Bayindir et al. 2004 [75] Designed and fabricated of fibres made of conducting, semiconducting and insulating materials in a variety of

geometries using fiber drawing technique. They demonstrated that this approach can be used to construct a tunable fibre photodetector comprising an amorphous semiconductor core contacted by metallic microwires, and surrounded by a cylindrical-shell resonant optical cavity. Such a fibre is sensitive to illumination along its entire length (tens of meters).

Wylie et al. 2007 [92] Considered the stretching of a thin viscous thread, whose viscosity depends on temperature. They showed that thermal effects lead to the surprising result that steady states exist for which the force required to stretch the thread could decreased when the pulling speed was increased. Also, they studied the stability of steady-state solutions and found that a complicated sequence of bifurcations could arise.

Zhang et al. 2008 [81] Produced vertically aligned metallic micro/nanowires by uniquely combining a novel fiber drawing technique and advanced materials using stack and draw method. This method could control the diameter, length and inter-wire spacing over a large range, and provide ordered materials at low-cost for a range of applications

Mazhorova et al. 2010 [76] Studied the challenges in the fabrication of metamaterials with sub-micrometer metallic wires by repeated stack-and-draw process. By comparing samples made using 2, 3 and 4 consecutive drawings for aligned metallic (tin alloy) microwires or chalcogenide As_2Se_3 microwires. They found that when using metallic alloys phase

separation effects took place and nano-grids formation on small metallic wires observed.

Badinter et al. 2010 [83] Reported on a technological route allowing one to integrate huge amounts of electrically isolated metal or semimetal (Pb/Sn alloys and Bi) nanowires in glass fibers with the diameter of up to a few hundreds of micrometers and the length reaching 1 m, the nanowires exhibiting a two-dimensional hexagonal distribution in the cross-sectional plane.

Tuniz et al. 2010 [84] Introduced drawing as a means of fabricating metamaterials, thus demonstrating a terahertz metamaterial. They co-draw PMMA and indium, producing several meters of metamaterial with wire diameters down to ~ 10 μm, and lattice constants of ~ 100 μm.

Danto et al. 2011 [99] Demonstrated the first rewritable memory in thermally drawn fibers by drawing a high tellurium-content chalcogenide glass, contacted by metallic electrodes internal to the fiber structure. An externally applied voltage can be utilized to switch between a high resistance (OFF) and a low resistance (ON) state; this in turn allows the fibers to function as a memory device reminiscent of the ovonic switch.

Deng et al. 2011 [90] Examined fluid instabilities during the complicated thermal drawing fabrication processing. They studied classical Plateau-

Rayleigh instabilities in the form of radial fluctuation. Also they established a viscous materials map from calculations.

Shabahang et al. 2011 [98] Reported the observation of the Plateau-Rayleigh capillary instability during the tapering of a multi-material optical fiber. The fiber core was a glass, and the cladding was an amorphous polymer. The instability was manifested in the breakup of the core into a periodic string of size-tunable micro-scale droplets embedded along the fiber axis. The particle diameters were tuned in the 1–20 mm range through control of the tapering speed and temperature.

Tuniz et al. 2011 [82] Presented a novel method for producing drawn metamaterials containing slotted metallic cylinder resonators, possessing strong magnetic resonances in the terahertz range. Resulting structures were either spooled to produce a 2-dimensional metamaterial monolayer, or stacked to produce three-dimensional multi-layered metamaterials. Also they experimentally investigated the effects of the resonator size and number of metamaterial layers on transmittance.

Lemoult et al. 2012 [62] Demonstrated that they could tailor unit cells locally inside the metamaterials to shape the flow of waves at deep subwavelength scales. They validated their approach in experiments with both electromagnetic and acoustic waves in the meter range demonstrating cavities, waveguides, corners and splitters with centimeter-scale dimensions, an order of magnitude smaller than previous proposals

Tuniz et al. 2013 [87] Demonstrated imaging through straight and tapered wire arrays, produced using fiber drawing technique, operating in the terahertz spectrum, with unprecedented propagation of near field information over hundreds of wavelengths and focusing down to 1/28 of the wavelength with a net increase in power density.

Naman et al. 2013 [7]

Used fibre drawing technique to fabricate indefinite media based on wire array metamaterials. Fibres containing arrays of indium wires embedded in polymer were drawn using an optical fibre draw tower. During drawing, the surface tension of the liquid indium could result in fluctuations to the wire diameter through the Plateau–Rayleigh instability. Through a modification of the draw process they were able to achieve wire diameters as low as 1 micrometer. Such wire array fibres were assembled and characterized as electric metamaterials through the resulting high-pass filtering behavior.

Demay et al. 2014 [89] Reported different forms of the draw resonance instability encountered in fibre spinning, cast-film and film blowing.
They presented time dependent equations for the simplified situation of constant width cast-film.

1.10 Aim of the Work

The aim of this research is to investigate the Plateau-Rayleigh instability effect on the fabrication of metamaterials using fiber drawing method. This can be achieved through the following steps:

1- Developing a description of the Plateau-Rayleigh instability. This will be applied to the draw process used for producing wire metamaterials with negative permittivity. Nonmagnetic indium metal was drawn inside the PMMA polymer.

2- A mathematical model used then to study the possible fluctuation for the small drawing ratio.

3- Study the effect of wavelength of the fluctuations throughout drawing, and compare these predictions with experimental results.

4- Finally, CST simulation was used to design a subwavelength guide inside the metamaterials as an application in the field of electronics and photonics.

Chapter Two: Experimental Work

2.1 Introduction

Fabrication process of electrical metamaterials in Far-IR response needs the metallic wire diameter to be in the range of μm. This needs complicated method. Fiber drawing technology in the producing wire metamaterials gives the capability of mass production in simple way as described previously. In the current method indium metal is used as conductors while PMMA is used as a host dielectric. They were co-drawn to produce electrical metamaterials. When indium wire diameter reaches 1 μm during the drawing process the fluctuation on the diameter appears. This is might be due to classically described Plateau-Rayleigh instability. Drawing tower components and drawing methodology will be presented first. The production of wire metamaterials under different drawing conditions to reach different wire diameter was done using primary and secondary sides of the tower. Neckdown profiles as well as the drawing conditions were used then to simulate the instability in the produced wires as will describe in chapter three. Finally the chapter will illustrate the method of recording the preform temperature profile for different feed speeds and furnace set temperatures.

2.2 The physical properties of the indium and the PMMA

PMMA and indium are having relatively the same glass transition temperature making them suitable for co-drawing. Table (2.1) shows the physical properties of indium, while table (2.2) shows the physical properties of PMMA.

Table (2.1) The physical properties of the indium metal [100]

Physical properties of indium	Value	Unit
Melting point	156.6	^{o}C
Boiling Point	2080	^{o}C
Density	7.31	g/cm^3
Thermal expansion	50 – 90	$10^{-6}/K$
Thermal conductivity	81.8	W/m.K
Electrical resistivity	83.7	nΩ.m
Young's modulus	11	GPa

Table (2.2) The physical properties of the PMMA [72]

Physical properties of PMMA	Value	Unit
Melting Point	160	^{o}C
Young's modulus	1800 - 3100	MPa
Elongation	2 – 10	%
Tensile strength	48 – 76	MPa
Thermal expansion	50 – 90	$10^{-6}/K$
Thermal conductivity	0.167 - 0.25	W/m.K
Refraction index	1.492 - 1.492	
Water absorption	0.3 - 0.4	%

2.3 Fabrication Process

Wire metamaterial was fabricated using stack and draw process. The drawing took place inside the two sided drawing tower from Heathway Company equipped with radiative furnace. The tower was extend over two stages with about 6.2m height, as shown in figure (2.1). Each side of the tower consists of controlled feeding and drawing mechanism, furnace, precision measurement tools for the produced diameter as well as tension meter. Controlled vacuum system is also attached to the tower

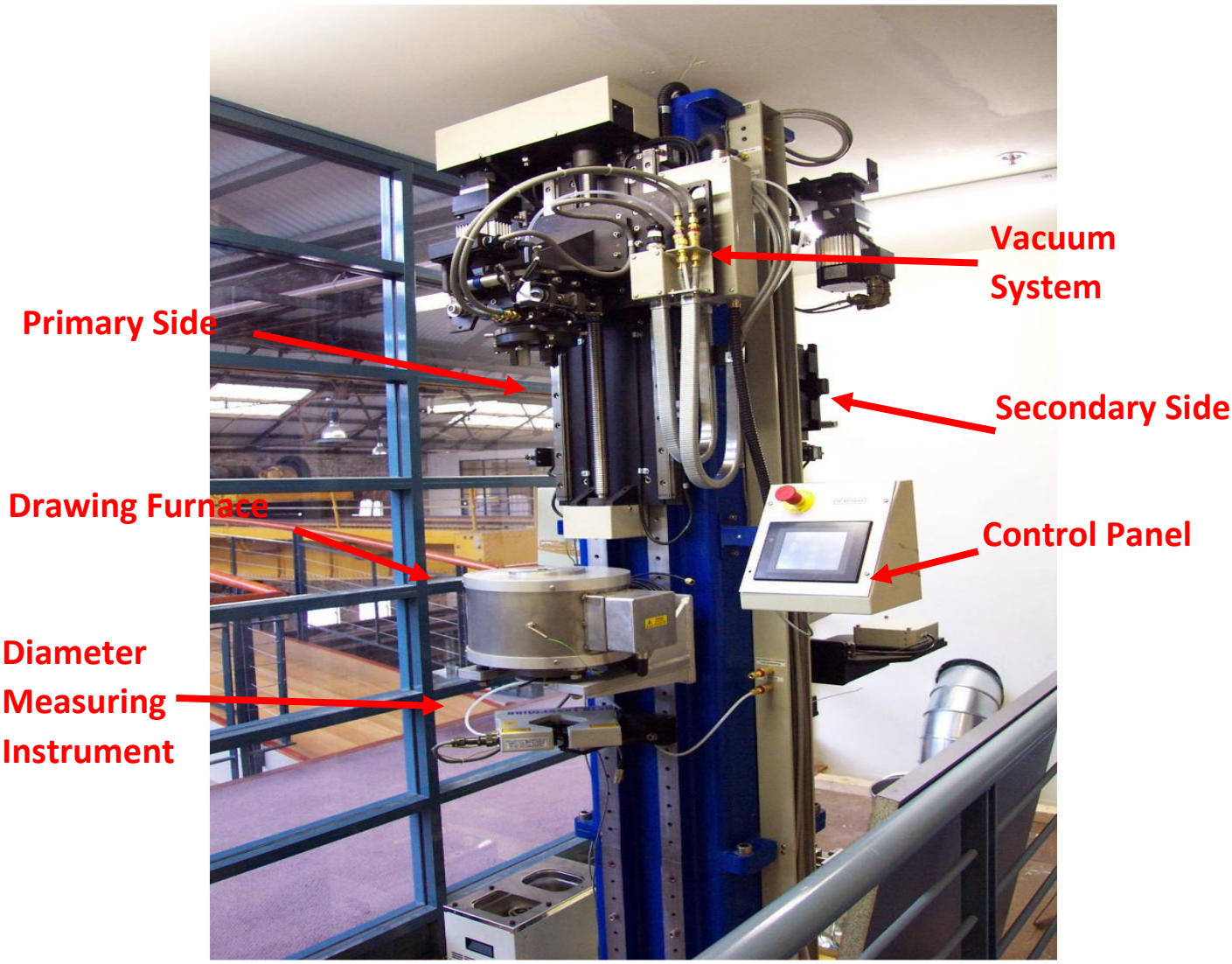

Figure (2.1) Fiber Drawing Tower by Hathway Company.

2.3.1 Primary Side

Primary side of the drawing tower was used mainly for changing the preform diameter or thickness to desire value by stretching or sleeving. Figure (2.2) shows the main parts of the primary side of the tower.

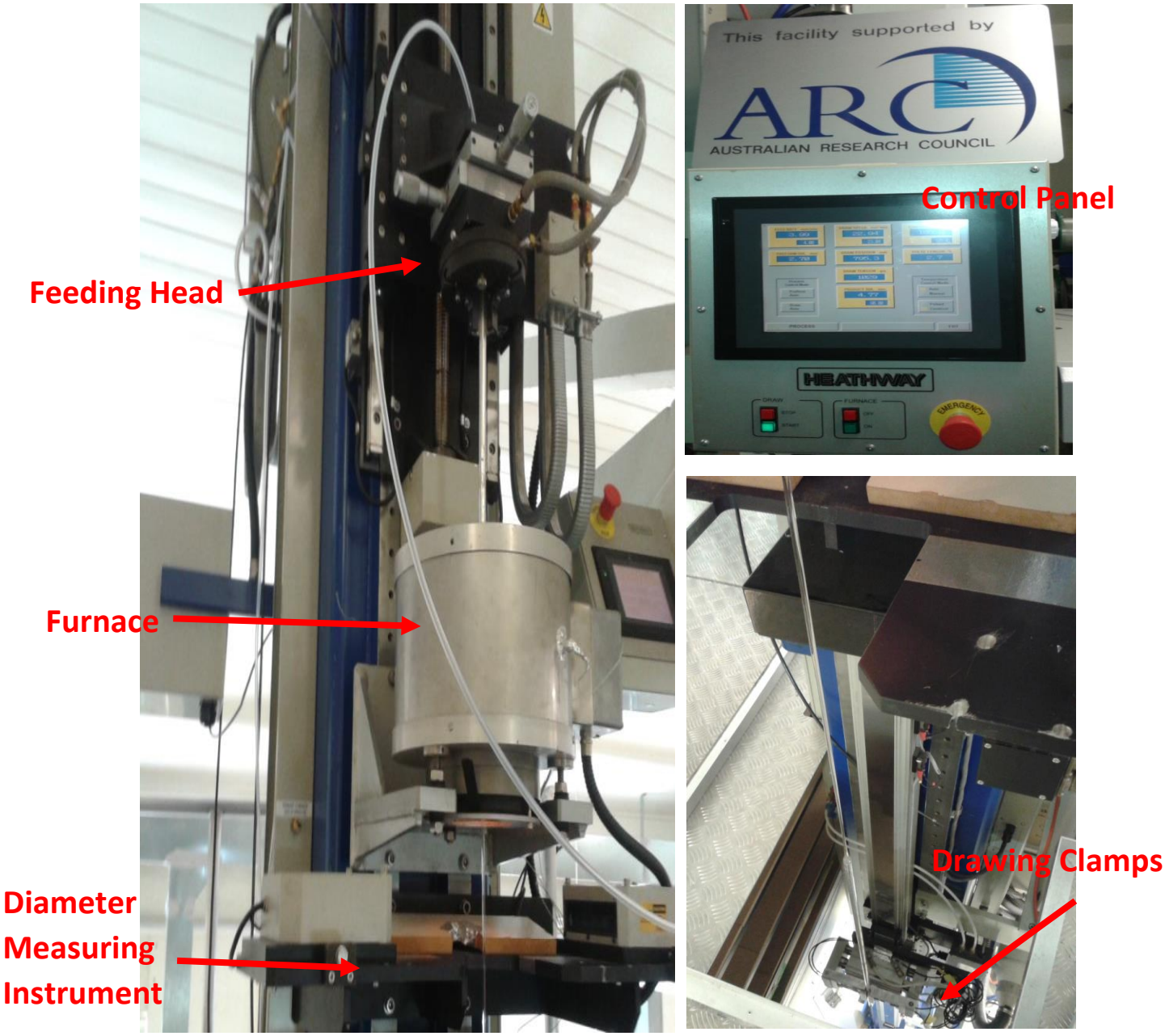

Figure (2.2) Main parts of the primary side of the tower.

a- Stretching

Stretching is used when the decrease in the diameter of the preform is desired. By manipulating feeding and drawing speed one can control the diameter of the produced preform. The relation between the mastering parameters can be easily derived from the conservation of mass during the drawing process [72].

$$Final\ diameter = \sqrt{\frac{Drawing\ speed}{Feeding\ speed}} \times Initial\ diameter \qquad (2.1)$$

Knowing that the ratio of the inner diameter to the outer diameter of the tube will preserved during stretching process

In order to prepare our samples 6mm/12mm PMMA tube was stretched to 2.75mm/5.5mm by setting the feeding speed 7 mm/sec and drawing speed to 30.45mm/sec with temperature furnace set to 200 °C.

b- Sleeving

Sleeving technique is used to increase the wall thickness of the tube (changing the inner diameter to outer diameter ratio). The process is carried out by fitting small tube inside outer jacketing tube. Inner tube must have an outer diameter with 10% smaller than the inner diameter of the outer jacket to prevent jacket warping during sleeving. Vacuum system with reasonable value (100 mbar) is used to get rid of the air between the two walls during the drawing process. Figure (2.3) shows the schematic for the vacuum system used during the sleeving, as well as, photographs for the top and bottom assembly for the tubes in the sleeving.

The 2.75mm/5.5mm tube was sleeved inside 6mm/12mm jacket tube at 220° C to reach 1.2mm/ 5mm PMMA tube.

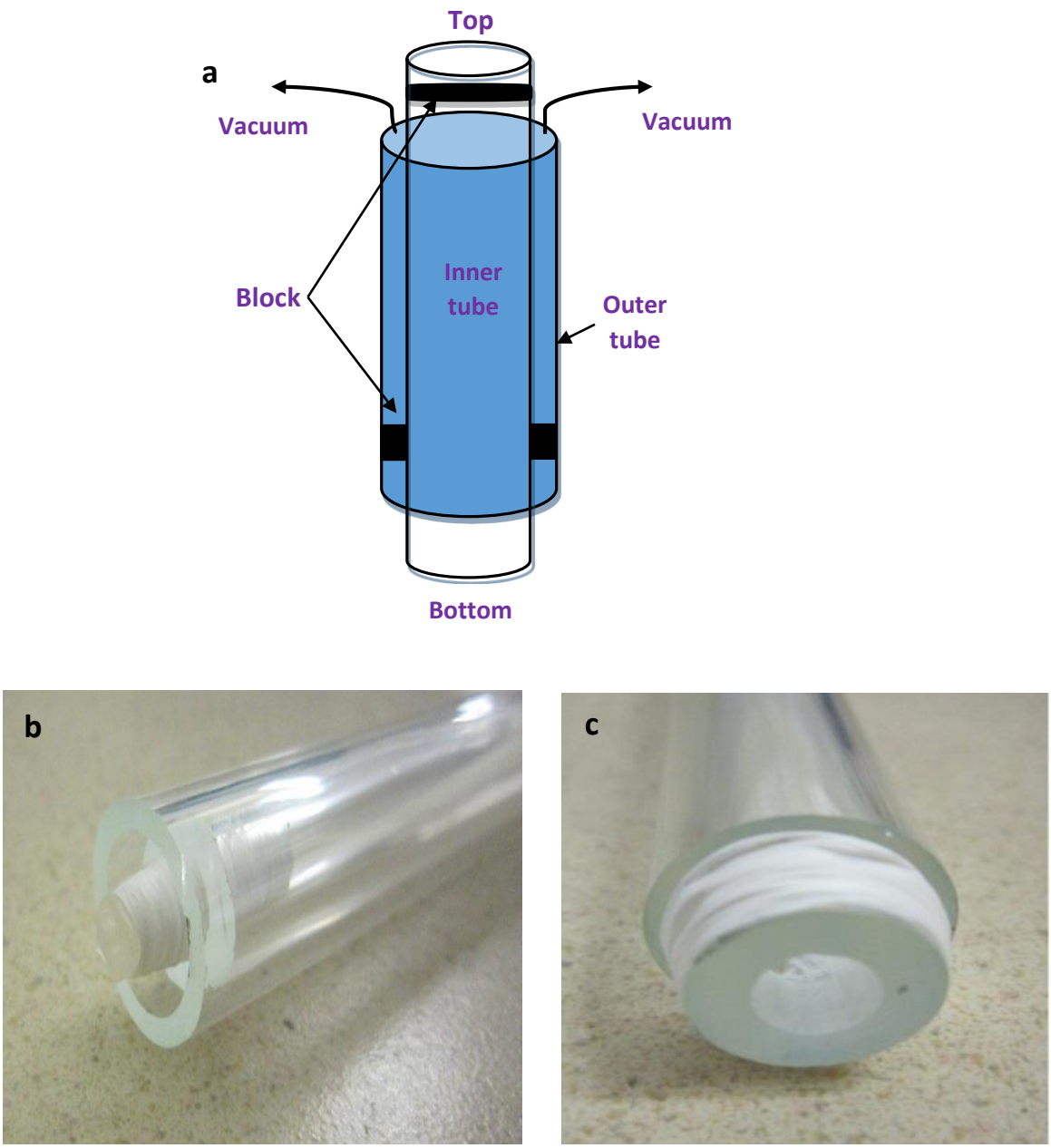

Figure (2.3) a- Schematic for the vacuum system used in sleeving, Cross sectional diagram of sleeving process b- top c- bottom of the sleeved tube.

c- Annealing

Annealing is a heat treatment that alters the physical and sometimes chemical properties of a material to increase its ductility and to make it more workable.

Annealing preforms before drawing or between two drawings is crucial step in the drawing polymer to fiber. Any residual stress or moisture could be removed by annealing to minimize the chance of bubbling as the PMMA highly absorbed H_2O. Annealing temperature scheme is ramping the temperature from the room temperature to a value slightly below glass transition temperature of the material (90° C in PMMA case). Rising temperature took place over 2 days then maintaining at 90° C for two weeks, depending on the preform thickness. Then ramping back to room temperature over two days. Figure (2.4) shows the thremoline laboratory oven used for annealing our preforms.

Figure (2.4) Thremoline laboratory oven

d- Filling with indium

Filling the tube with about 1mm inner diameter with solid indium metal is a hard process. To do so in easy way the indium was melt firstly inside laboratory beaker over a hotplate, as shown in figure(2.5). Molten indium sucked then inside the PMMA tube using the vacuum process (syringe here). PMMA tube attached to the syringe using Teflon tape.

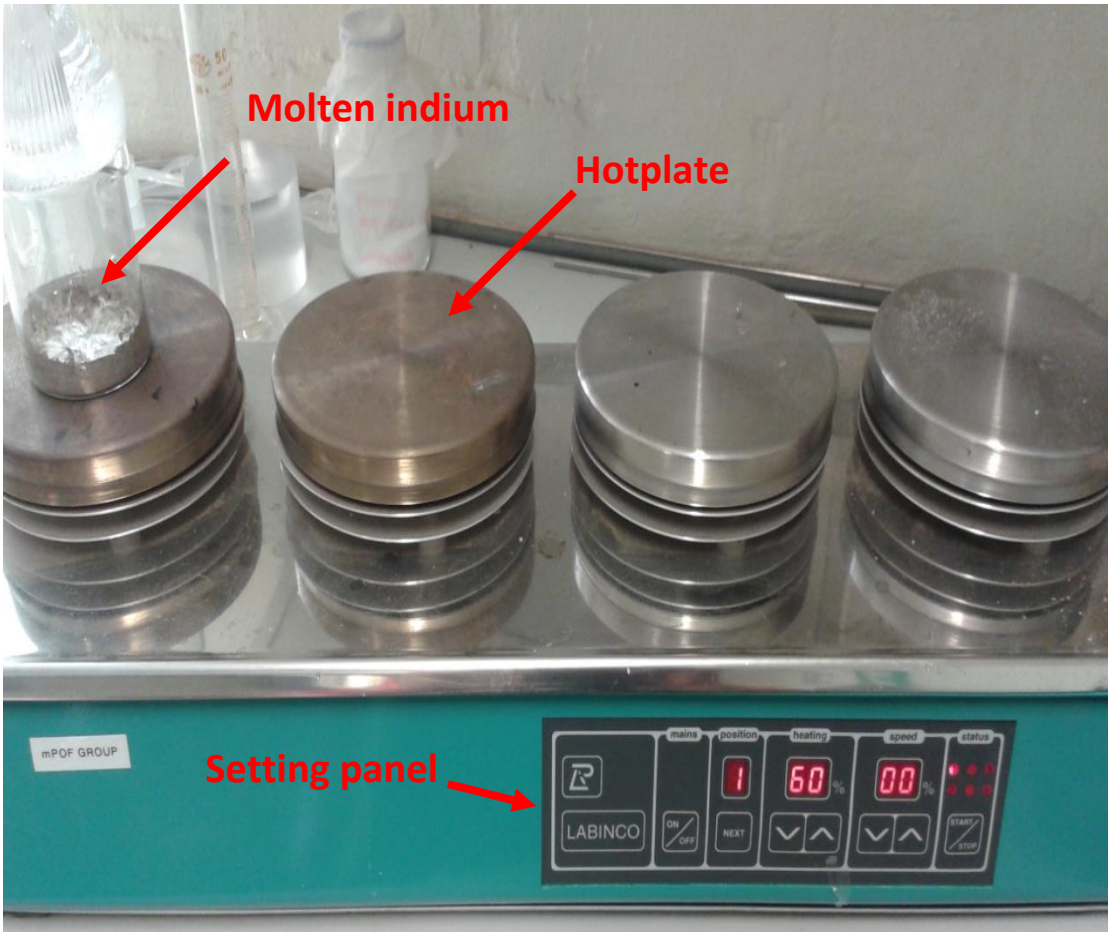

Figure (2.5) Molten indium inside beaker over hotplate

Using this method a tube with 18 cm length filled with indium, as shown in figure (2.6), was prepared without air gaps

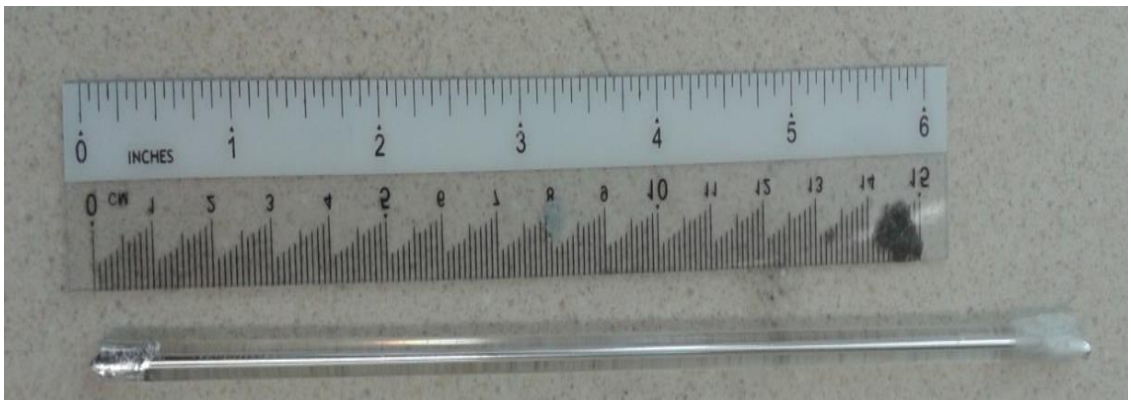

Figure (2.6) PMMA tube filled with indium .

2.3.2 Secondary side

Secondary draw side, figure (2.7), was used for drawing the final preform to the fiber with diameter less than 1mm with conservation of the preform shape. The operation conditions such as, temperature, feed and draw speed are fully controlled by computer. The key parameters that connect all these conditions are the required final diameter and the tension during the drawing. Sometimes increasing the furnace set temperature or decreasing the feed speed are the solution in the case of high tension in drawn fiber. Tense fiber might snap. On the other hand decreasing the temperature or increasing the feed speed will reflect on less fluctuation in the produced indium wires as discussed later in the next chapter.

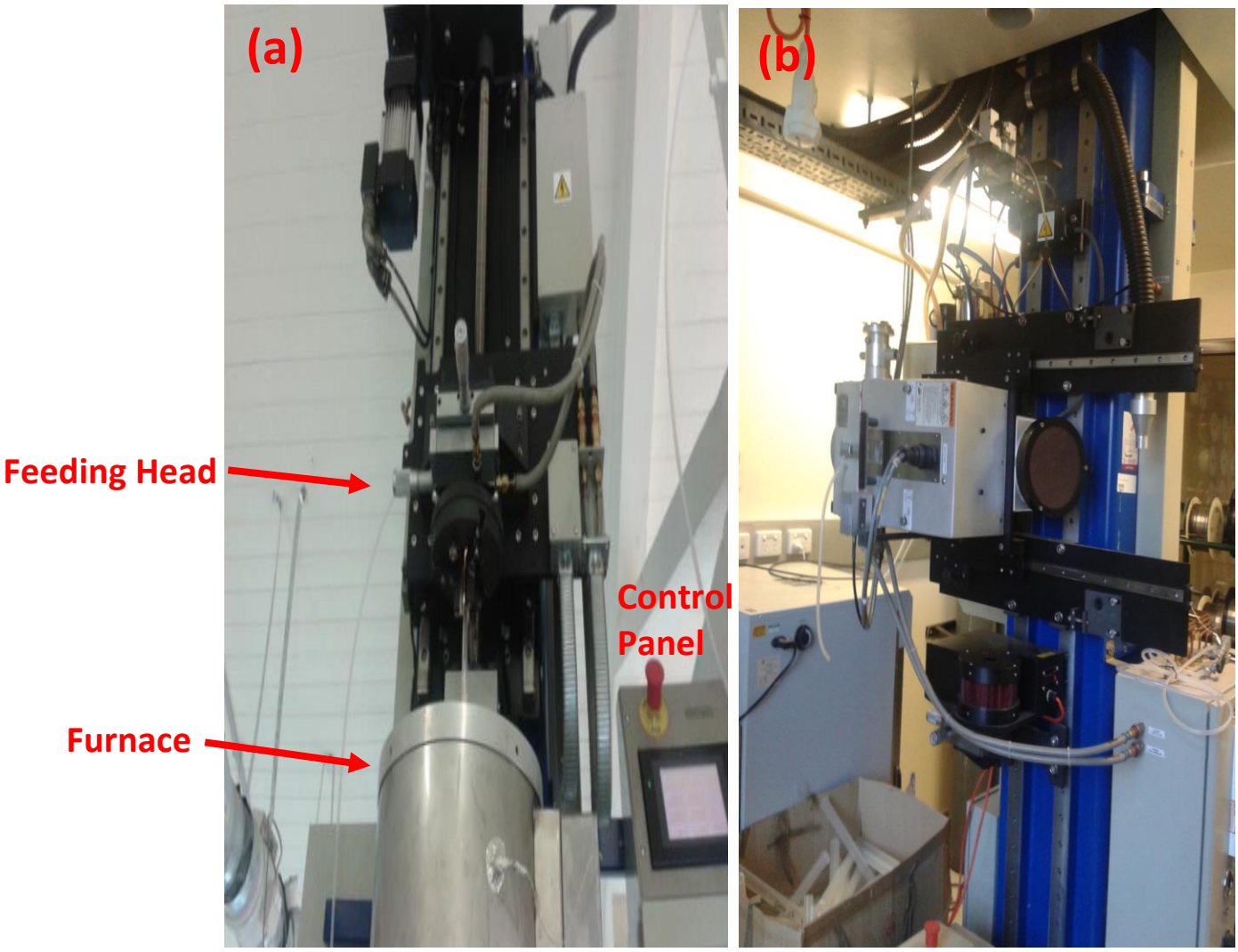

Figure (2.7) Secondary side of the drawing tower a-top floor b-down floor

Secondary side has additional equipment of capstan to control drawing speed and measuring the tension of the produced fiber. Spool wheels for fiber tension equilibrium during spooling. Drum winder was used for spooling the produced fiber on the plastic bobbin within even km length to be ready for testing. Also the secondary draw was equipped with two axes LaserMike diameter monitoring device to check the elliptic of the

produced fiber. Figure (2.8) shows the extra equipment for the secondary side

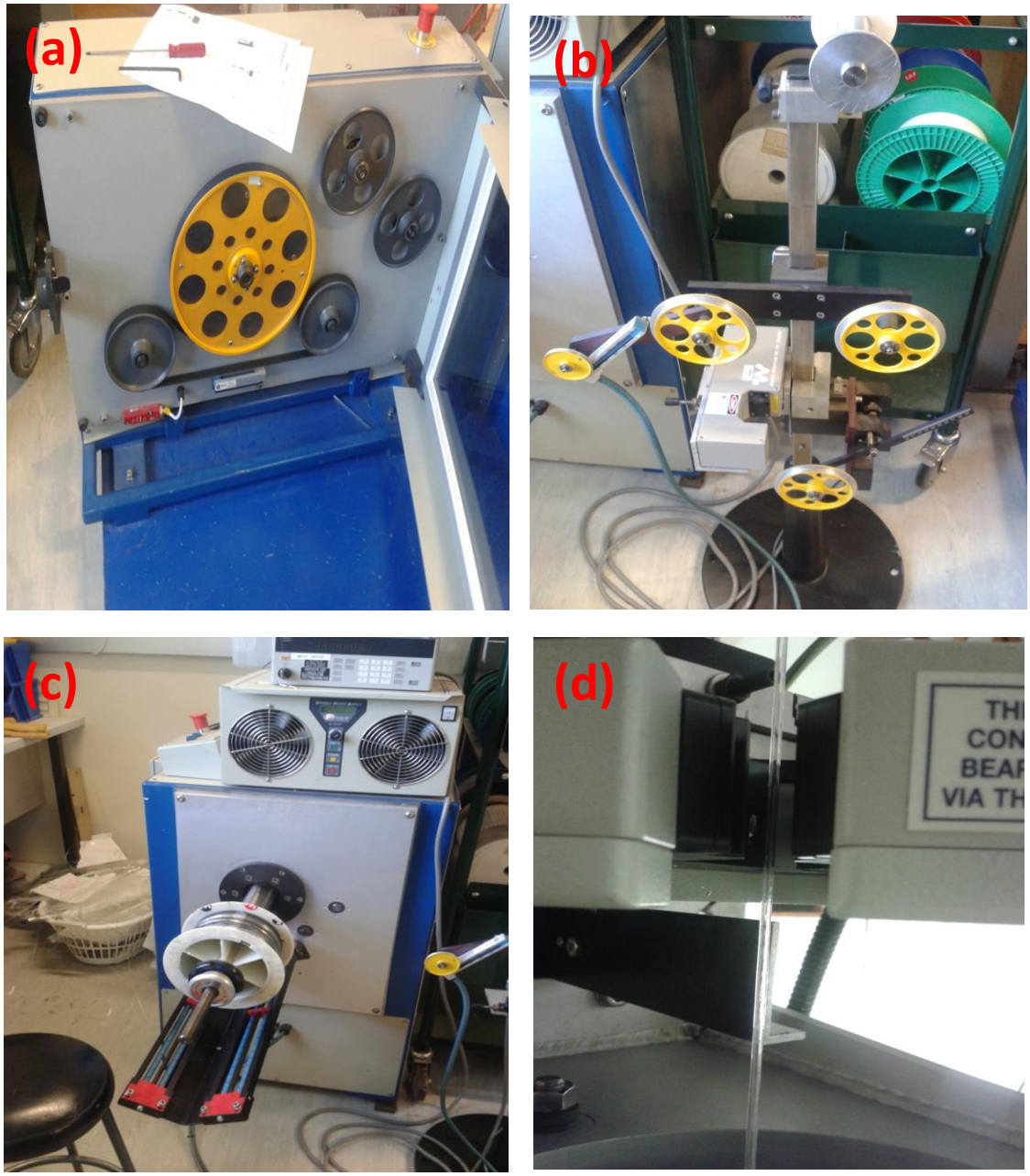

Figure (2.8) a- Capstan, b-Tension equilibrium wheels, c- Drum winder, d-two axes LaserMike diameter monitoring device.

For drawing preform to fiber, the preform was heated inside the radiative furnace up to 230° C. Heating took place first without turning on the

feeding or drawing, waiting then for the preform to start dropping down with the aide of about 200 g tension attached to it. As soon as the drop off filling down then the feed have to start and the drop off have to guide through the capstan and spooling wheels with turning on the drawing speed. Equation (2.1) was used also to calculate the required feeding and drawing speed for desired fiber diameter.

To investigate how the neckdown profile affected by both the set temperature of the furnace and the feeding speed, a set of draws were carried out on 12mm/6mm PMMA tubes at different conditions. Figure (2.9) shows the neckdown profiles. The effect of these conditions on the neckdown profile, as well as, the growth of the instability will be discussed in Chapter Three

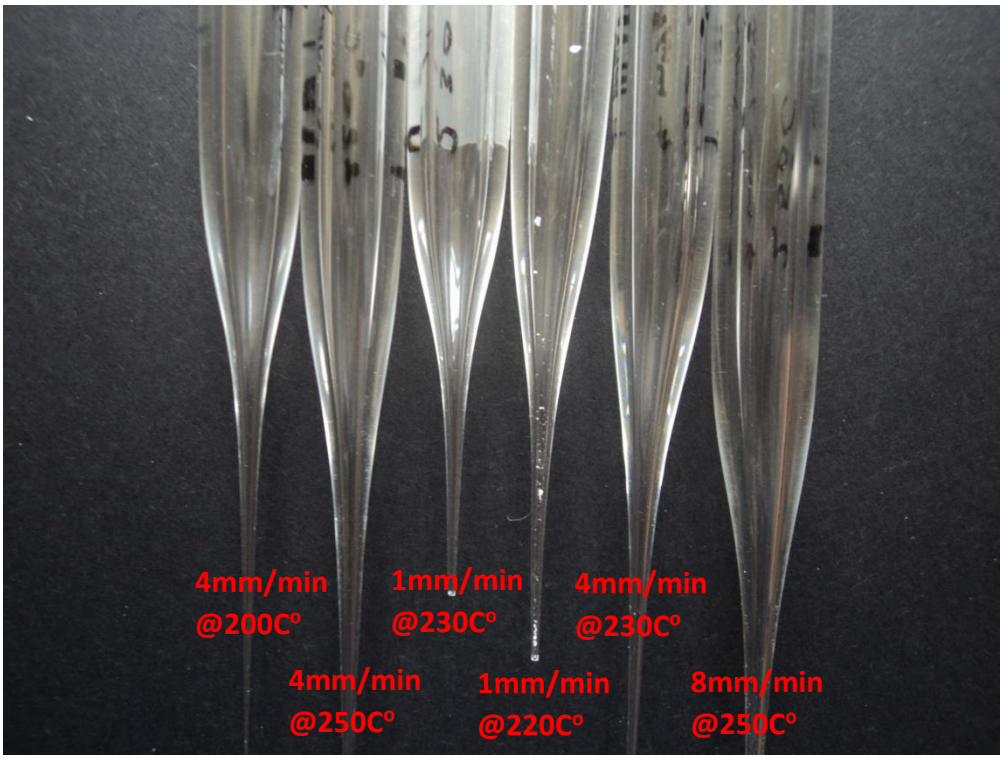

Figure (2.9) Neckdown profiles at different drawing conditions

Our preform, mentioned earlier in (2.2.1), were drawn to the fiber with single indium wire at different conditions as will illustrate in Chapter Three

2.3.3 Stack and Draw

Stack-and-draw technique is the most successful way to make PCFs. Rods and tubes, typically a millimeter in diameter and 30 cm in length, are carefully stacked in a spaghetti-like bundle to give the required pattern of indium wires distribution as shown in figure (2.10). This stack is then heated in a furnace and drawn into a fiber in the same way that conventional fibers are made.

Stack and draw method was used in the producing the indium wires with diameter in μm or sub μm using a series of two or even three draws. Figure (2.11) shows the stacking of many fibers inside external jacket.

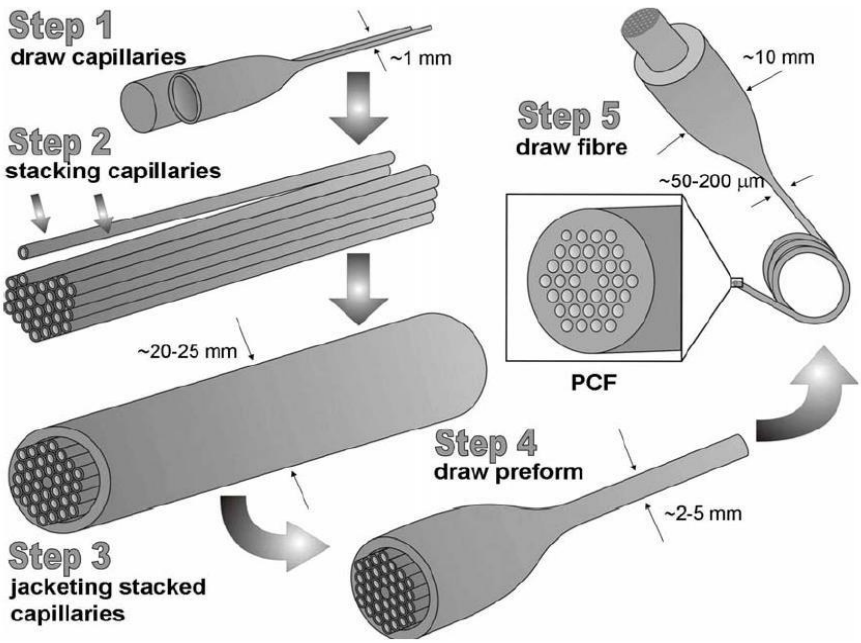

Figure (2.10) Stack and draw technique for PCFs production[72]

Figure (2.11) Stacking many fibers inside external jacket

In order to fix the wire positions at a desire distribution during the drawing for preventing the crossing of the indium wires during the drawing, an idea of preparing preform, shown in figure (2.12), by filling the holes of solid core photonic crystal preform of 8.5 mm outer diameter with 45 PMMA fibers. Fibers has diameter of 240-250 μm containing single 33.1 μm indium wire. Preform drawn then to 550 μm fiber at furnace set temperature of 180 °C with drawing speed =2mm/min. Vacuum of 130 mbar was applied to suck the air between the PCF air holes and the filling fibers.

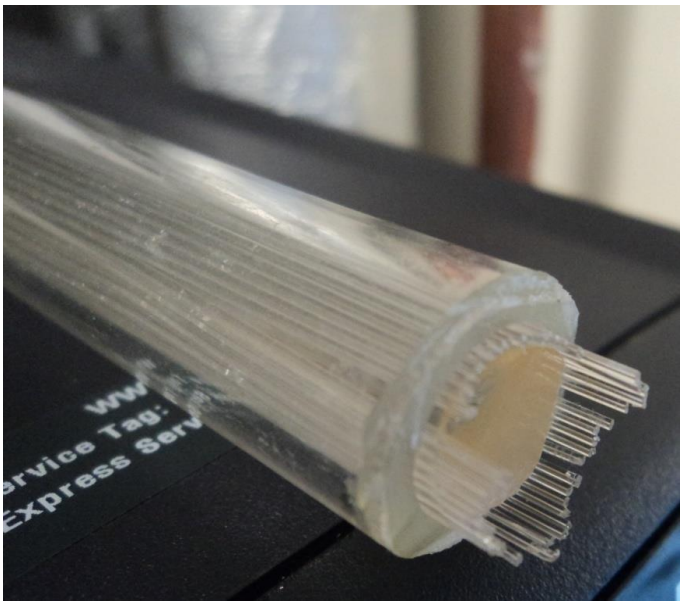

Figure (2.12) Photonic crystal preform with holes filled by PMMA fiber containing indium wire.

2.4 Measuring indium diameter and fluctuation

Optical microscope was used for investigate the produced fiber in each step. In order to test the fiber under the microscope the fiber should be cut sharply with blade.

For sub micrometer indium wire (obtained from third drawing) Scanning Electron Microscope (SEM) model Zeiss EVO 50 was used. Samples were prepared for investigation under the SEM by dissolving the polymer completely using a 1:1:8 volume ratio of water, methyl isobutyl ketone and acetone first. The remaining indium was coated with gold reflective layer.

2.5 Measuring Preform Temperature Profile

In order to simulate the growth of the instability, viscosity of the materials, as well as, interfacial tension should be calculated along the preform during the drawing inside the furnace. To measure the temperature along

the neckdown profile a thermocouple was fixed inside 6mm/12mm PMMA tube. The temperature was recorded along the drawing starting from the top iris of the furnace to the end of the hot zone of the furnace where the fiber is cooled down. This procedure, shown in figure (2.13), has been carried out for different conditions which is listed in table (2.1) and the result will presented in the next chapter

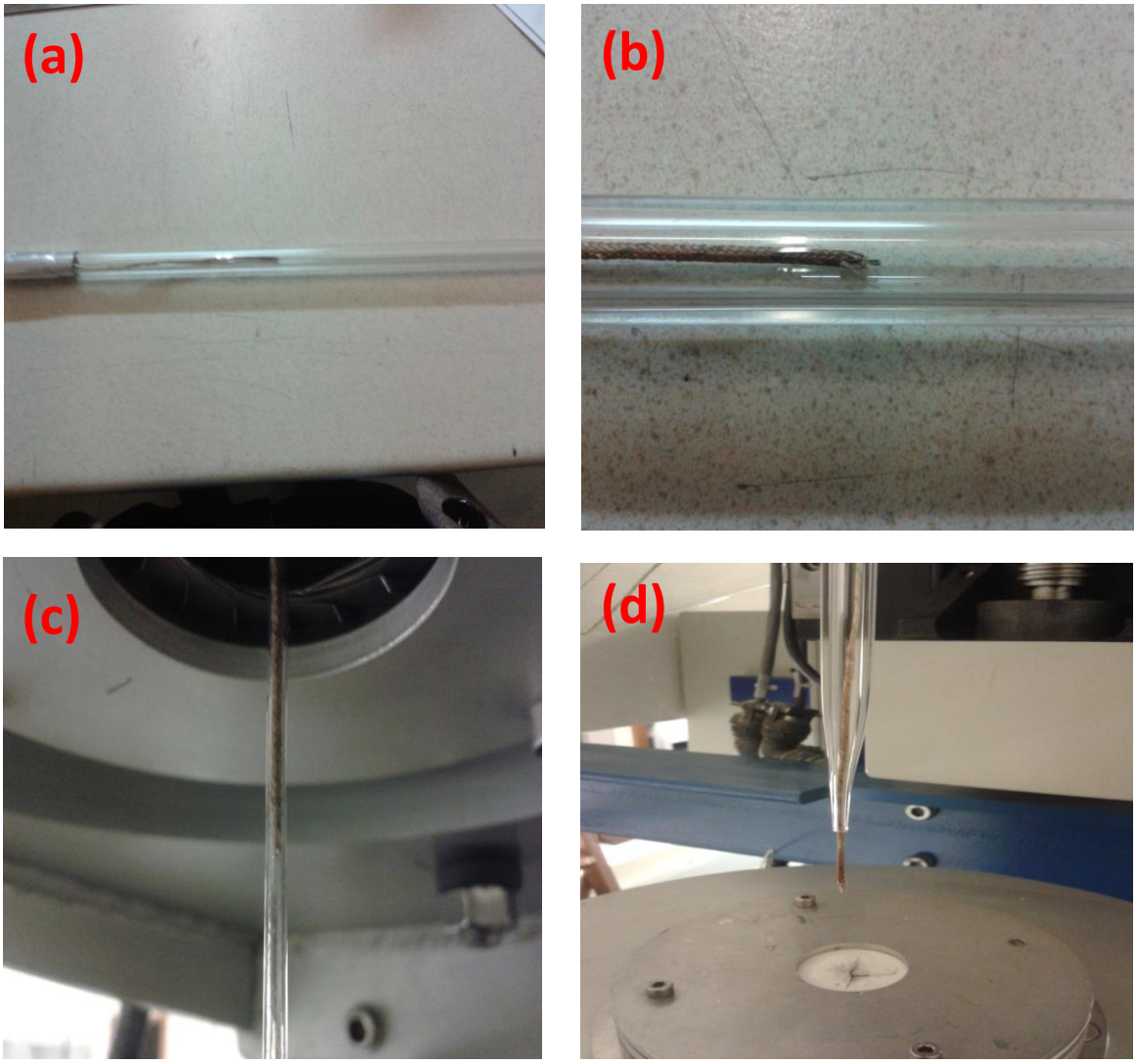

Figure (2.13) a,b- Preparing the thermocouple in PMMA tube, c- Neckdown of the PMMA on the bottom of the furnace, D- neckdown of the PMMA with thermocouple after pulling outside the furnace

Table (2.3) Conditions for Furnace temperature profile measurement

Set Temp. (°C) / Feed speed (mm/sec)	180	190
2	X	X
4	X	X

Chapter Three: Results and Discussion

3.1 Introduction

Indium wire and PMMA represent the ingredient of the fabricated metamaterials in the presented work. A fiber drawing technique was employed to draw the preform. During drawing to a subwavelength range (below 1um), a break up occurs inside the produced fiber. Such phenomenon called Plateau-Rayleigh instability

Tomotika model for the growth in the perturbation in the surface of fluid extended inside another fluid has been modified to describe the fluctuations (instability) of inner core diameter for metamaterials drawing inside radiative furnace.

Modified Tomotika model for the growth of the instability was used to investigate the instability of the indium wire diameter. The investigated diameter was produced by co-drawing of indium metal embedded in a PMMA polymer to fabricate wire metamaterials. PMMA and indium have relatively same glass transition temperature.

The observed instability during metamaterials wire fabrication was studied using the Matlab simulation program for the growth of this instability. To study the effect of different drawing conditions, special case was considered by neglecting the effect of wavelength of perturbation for the small drawing ratio.

Then a complete description were studied. Changes with the wavelength of the perturbation throughout deep drawing to sub μm scale accomplished by third stack and drawing process were considered. The outcome from

the simulated model was compared with the experimental results obtained from scanning electron microscope.

Effects those may give rise to the original fluctuations, like oxidation, which is then amplified by the surface tension will be discussed also.

Finally, the simulation for deep subwavelength wave propagation inside wire metamaterials depending on unit cell manipulation was performed. CST microwave studio software has been used to simulate wave propagation inside linear and corner waveguide as well as equal arms (50/50) beam splitter.

3.2 Modifying Tomotika model

Consider Tomotika's model for the instability growth which has been presented in equation (1.19)

$$\ln\left[\frac{\bar{\varepsilon}/a}{\bar{\varepsilon}_0/a_0}\right] = \frac{\sigma x_0^{1/3}}{3\mu a_0 C}\int_x^{x_0} x^{-\frac{4}{3}}(1-x^2)\Phi(x,\mu'/\mu)dx$$

This formulation as presented has several limitations as it is specific to an exponentially decreasing radius, as well as constant fluid parameters. For the case of interest here – fiber drawing in a furnace – a specific profile for the evolution of the radius will be achieved, and the viscosity and surface tension will vary along the draw through their dependence on temperature. Consequently, we consider an arbitrary profile for the radius through scaling factors $f(t)$ or $g(z)$, as a function of time t or position along the furnace (i.e. the direction of elongation) z , such that

$$a = a_0 f(t) = a_0 g(z).$$

This allows other parameters to be similarly defined, e.g. $x = x_0 f^3(t) = x_0 g^3(z)$, and for the evolution of the fluctuation of a particular initial wavenumber to be considered more intuitively over time or position throughout the draw process,

$$\ln\left[\frac{\bar{\varepsilon}/a}{\bar{\varepsilon}_0/a_0}\right] = \frac{1}{2}\int_0^{t'} \frac{\sigma}{\mu}\frac{1}{a}(1-x^2)\Phi(x,\mu'/\mu)dt = \frac{1}{2v_i}\int_0^{z'} \frac{\sigma}{\mu}\frac{1}{a} g^2(1-x^2)\Phi(x,\mu'/\mu)dz, \tag{3.1}$$

Where the dependence of the parameters inside the integral on f, t, g, or z is implicit and $\Phi(x)$ was defined previously in chapter one.

The velocity of the fluid along the direction of elongation $dz/dt = v_i/g^2(z)$ is determined by the velocity of the preform into the furnace v_i and the scaling factor $g(z)$ by conservation of mass. Also, the fibre is drawn to a particular final diameter. Re-arranging equation (3.1) for the time domain

$$\frac{\bar{\varepsilon}/a}{\bar{\varepsilon}_0/a_0} = e^{\frac{1}{2}\int_0^{t'} \frac{\sigma}{\mu a}(1-x^2)\Phi(x,\mu'/\mu)dt} \tag{3.2}$$

Again denote $n = \frac{\sigma}{2\mu a}(1-x^2)\Phi(x,\mu'/\mu)$ as the rate of growth of the instability along the time

$$\frac{\bar{\varepsilon}/a}{\bar{\varepsilon}_0/a_0} = e^{\int_0^{t'} \mathrm{n}\, dt} \tag{3.3}$$

If we consider the term $\frac{\sigma}{2\mu a}$ is constant for a given temperature. By plotting $(1-x^2)\Phi(x,\mu'/\mu)$ as a function of x as shown in figure (3.1) and taking $\mu'/\mu \sim 10^{-8}$ corresponding to nominal values of the PMMA and indium

viscosities of 10^5 Pa.s and 10^{-3} Pa.s, respectively, in turn corresponding to the typical drawing temperature of approximately 200° C.

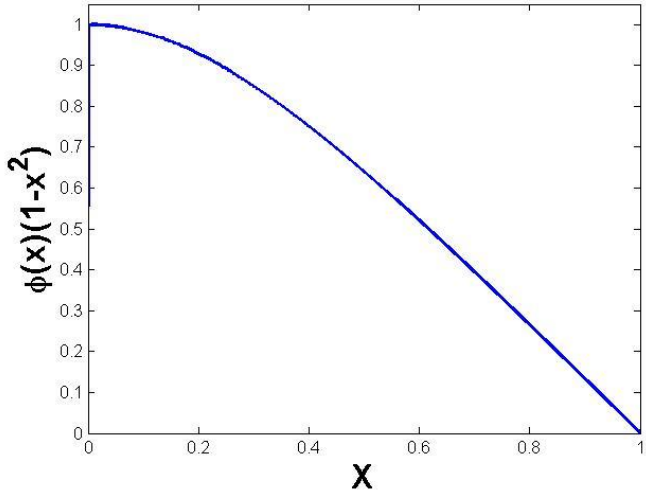

Figure (3.1) $(1-x^2)\Phi(x,\mu'/\mu)$ as a function of x corresponding to $\mu'/\mu \sim 10^{-8}$

For this viscosity ratio $\mu'/\mu \sim 10^{-8}$ the shape of the curve is clearly modified with respect to figure (1.8) where there is no clear maximum value, rather than the maximum gain value is shared by a range of wavelengths. These wavelengths will compete each other to break-up the filament wire.

Shabahang et al. proposed the break up occurred at regular fashion [98], while the present model indicates that the break up took place at random intervals. When the work extend to draw the fiber to sub μm the SEM picture reveals another story as will be discussed later.

The instability growth may only occur whilst the metal is in the liquid phase, and stops when the fiber exits the furnace and cooling. Furthermore, the viscosity of the polymer appearing in the exponent,

varies exponentially with temperature, also the interfacial tension between the indium and PMMA liquids vary with temperature. Material parameters as a function of temperature T (in Kelvin) were defined as

$$\mu(T) = 3.08 \times 10^{-14} e^{(20270/T)} \text{ [Pa.s]} \quad (3.4)$$

$$\mu'(T) = 3.02 \times 10^{-4} e^{(800/T)} \text{ [Pa.s]} \quad (3.5)$$

$$\sigma(T) = 0.546 - 9 \times 10^{-5} T \text{ [N/m]} \quad (3.6)$$

with $\mu(T)$from a fit to experimentally measured viscosity data for PMMA [101], and the indium parameters from Ref. [102], [103].

To modeling the instability growth, the temperature profile inside the furnace has to be considered, to do so the temperature profile was recorded at different feeding conditions as will be described in the next section.

This analysis cannot be used directly as a predictive tool, as the profile that results from certain draw conditions $a(z)$ cannot be easily determined in advance. Profile shape depends on the feed speed, furnace temperature, preform size and final fiber size, as well as the thermal conductivity of the materials and the efficiency of heat transfer processes. As the instability growth is extremely sensitive to the radius of the wires, the profile must be known exactly.

3.3 Furnace Temperature Profile

In order to modeling the instability growth with the indium diameter during drawing process, the temperature profile has to be recorded inside the furnace as it related directly to the viscosity of the PMMA as well as the interfacial tension between the two fluids (PMMA and indium).

Temperature profile for 180° C set point at different feed speed 2mm/min and 4mm/min was illustrated in figure (3.2).

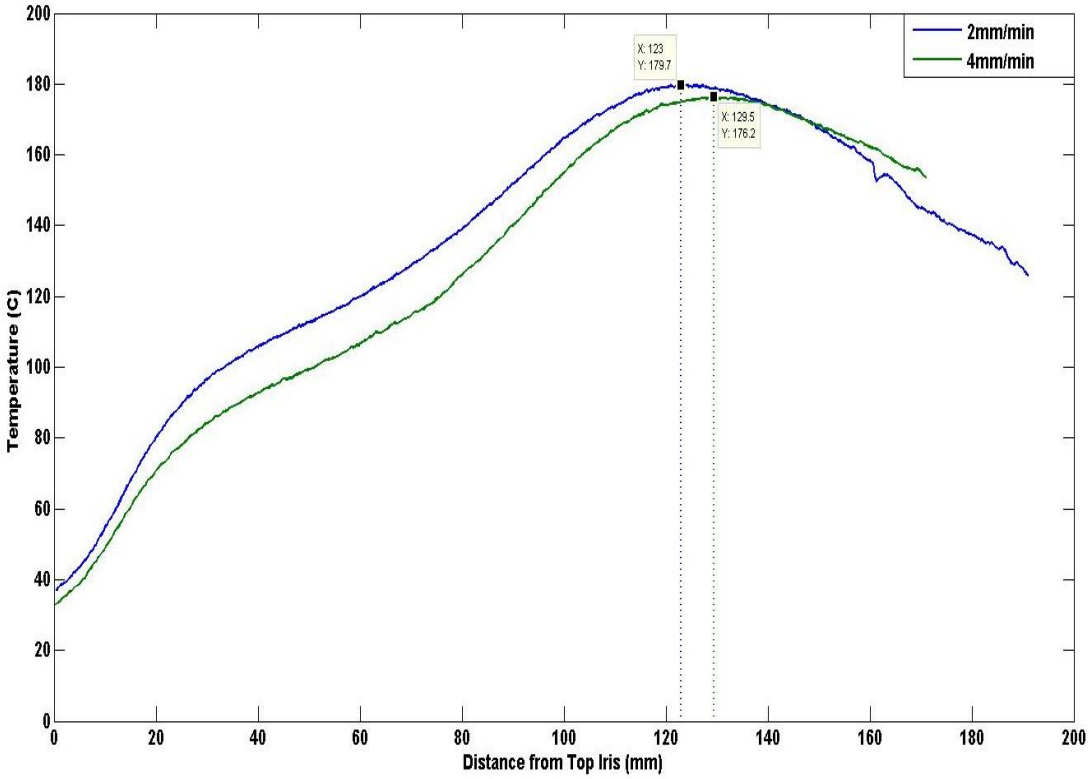

Figure (3.2) Temperature profile for 12/6 mm PMMA tube inside the furnace for the set point 180 °C and feeding speeds 2mm/min and 4mm/min

Figure (3.2) shows the shift of the maximum temperature 176.1 °C in the case of feeding speed 4mm/min toward the bottom of the furnace. While for lower feeding speed 2mm/min the preform reaches higher maximum temperature 179.7° C first. This is obvious because there will be enough time for heat accumulation. Thus at lower temperature slow feeding rate is preferable so as the produced fiber dose not snap during the drawing process at by high tension with at more viscous fluid. Figure (3.3) represents the temperature profile for two set points 180 °C and 190° C at fixed feed speed 2mm/min

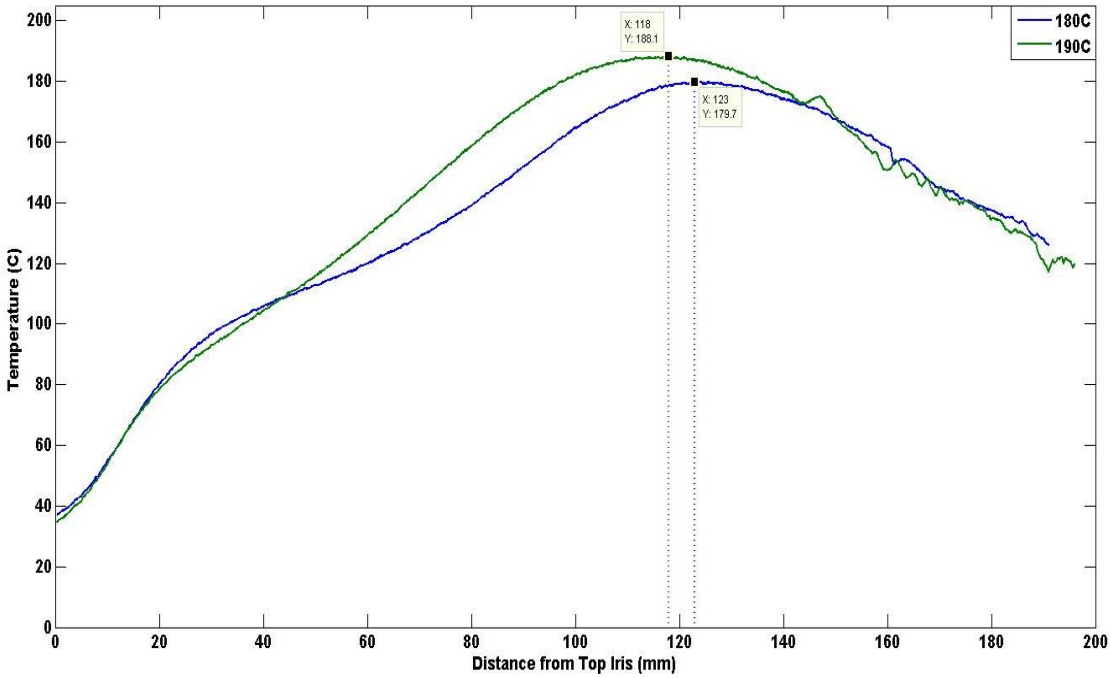

Figure (3.3) Temperature profile for 12/6 mm PMMA tube inside the furnace for two set points 180 C, 190° C and feeding speed 2mm/min.

Figure 3.3 depicts the shift of the center of the temperature profile at 190° C (114.5mm from the top iris) towards the top iris of the furnace with respect to 180° C (124.5mm from the top iris). Both variance have same feeding rate. It's clear that the PMMA in the case of 190° C needs less time to heat up. Increasing the furnace set point temperature can compensate the fast feed problem of high tension.

Increasing the temperature inside the furnace for long time leads to less viscosity and thus high instability as observed in equation (3.4). This can be done by reducing the heat zone inside the furnace by 30 mm (heat zone length from 90 mm to 60 mm) and fixing the other parameters at 190° C and 2mm/min feed speed as it is shown in figure (3.4). But reducing the heat zone length leads to insufficient time for heating up and maximum temperature obtained was 177° C with a clear shift towards the bottom of

the furnace about 20 mm lower than the unmodified one. A snap will appear in the fiber during the drawing process even with relatively low feed speed.

From the aforementioned results, one can conclude that it's not easy to predict the suitable set temperature or feed speed separately. With the simulation, only the liquid phase has been taken during calculations. This part of the profile where PMMA has a temperature more than 160° C. Thus both PMMA and the indium wire were molten and the drawing process took place at fluid state.

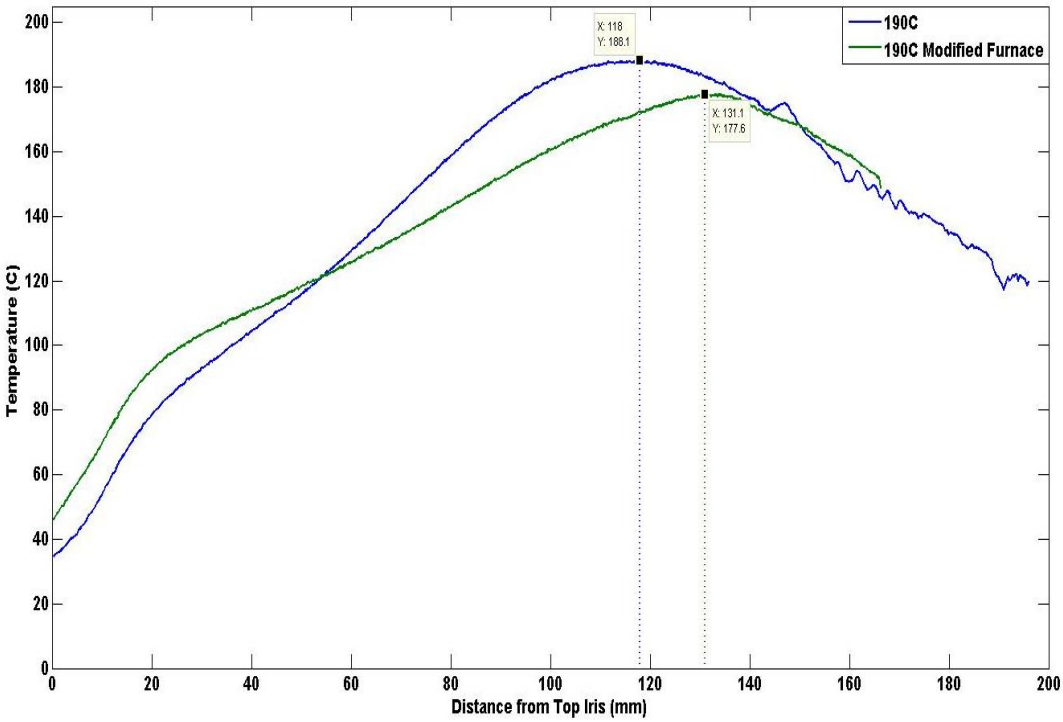

Figure (3.4) Temperature profile for 12/6 mm PMMA tube inside the furnace for the set point 190° C and feeding speed 2mm/min considering modified and unmodified heat zoon inside the furnace

3.4 Neckdown Profile for PMMA Tube

Neckdown profile describes how the diameter of the fiber changes as a function of time or position during the drawing process. At different drawing conditions not only the profile differs in shape, but its position in

the furnace (and hence the temperature at a given diameter) also differs. So returning to equation (3.2) these different neckdown can give different instability growth

In order to investigate how the neckdown profile affects by both the set temperature of the furnace and the feeding speed, set of draws were carried out to PMMA tubes with dimensions of 12 mm outer diameter and 6 mm inner diameter. They had been drawn to an outer diameter of 300 µm fiber at different conditions which were illustrated in table (2.1). Figure (3.5) shows a photograph of such profiles, aligned to the same vertical position relative to the furnace.

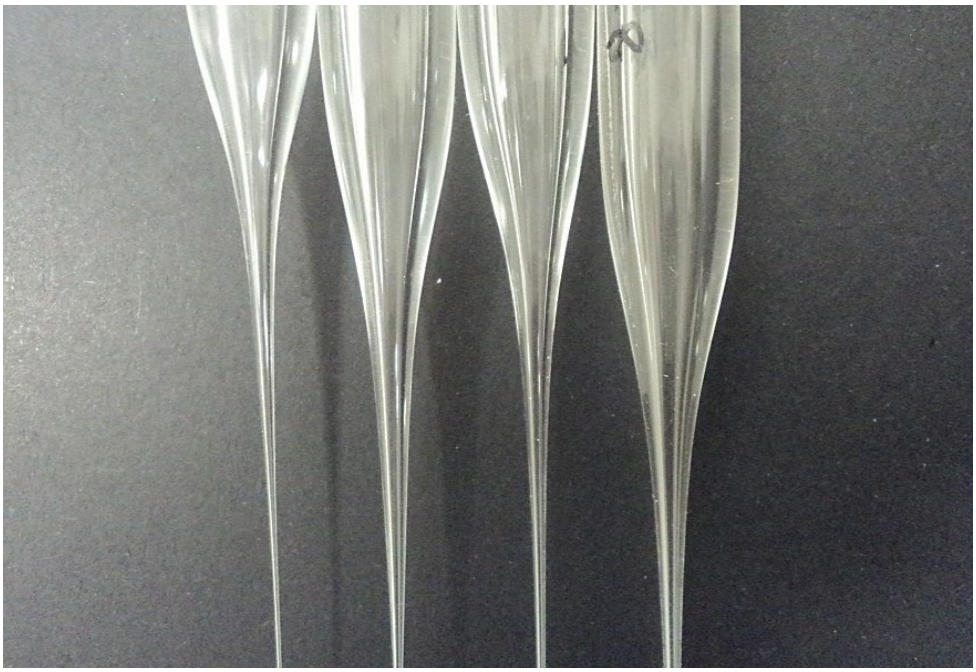

Figure (3.5) Photograph shows shape of the neckdown for the different drawing conditions.

Figure (3.6) shows neckdown profiles for two different feeding speeds of 1mm/min and 4mm/min both drawn at 220° C. The figure clearly shows that at high feeding rate, 4mm/min, more fluid was injected inside the

neckdown and the tube needs about 20 mm (at approximately 70 mm) more than the case of 1mm/min (50 mm) to start tapering the fiber.

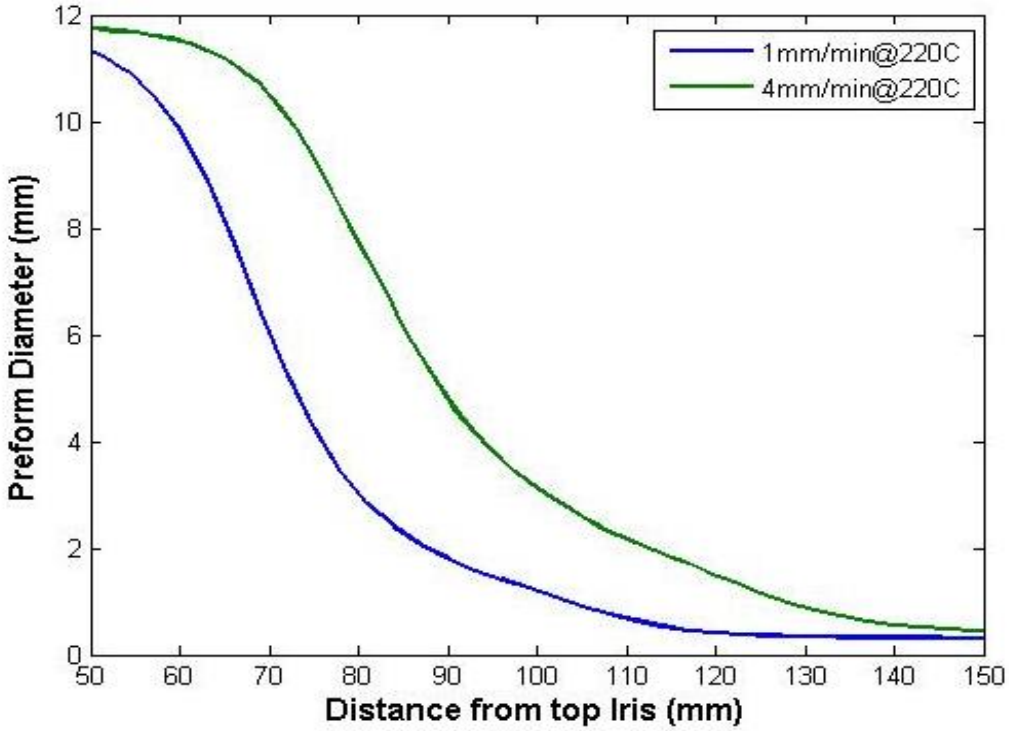

Figure (3.6) Neckdown profiles for two different feeding speed 1mm/min and 4mm/min both at 220° C.

The different neckdown profiles obtained by changing the furnace temperature only (220° C, 230° C and 250° C) with fixing the feeding speed at 4mm/min were illustrated in figure (3.7). This figure clearly shows that an increasing set temperature of the furnace make the material less viscous and starts tapering early to reach the desired diameter

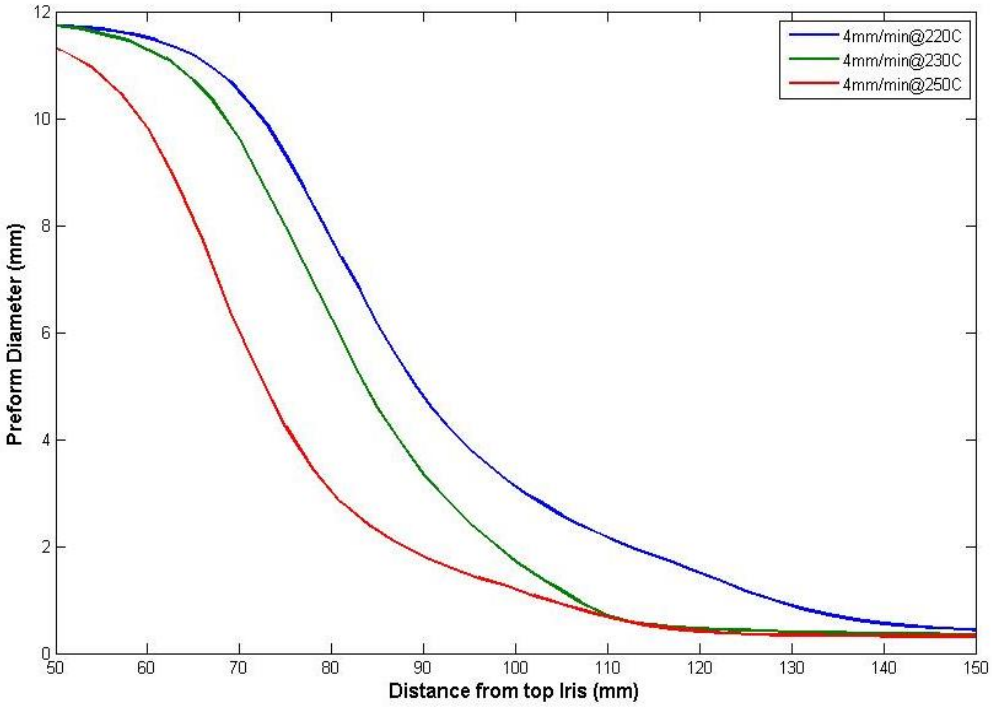

Figure (3.7) Different neckdown profiles obtained by changing the furnace set temperature with fixing the feed speed at 4mm/min.

3.5 Growth of the Instability

Matlab code (appendix A) was built to trace the growth in the instability in the indium wire during the drawing process by means of the neckdown diameter and the furnace temperature at each point inside the furnace.

At first it has been considered a relatively small drawing ratio. The dependence of the growth of the instabilities on their wavelength has been ignored. The wavelength dependence arises from the term $(1-x^2)\Phi(x,\mu'/\mu)$ in Eq. (3.4) which is plotted in Figure 3.1 for $\mu'/\mu \sim 10^{-8}$. It can be seen that range of fluctuation wavelengths corresponding to low x all correspond to the maximum value of 1 for this term. This would give rise to essentially random fluctuations on a scale larger than the wire

radius. Thus, the value of 1 for the term $(1-x^2)\Phi(x,\mu'/\mu)$ was assumed, simplifying Eq. (3.2) to

$$\frac{\bar{\varepsilon}/a}{\bar{\varepsilon}_0/a_0} = e^{\frac{1}{2}\int_0^{t'}\frac{\sigma}{\mu a}dt} \tag{3.7}$$

Integrating over cumulative effect of the growth of the instability allows the growth to be plotted as a function of wire diameter. The obtained results were compared to experimentally observed perturbation. To do so, the size of the fluctuation ε/a was quantified experimentally by examining the diameters of wire sizes at different cross-sections along a fiber length. The standard deviation in wire diameters divided by the average diameters was used.

Figure (3.8) represents the growth of the instability as a function of wire diameter for the preform of outer diameter 4.64 mm and indium diameter of 1mm with experimentally fluctuation of $\bar{\varepsilon}_0/a_0 = 0.004889$ then drawn to fiber at 190°C with 2mm/min feed speed. The produced indium wire diameter was 85 μm with $\bar{\varepsilon}/a = 0.0215$ inside 378 μm PMMA fiber (cross sections shown in figure 3.9). These values of fluctuation give growth of the instability $(\bar{\varepsilon}/a)\big/(\bar{\varepsilon}_0/a_0)$ in the produced wires equal to 4.397 (mention as * in the figure). Simulated instability growth for preform under consideration reach 1.476 at 85 μm indium wire diameter.

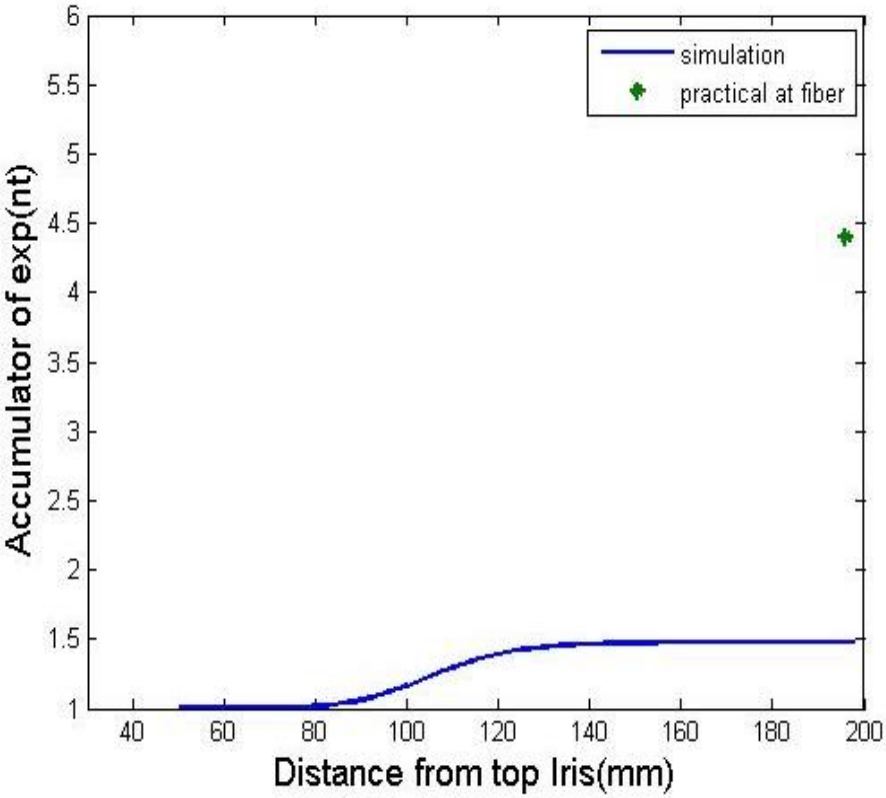

Figure (3.8) Growth of the instability as a function of wire diameter for the preform of outer diameter 4.64 mm and indium diameter = 1mm drawn to fiber at 190° C with 2mm/min feed speed. The produced indium wire 85 µm in 378 µm PMMA fiber

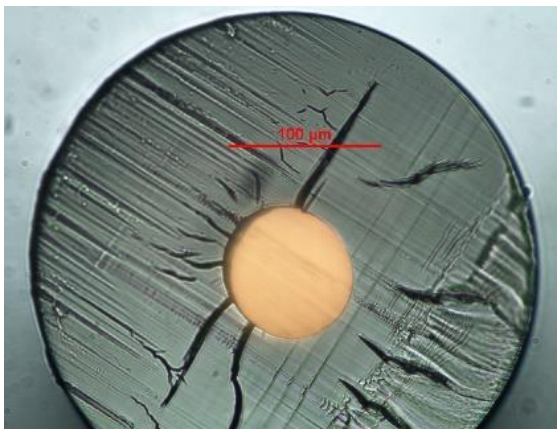

Figure (3.9) Cross section of indium wire embedded inside PMMA jacket from the first drawing indium diameter =85 µm

For the first set of the drawing with different conditions is illustrated in Table (3.4) there is a big mismatch between the experimental and the simulated results

Table (3.4) Growth of instability for different drawing conditions

T(C°)	Feed speed (mm/min)	D(indium)/D(PMMA) (mm/mm)	Final indium diameter (µm)	Instability Growth	
				Simulation	Practical
190	2	1/ 4.64	70	1.447	2.9
183	4	1.1/4.9	80	1.08	5.93
190	2	1.13/12*	68.6	1.3	4.4

* Double jacket

The origin of this difference between simulated and practical results is due to:

a- In the first procedure, the ratio of the indium wire diameter to the PMMA outer diameter was taken. Many fibres were stacked together for preparing preform for the second drawing. When drawing the preform to the fibre, the air gap between the PMMA fibres will alter this ratio (indium wire diameter /PMMA jacket outer diameter). This indicates the large mismatch between the experimental and simulated results. The observed ratio on the fibre was investigated under the microscope, as shown in figure (3.10), have to be considered for reconcile the practical and simulated fluctuation.

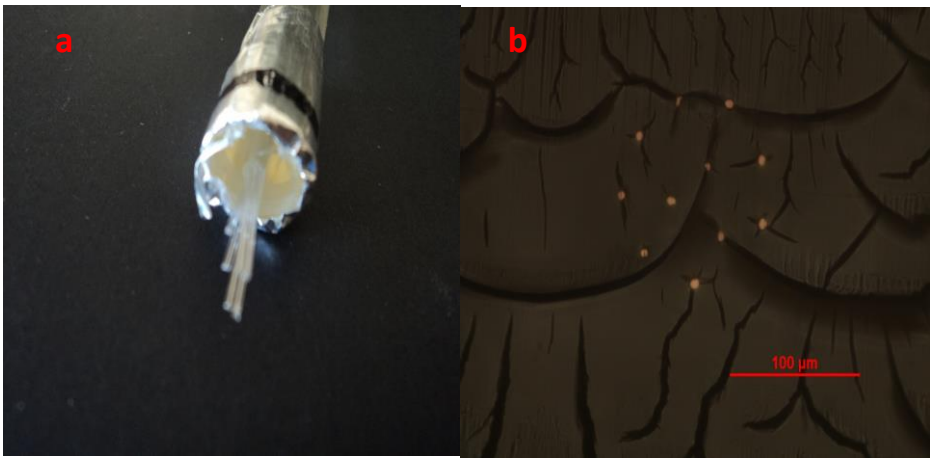

Figure (3.10)-a- Many fiber stack together inside outer jacket for secondary drawing b- Indium wire after drawing inside PMMA matrix.

b- The growth of the instability is highly dependent on the temperature profile inside the furnace as mentioned earlier. Figure (3.11) shows the effect of small temperature variation on the simulated results

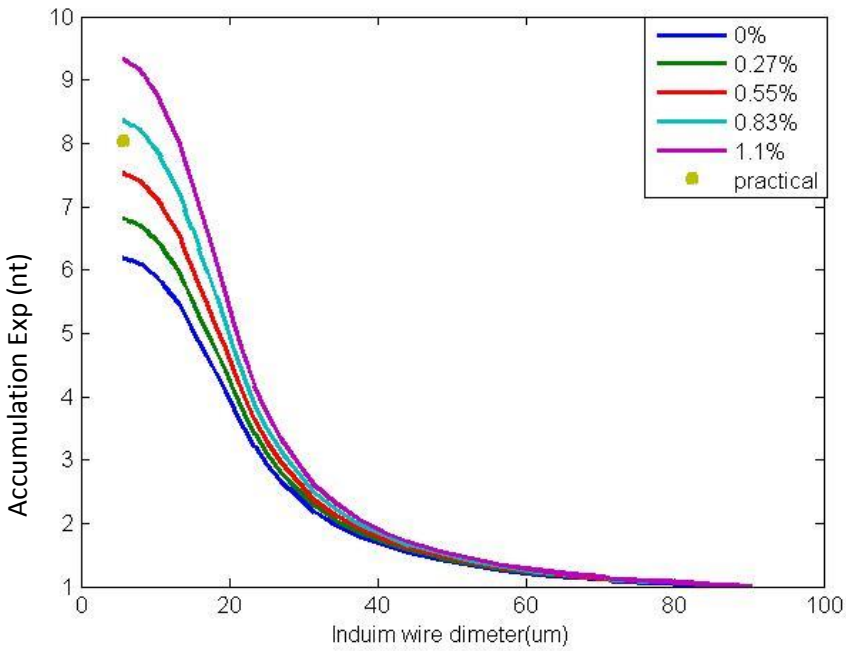

Figure (3.11) Effect of temperature variation on the Instability growth

Figure (3.11) illustrates that variation of 0.83% in furnace temperature can insure matching between simulated and practical result. The reason for this variation might arise from the temperature profile measurement inside the furnace

c- Once the preform drawn to fibre inside the furnace, there will be a heat accumulation before drop of falling down and drawing starting. This deposited heat may promote the instability growth. In the simulation work this effect had not been taken in to account. For experimental work, it's possible to get rid of this side effect by making along preforms. Experimental samples were taken then from the end of the drawn fibre. Figure (3.12) Compares the variation of the indium wire diameter in the case of reaching steady state conditions or not. Present obtained results are compared with previous work carried out by IPOS group [7].

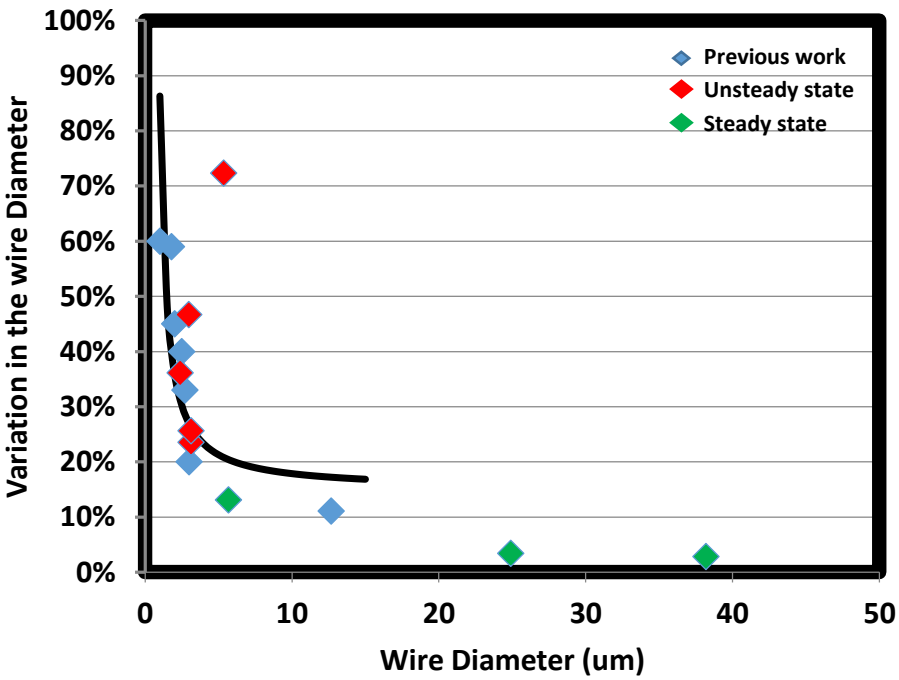

Figure (3.12) Standard of deviation in wire diameter divided by average diameter for different wire diameters

Figure (3.12) clearly shows that reaching a steady state conditions will reduce the fluctuation of the indium wire by get rid of any accumulated heat for the preform during the starting of the drawing process.

To bridge the gap between the experimental and simulation results, the aforementioned three reasons (a, b, and c) were taken in to account

Finally, PMMA tubes of approximately 5 mm outer diameter and 1 mm inner diameter were fabricated and filled with indium by immersing one end of each tube into a liquid indium reservoir, then applying vacuum at the other end. They were drawn to form a single indium wire of 87 µm in diameter inside 640 µm PMMA fiber diameter. Figure (3.13) shows optical microscope image for selected cross sections for the produced indium wire

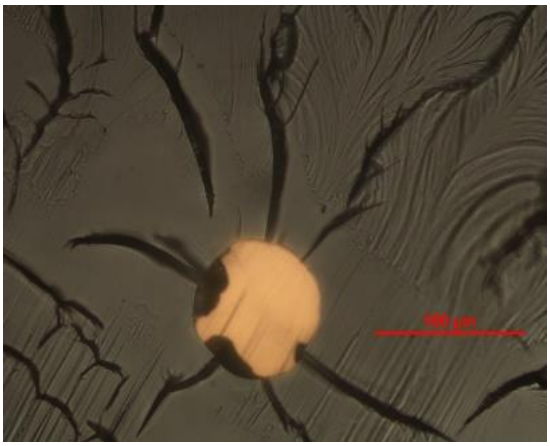

Figure (3.13) optical microscope image for indium wire cross section with diameter of 87 µm

Eleven fibers were stacked inside another PMMA tube of 2.6 mm inner diameter and 11.1 mm outer diameter to form a new preform for secondary drawing. This preform was drawn at 180 °C with a feed speed of 2 mm/min to produce a total fiber diameter of 730 µm. The produced indium wires inside this fiber has a diameter of 5.69 µm.

Figure 3.14 shows optical microscope image for a selected cross section for the produced wires. It is clear that the indium wires are homogenously distributed and of uniform size

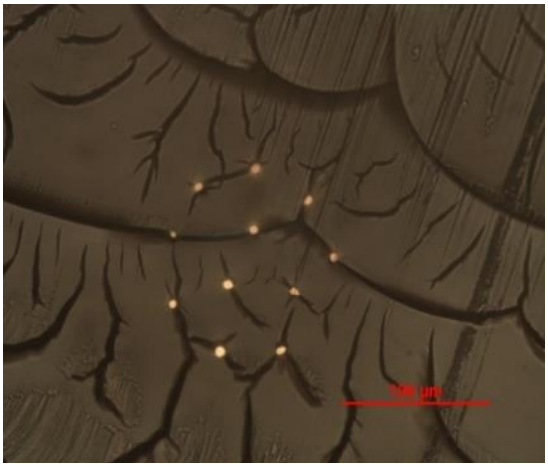

Figure (3.14) Optical microscope image for cross section for the produced wires after second drawing. Indium wires diameter here reaching 5.69 µm.

Figure (3.15) shows optical microscope image for the instability in wires from side view. This figure depicts a clear and very noticeable variation in the diameters along the indium wires

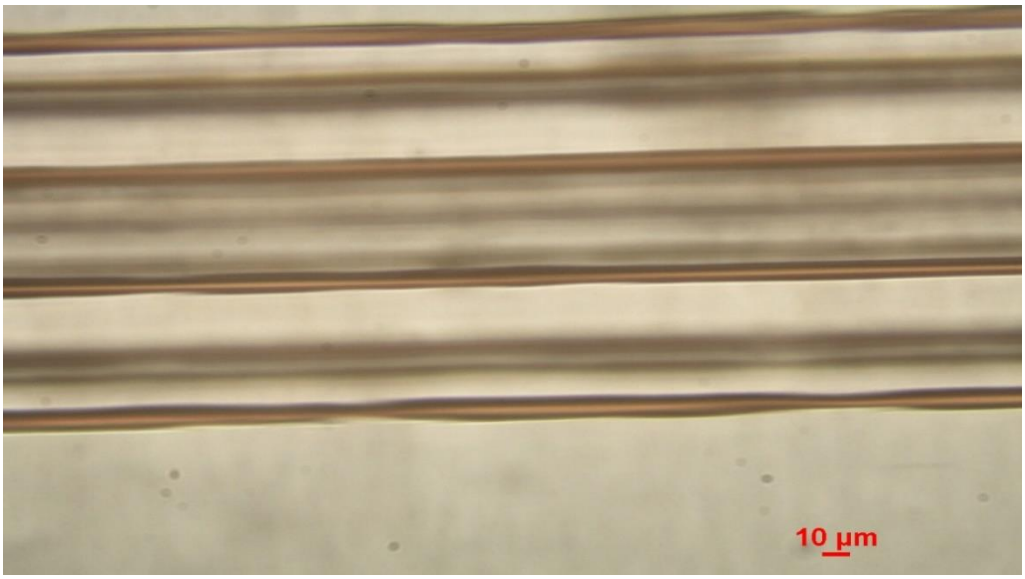

Figure (3.15) Optical microscope image for the instability appears in 5.69 µm indium wires from side view

The result for the mentioned draw is shown in Figure (3.16), in which the variation in wire size increased from $\bar{\varepsilon}_0/\bar{a}_0 = 0.0163$ in the preform to $\bar{\varepsilon}/\bar{a} = 0.131$ in the fibre, i.e. by a factor of 8.

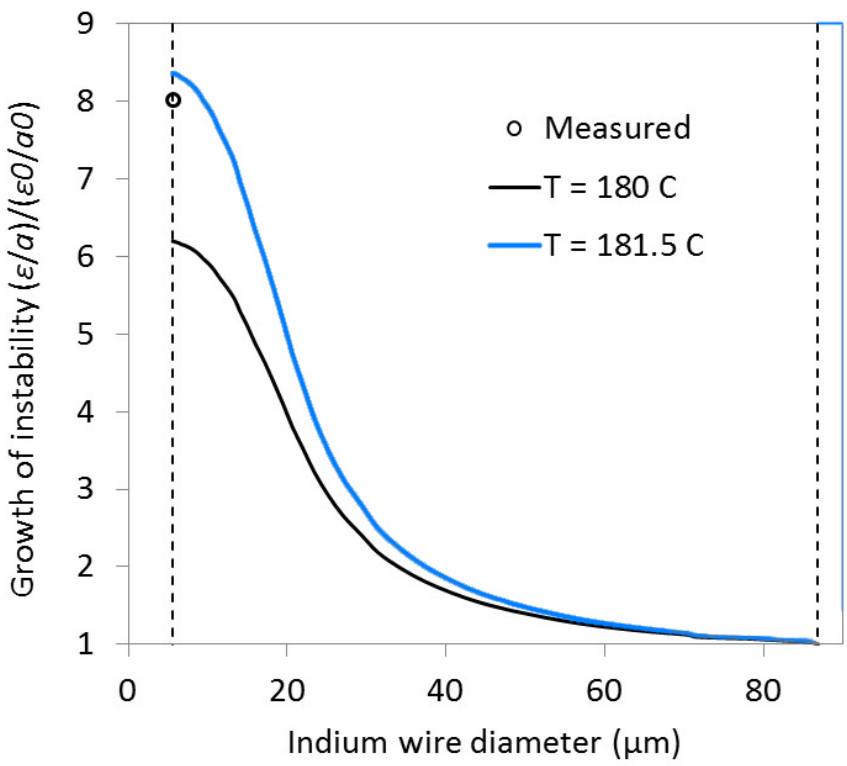

Figure. (3.16) Increase in the fluctuation amplitude as the wire diameter is decreased during the draw from the initial diameter of 87 µm to the final diameter of 5.7 µm. The Measured increase is compared to calculations using Eq. (3.7).

For the growth of the instability plotted as a function of wire diameter shown in Figure. (3.16). However, at first this appears to underestimate the practical growth, predicting a factor of 6.2 instead of 8. Given the sensitivity to the terms in the integral of eq. (3.1), and particularly to the viscosity, the growth was recalculated with an increase in the temperature by 1.5 °C, which indeed gives excellent agreement, predicting a growth

factor of 8.4. Given the assumptions made in determining the temperature, a variation of 1.5 °C is a very reasonable margin of error, hence the observed fluctuations in diameter can be reconciled with the Plateau-Rayleigh instability.

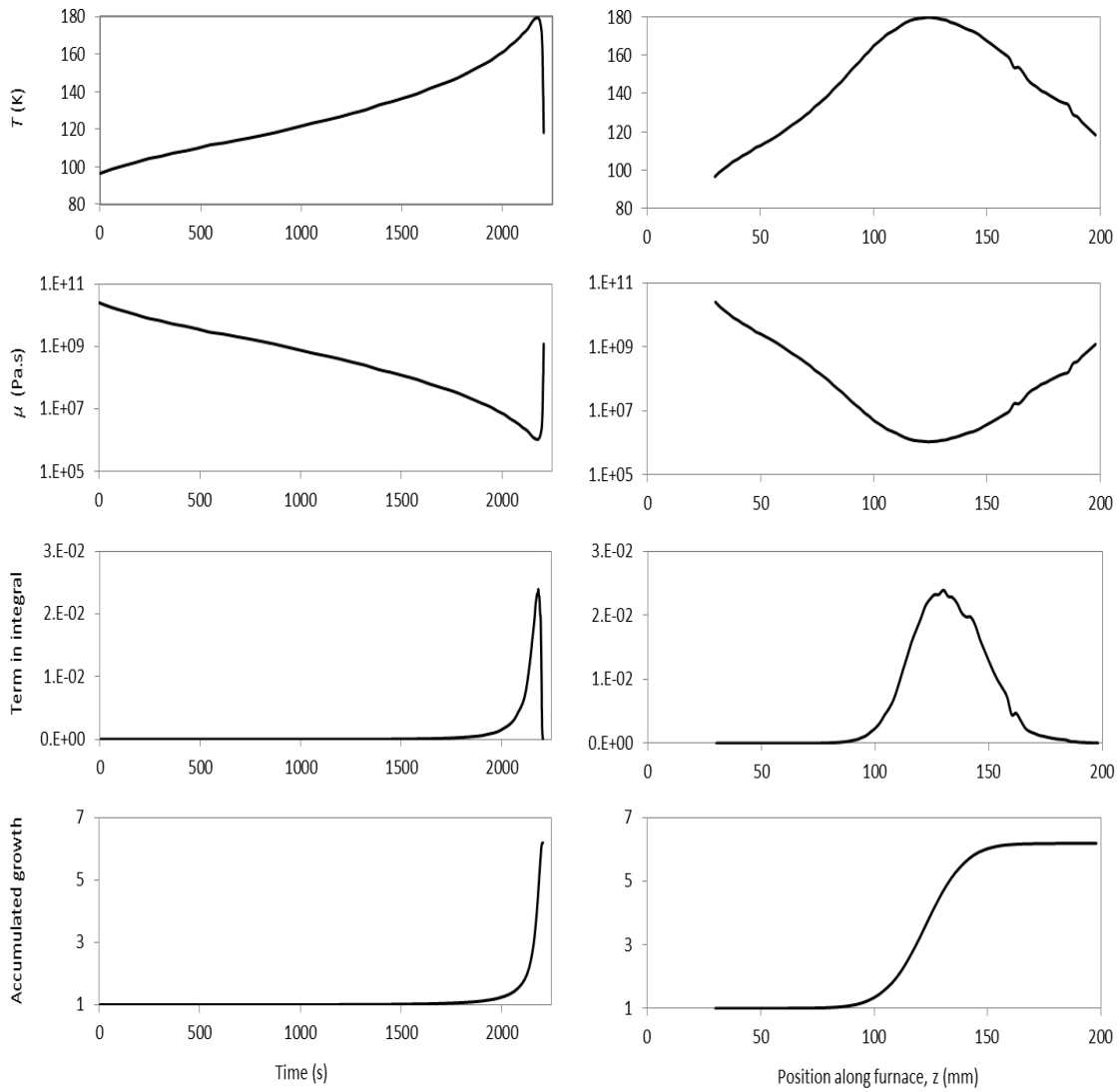

Figure (3.17) Furnace temperature, PMMA viscosity, differential instability growth rate, and accumulated instability growth for the example discussed shown in Figure. (3.16), as function of time (t) and position along the furnace (z). The origin of both axes marks the entry of the preform into the top of the furnace.

Looking more closely at all the relevant parameters in Figure (3.17), the fluctuations are seen to grow most prominently where the temperature is highest and the wire diameter and polymer viscosity are lowest, as expected. Also the time for the main growth in the instability is about 120 (s) as shown in figure (3.18)

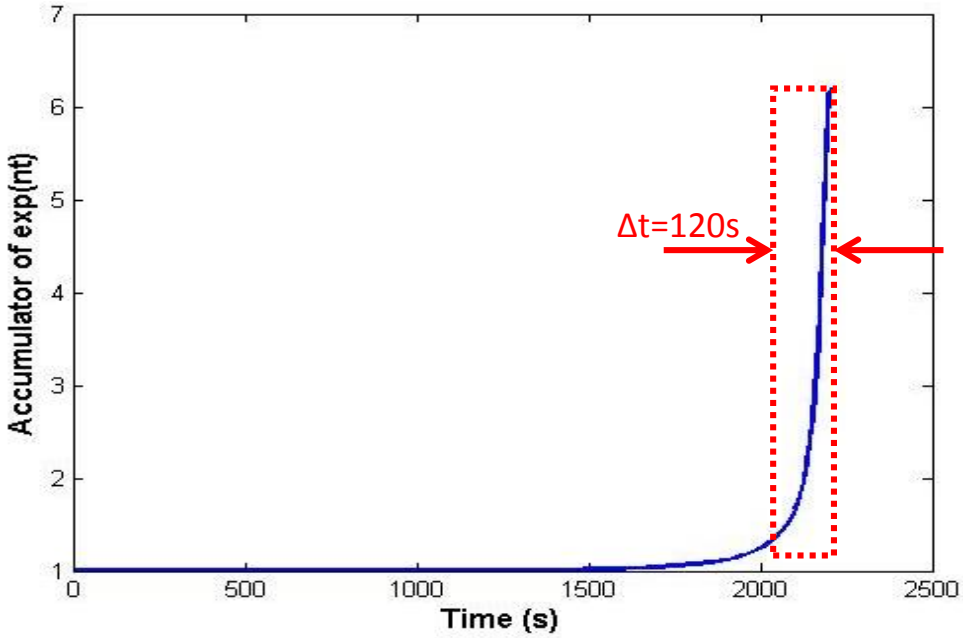

Figure (3.18) Time for main growth approximately 120 second

A final outcome of this first study (with small drawing ratio) was the importance of the draw achieving steady state. Once the draw begins, it requires some time before it reaches the steady state profile and temperature distribution. It was found that only then, as anticipated, could the instability growth be described by modified Tomotika's model.

To investigate the full effect of the instability, including the effect of the instability wavelength, a second study was undertaken, in which a larger drawing ratio was used, with a nominal 'final' wire diameter below 1 µm, to purposely cause the wires to break-up into droplets

3.6 Effect of the wavelength of perturbations

To investigate the origin wavelength of fluctuation λ_0 and whether the wires were broken out in random fashion or periodically, as in [98], the drawing had been extended beyond the breaking limit. Third drawing was performed for the produced fiber inside new PMMA jacket to reach sub μm scale for the indium wires. At this stage the fluctuation become larger than the wire diameter and the wire starts to break up to droplets.

Five fibers with outer diameter of 700 μm containing 26 indium wires (each has diameter of 2.7 μm) were drawn inside PMMA jacket. Jacket has 3.6 mm outer diameter and 0.9 mm inner diameter. The preform then was drawn to fiber with 500 μm outer diameter. This would produce 377nm indium wires diameter.

The produced indium wires were examined under SEM after dissolving polymer completely using a 1:1:8 volume ratio of water, methyl isobutyl ketone and acetone. Figure (3.19) shows the indium wires are broken when investigated under the SEM.

Histogram was recorded for the length of the rice grain-like breaks then these lengths were reflected back to their origin lengths at the time of the broke, as the wires were shrank after broken out, using equations derived from the conservation of material

$$\lambda_{final} = (W_2/W_1)^2 * L, \quad (3.8)$$

$$x = \pi * W_1^3/W_2^2 * L, \quad (3.9)$$

Where W_1: original width of the grain at the time of the broke, W_2: observed width of the grain, L: observed length of the grain, λ_{final}: final perturbation wavelength at the time of the broke

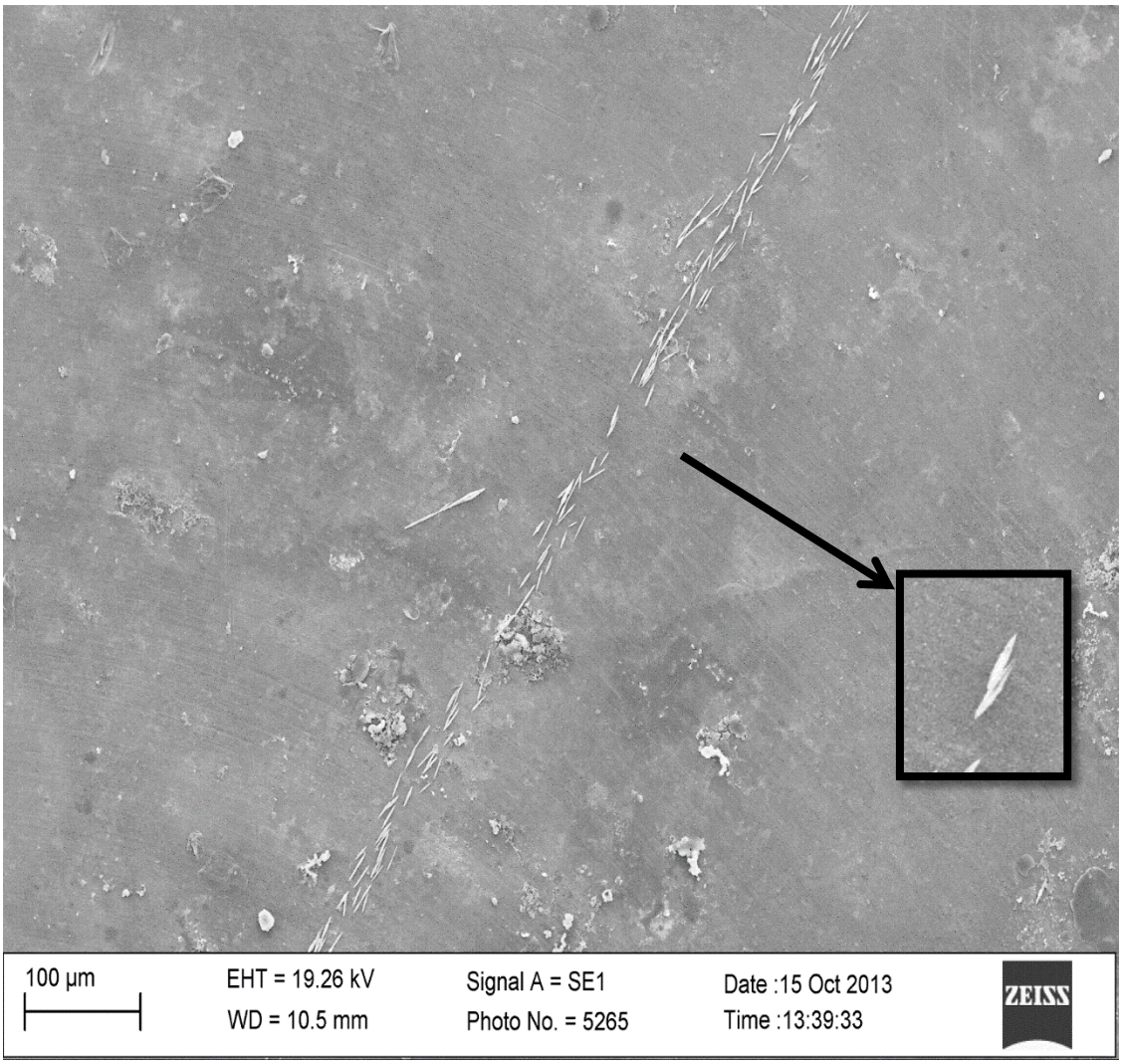

Figure (3.19) indium wires are broken down by the effect of the instability

Figure (3.20) shows the histogram of the calculated $x=R*2\pi/\lambda$, While Figure (3.21) compares these iterative of x to the curve of $(1-x^2)\Phi(x,\mu'/\mu)$ term appeared in modified Tomotika model eq. (3.2). The

inset in figure (3.20) shows $(1-x^2)\Phi(x,\mu'/\mu)$ for the full x scale$(0 \rightarrow 1)$.

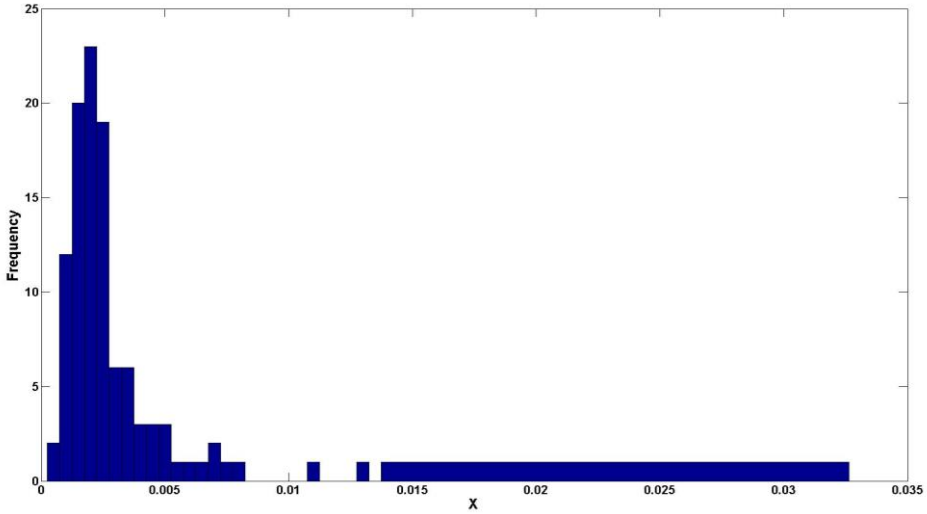

Figure (3.20) Histogram for the *x* measured from the shape of the rice grain-like breaks of indium.

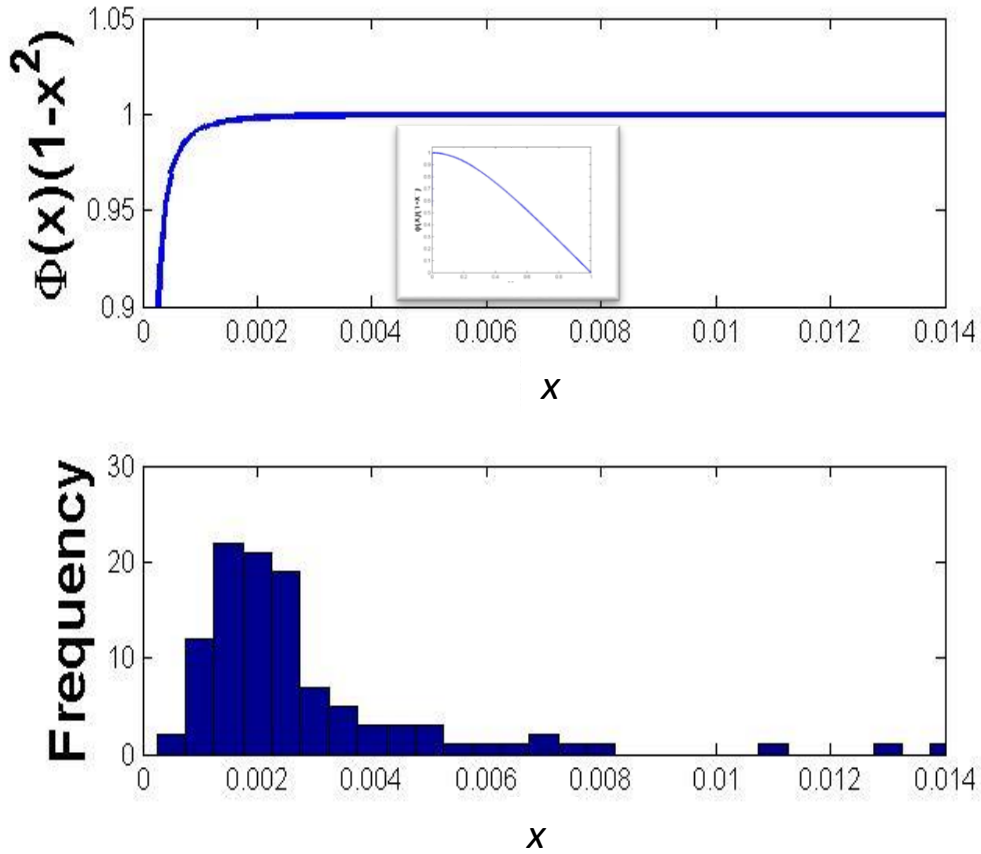

Figure (3.21) Comparing the histogram of x to the $(1-x^2)\Phi\left(x,\frac{\mu'}{\mu}\right)$. The inset shows $(1-x^2)\Phi(x,\mu'/\mu)$ for the full x scale$(0\rightarrow 1)$.

One can conclude two main findings from the graph presented in figure (3.21)

First: only the wavelengths of perturbations with the maximum value of gain rate will appear in the end of the drawing process. This reveals approximately periodic breaks up. Work might be pushed to produce symmetric shape nanoscale indium droplets. Indium nano-particles or producing 3D metamaterials can be achieved from this method.

Second: one can use these values of the wavelength of the perturbation at the breaking point λ_{final} to find the original wavelength of the perturbation λ_o in the preform. Knowing original wavelength of the perturbation λ_o

gives the ability of find the origin of fluctuation. The fluctuation at the beginning might arise from indium oxidation or the roughness of PMMA surface or other reasons. In our case it appears to be 1 nm. which is about the roughness of atomic structure and infer limits to wire dimensions that can be achieved using the chosen material system (PMMA and indium).

To investigate equation (3.2) growth of instability along the preform for different λ_o is presented in figure (3.22). This figure clearly shows that for each λ_o there are different gain rates depending on the wire diameter. However certain λ_o , 1 mm here, is having larger growth rate over all drawing process. This consistent with our observation as the breaks up takes place for certain λ_{final} values.

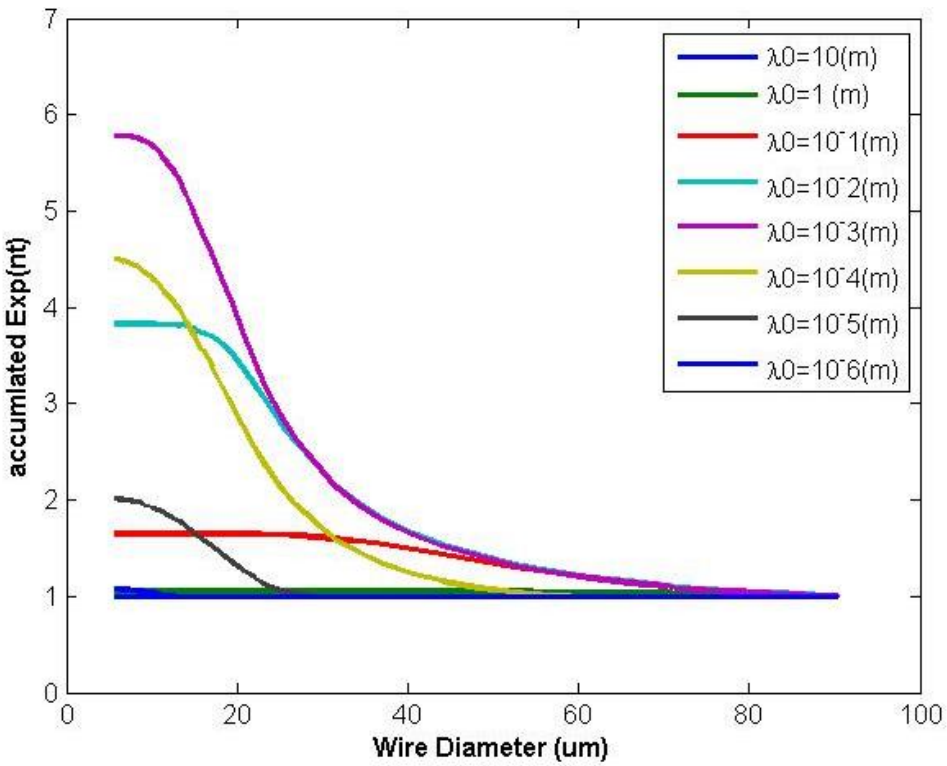

Figure (3.22) Growth of instability as a function of wire diameter for different λ_o

Figure (3.23) shows plot for eq. (3.2) by taking in into account the decrease in the wire diameter as well. Again at certain λ_o the growth was dominated along all drawing process.

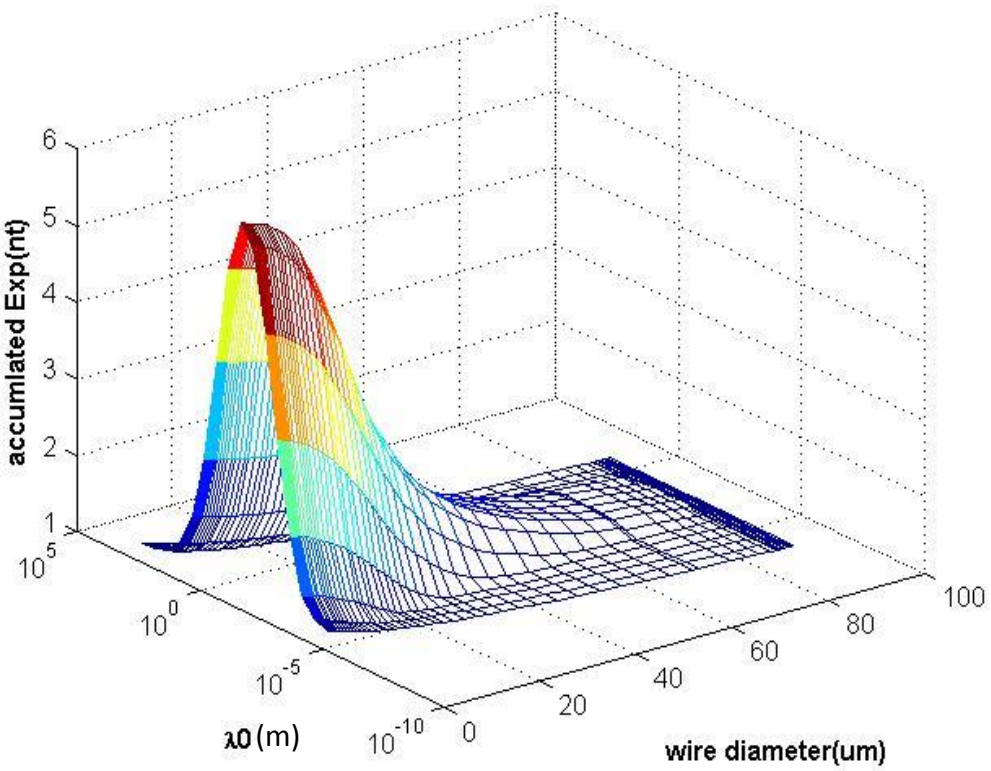

Figure (3.23) Growth of instability as a function of diameter and λ_o and indium wire diameter

3.7 Factors for initial fluctuations

The fluctuation growth takes its origin from $\bar{\varepsilon}_0/a_0$. The initial fluctuation might arise from the oxidation of indium surface contacted directly to the air or PMMA. PMMA is a good absorber for the humidity from the surrounding environment. An experiment of drawing preforms to fiber in the absence of the oxygen was performed. PMMA tube was left in the vacuum furnace at 90 ^oC for 2 days then the furnace was filled with

nitrogen for 2 days. This procedure was repeated for the next 4 days to make sure there's no oxygen inside the furnace. The tube was filled with indium and drawn to fiber with a plenty of nitrogen surrounding the drawing furnace. Fluctuations still exist in the produce fiber and neckdown region as shown in figure (3.24)

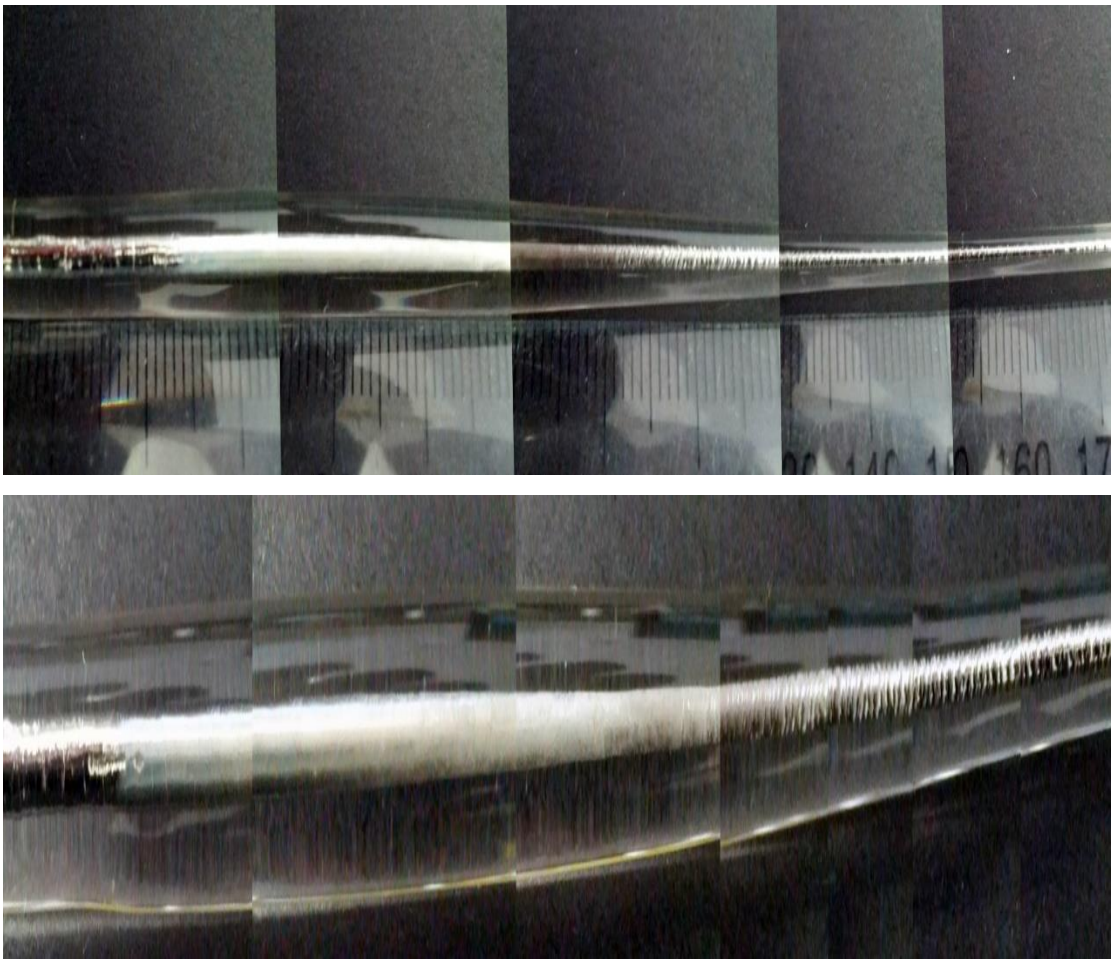

Figure (3.24) Neckdown of the preform drawn with absence of the oxygen to get rid of the indium oxidation

3.8 Controlling wave propagation in subwavelength scale

When we are dealing with the photonic crystals one can control the propagation of light or making light confined in order of the wavelength by disordering unit cell. In the case of metamaterials, when the unit cell is smaller than the wavelength it needs to consider the microscopic parameters of the system ε_r, μ_r. CST microwave studio software was used for modeling the flow of light in subwavelength scale by manipulating unit cell in wire metamaterials. The theory was experimentally verified by Lemoult et. al, [62].

The system under consideration consists of 20x20 identical metallic wires with resonance frequency $f_c = nc/2L$ where c: speed of light in vacum, n: resonance mode number, L=length of the wire (40cm for present work). Figure (3.35) shows the system model while figure (3.26) shows frequency response of such system at the second resonance (*n*=2) at about 720 MHz. Two discrete ports were inserted in the opposite sides to investigate the frequency response. Open space boundary conditions have been considered to get match the experimental results.

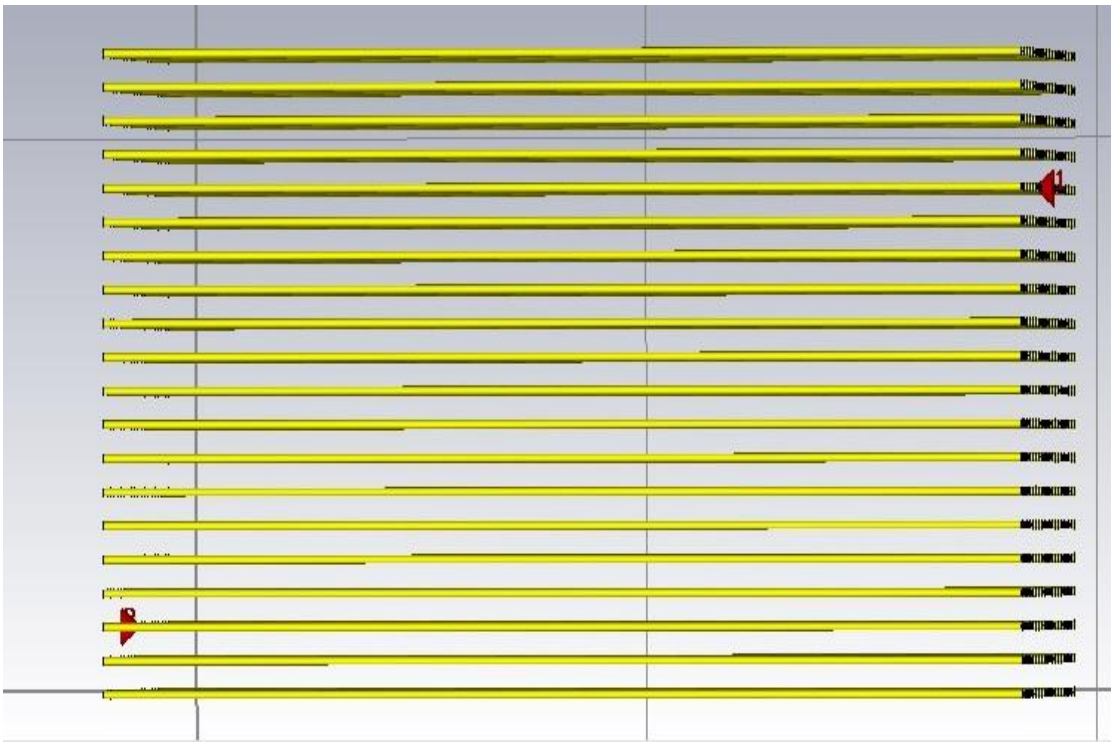

Figure (3.25) Metallic wires with 3 mm diameter, 12mm separation and 40 cm length. Discrete ports were placed in the opposite sides

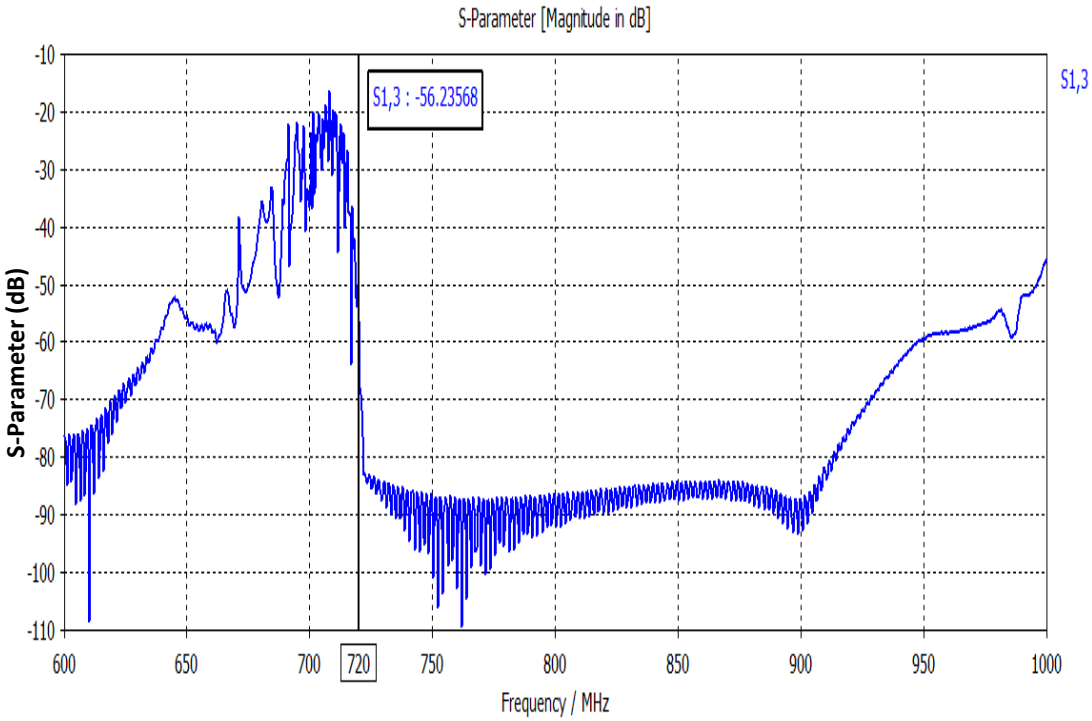

Figure (3.26) Frequency response of the system measured using S21 (dB) parameter for 40 cm. vertical line assign resonace frequency according to $f_c = nc/2L$

Figure (3.26) indicates that there is a clear sharp bandgap above resonant frequency. This band gap finds its origin in the local resonance of the metallic wires. This may lead to very strong near-field interactions between the resonators due to the interference (Fano interference) [104]. Shortening the resonant wire will shift the resonance toward higher frequencies. Figure (3.27) shows the frequency response for the 40, 37 cm wires length systems

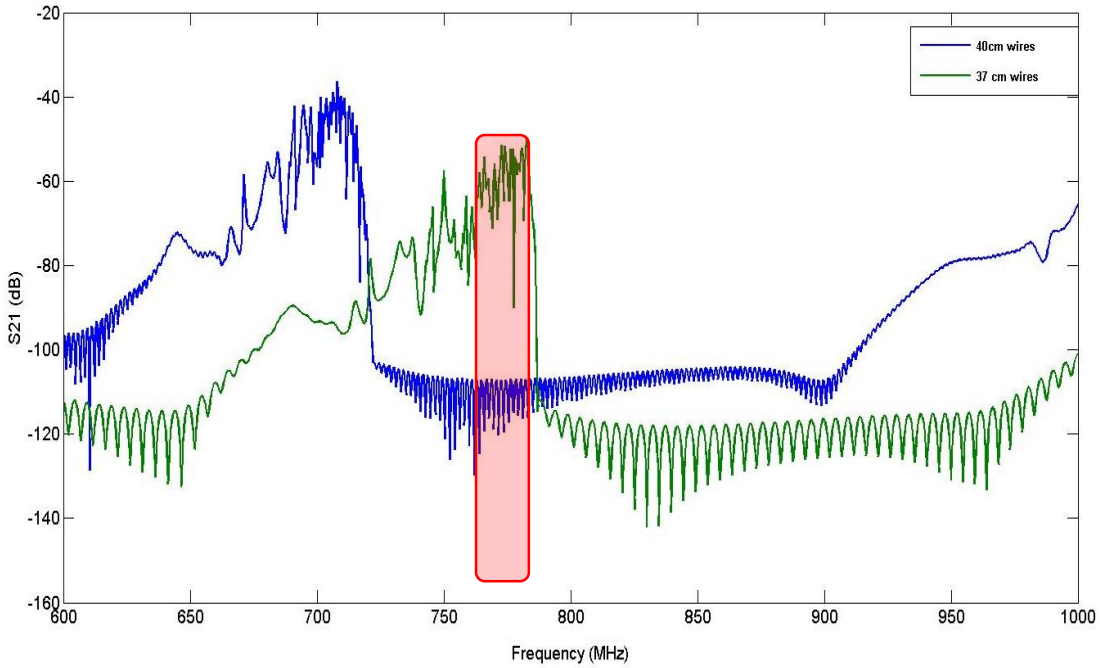

Figure (3.27) Comparing frequency response of the system in the case of 40 cm ,37 cm using S21 (dB) parameter. Red region represents the working region

Figure (3.27), clearly illustrates that at frequency range (760MHz-780MHz marked with red rectangular), the resonance mode at shorter wire (high transmission) has a counterpart bandgap at longer wires.

a- Waveguide

The waveguide (linear or bending) can be simply achieved by shortening a single raw of wires by 3 cm and selecting certain frequency for the

propagating wave. A deep subwavelength guiding was modeled. Figure (3.28) shows the linear waveguide for the wave propagation at deep wavelength ≈2.4 cm. Figure (3.29) illustrate the S21 parameter for the waveguide (used to select the mentioned certain frequency).

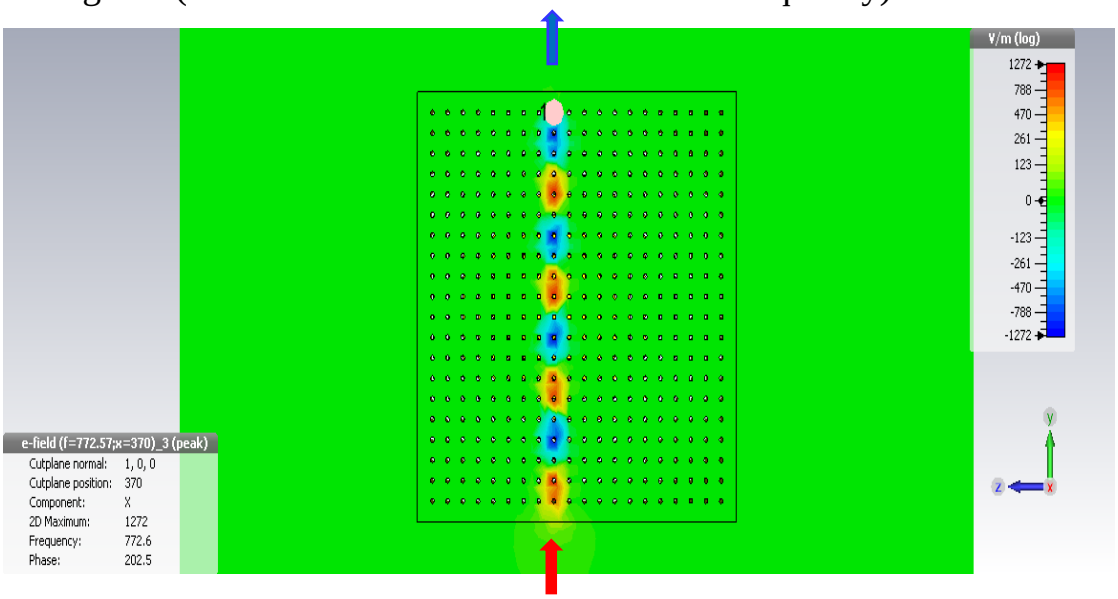

Figure (3.28) 772.59 MHz=38.8 cm wavelength) wave propagation at deep wavelength ≈2.4 cm (linear waveguide)

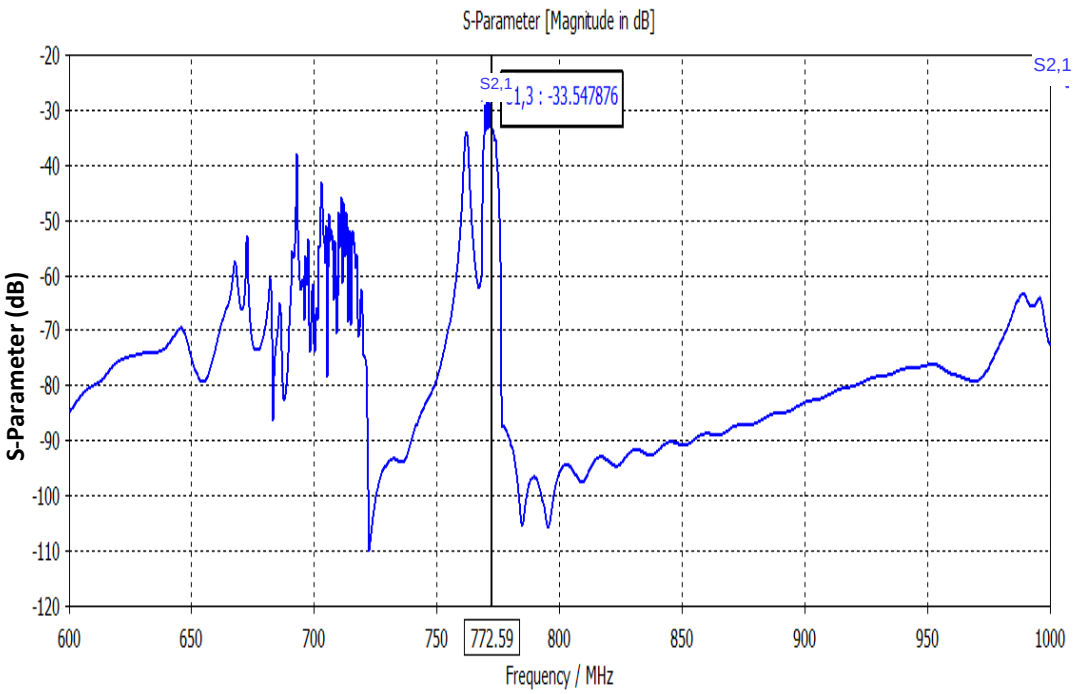

Figure (3.29) S-parameter S31 for the waveguide over 600-1000 MHz 772.59 MHz

Figure (3.30) presents the wave propagation inside 90° bended waveguide for **775.52 MHz** wave. S21 parameter is illustrated in figure (3.31).

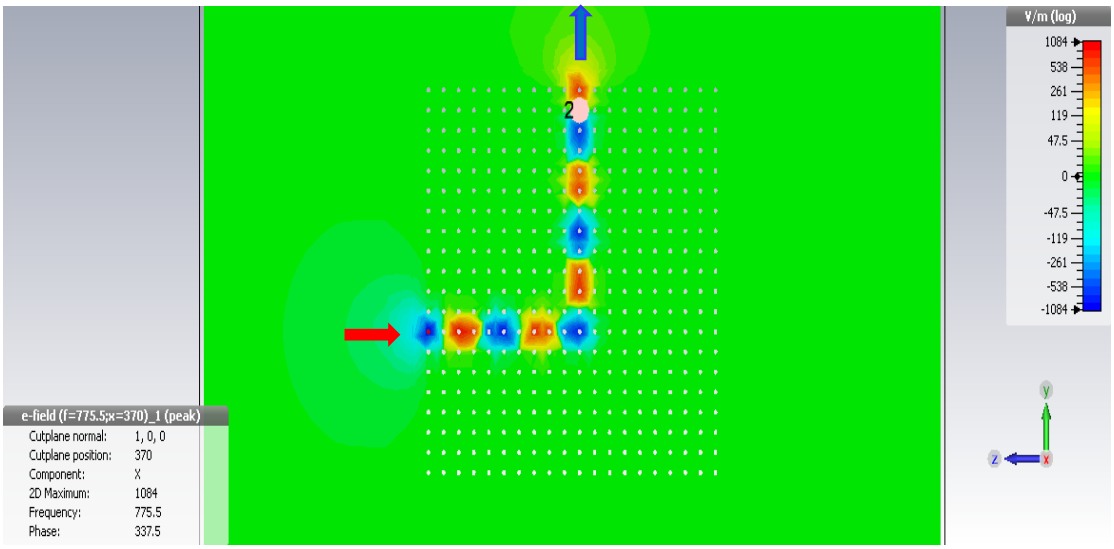

Figure (3.30) 775.52 MHz=38.7 cm wavelength) wave propagation at deep wavelength ≈2.4 cm. (90° bending).

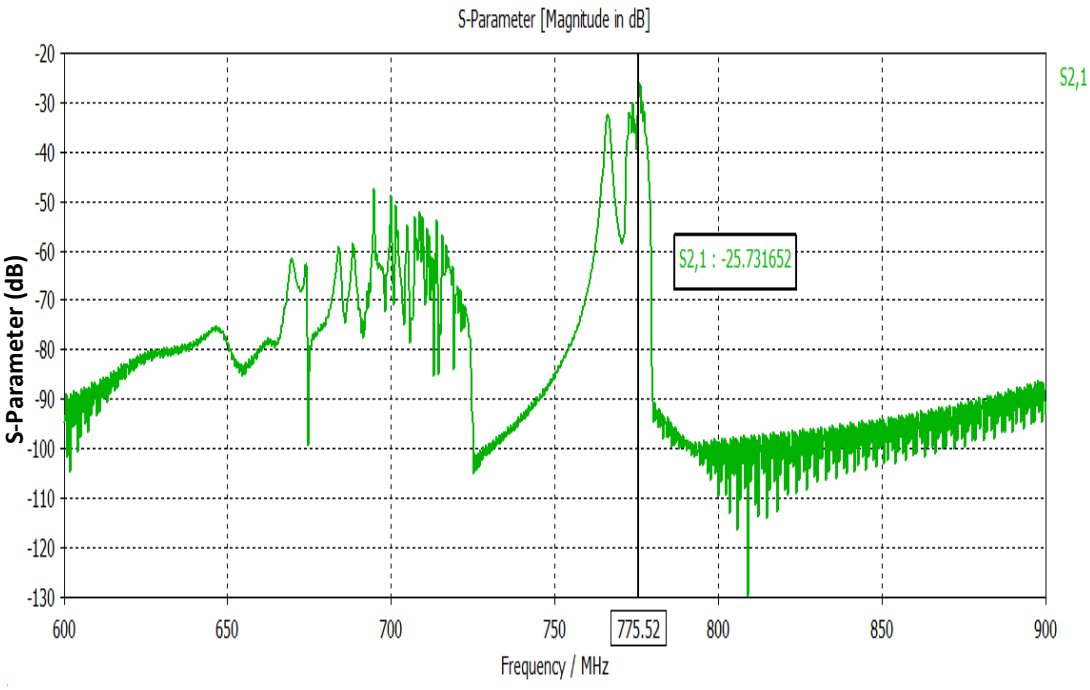

Figure (3.31) S-parameter S31 for the 90° bending over 600-900 MHz 775.52 MHz

b- Beam Splitter

Laser systems employ many optical elements and accessories. Beam splitter are widely used with lasers, photonics and electronic applications. Conventional materials used to construct beam splitters have many drawbacks. Using the metamaterials to build such element will promote their potentials as well as beam splitters under investigation function at deep subwavelength range.

Beam splitter using the same concept of unit cell manipulation was applicable to modeling. Figure (3.32) shows the wave propagation inside the beam splitter at 778 MHz. S21 and S31 for both arm of the splitter where illustrated in figure (3.33) were both arms have equivalent output power (50/50)/

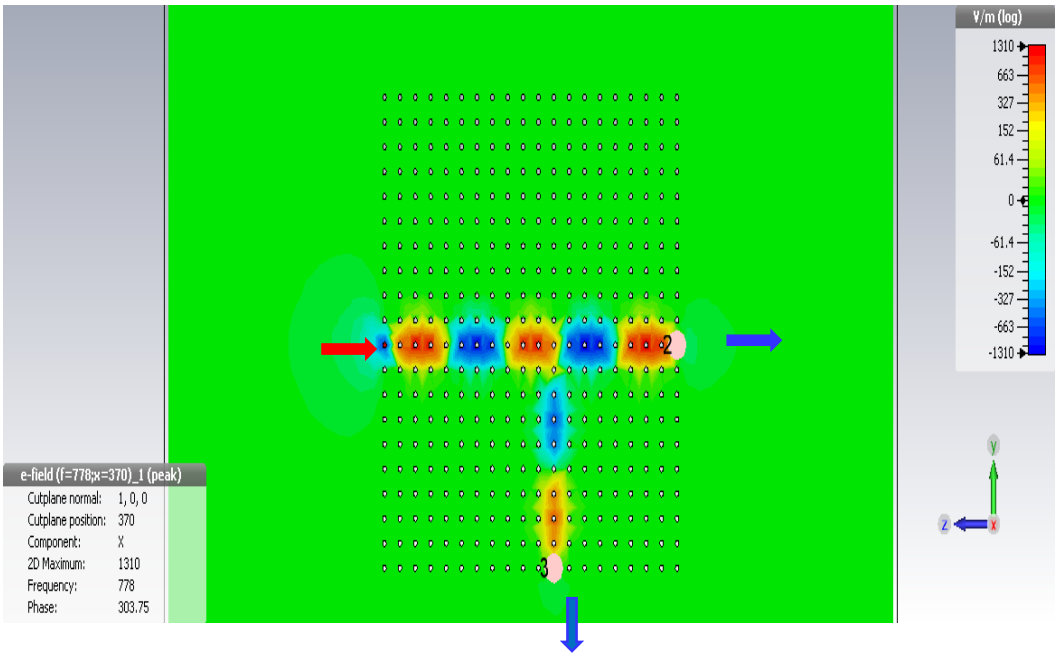

Figure (3.32) 778 MHz=38.5 cm wavelength) wave propagation at beam splitter

Figure (3.33) S-parameters S21, S31 for both arms of beam splitter over 600-900 MHz 778 MHz

A slight frequency shift has been observed for each individual configuration. This was attributed to the physical length of the waveguide [62].

3.9 Conclusions

1- given the limitations and complexity of the indium/ Poly-Methyl Methacrylate (PMMA) system for fabrication wire metamaterials with negative permittivity studied here
2- Reaching steady state conditions by using long preform highly decrease the fluctuations in the produced wires
3- Even when the function of $(1-x^2)\Phi(x,\mu'/\mu)$ has not clear maximum when it was plotted as a function of *x*, the produced wire had been broken up periodically at a certain λ_{final} when it was investigated under the scanning electron microscope. This can push the work to produce 3D metamaterials. One can also use these value of the wavelength of the perturbation at the breaking point λ_{final} to find the original wavelength of the perturbation λ_o at the preform. It appears here to be 1 nm, which is about the roughness of atomic structure and infer limits to wire dimensions that can be achieved using the chosen material system (PMMA and indium)
4- Wire metamaterials can be used to guide the electromagnetic wave in deep sub-wavelength by manipulating the unit cell. The present work doesn't consider the macroscopic effect. It's applicable to waveguide 40cm wavelength in about 2.4 cm waveguide.

3.10 Suggestions for future work

1- Modeling the drawing process to record the profile shape for the neckdown in the different drawing conditions. By using the using the instability model presented here one can directly expect the fluctuations in the produced wires.

2- Investigate the instability with different materials combinations such as soft glass instead of PMMA

3- Continue drawing in sub μm with certain condition to produce indium nano-particle's.

4- Studying the possibility of produce more complex configuration such as add drop filter using the unit cell manipulation and experimentally verification for the produced system.

5- Simulation of subwavelength waveguide inside wire metamaterials in the range of photonic applications.

References

[1] C. C. Lee, *The Current Trends Of Optics And Photonics*. Springer, 2015, p. 542.

[2] S. Zhong, Y. Ma, and S. He, "Perfect absorption in ultrathin anisotropic ε-near-zero metamaterials," *Appl. Phys. Lett.*, vol. 105, no. 2, p. 023504, Jul. 2014.

[3] D. R. Smith and N. Kroll, "Negative refractive index in left-handed materials.," *Phys. Rev. Lett.*, vol. 85, no. 3, pp. 2933–2936, 2000.

[4] J. Yao, Z. Liu, Y. Liu, Y. Wang, C. Sun, G. Bartal, A. M. Stacy, and X. Zhang, "Optical negative refraction in bulk metamaterials of nanowires.," *Science*, vol. 321, no. August, p. 930, 2008.

[5] T. Xu, A. Agrawal, M. Abashin, K. J. Chau, and H. J. Lezec, "All-angle negative refraction and active flat lensing of ultraviolet light.," *Nature*, vol. 497, no. 7450, pp. 470–4, 2013.

[6] S. Fleming, A. Tuniz, A. Argyros, and B. T. Kuhlmey, "Metamaterials Drawn in fibers," in *European Conference and Exhibition on Optical Communication*, 2012, p. Mo.2.F.5.

[7] O. T. Naman, M. R. New-Tolley, R. Lwin, A. Tuniz, A. H. Al-Janabi, I. Karatchevtseva, S. C. Fleming, B. T. Kuhlmey, and A. Argyros, "Indefinite Media Based on Wire Array Metamaterials for the THz and Mid-IR," *Adv. Opt. Mater.*, vol. 1, no. 12, pp. 971–977, Dec. 2013.

[8] S. Tomotika, "Breaking up of a Drop of Viscous Liquid Immersed in Another Viscous Fluid Which is Extending at a Uniform Rate," *Proc. R. Soc. Ser. A, Math. Phys.*, vol. 153, no. 879, pp. 302–318, 1936.

[9] R. D. M. John D. Joannopoulos, Steven G. Johnson, Joshua N. Winn, *Photonic Crystals: Molding the Flow of Light*, 2nd Editio. New Jersey, USA: Princeton University Press, 2008.

[10] N. D. Ashcroft, NeilW. and Mermin, *Solid state physics*, First. Orlando, FL: Saunders College Publishing, 1976.

[11] W. Cai and V. M. Shalaev, *Optical Metamaterials: Fundamentals and Applications*. Springer Science, 2010.

[12] R. C. Mcphedran, I. V Shadrivov, B. T. Kuhlmey, and Y. S. Kivshar, “Metamaterials and metaoptics,” *NPG Asia Mater.*, vol. 3, pp. 100–108, 2011.

[13] V. M. Shalaev, “Talk at 1st Metamaterials Congress, Purdue Univ,” 2007.

[14] Jackson and J. D., *Classical Electrodynamics*, 3rd Editio. New York, USA: John Wiley & Sons, Inc., 1999.

[15] K. Gangwar and R. P. S. Gangwar, “Metamaterials : Characteristics , Process and Applications,” *Adv. Electron. Electr. Eng.*, vol. 4, no. 1, pp. 97–106, 2014.

[16] J. Pendry, “Negative Refraction and Metamaterials,” *Opt. Express*, vol. 11, no. 7, p. 639, Apr. 2003.

[17] G. Thompson, “Unusual Waveguide Characteristics associated with the Apparent Negative Permeability obtainable in Ferrites,” *Nature*, vol. 175, no. 4469, pp. 1135–1136, Jun. 1955.

[18] J. Brown, “Artificial dielectrics having refractive indices less than unity,” *Proc. IEE - Part IV Inst. Monogr.*, vol. 100, no. 5, pp. 51–62, Oct. 1953.

[19] J. Brown and W. Jackson, “The properties of artificial dielectrics at centimetre wavelengths,” *Proc. IEE - Part B Radio Electron. Eng.*, vol. 102, no. 1, pp. 11–16, Jan. 1955.

[20] A. Carne and J. Brown, “Theory of reflections from the rodded-type artificial dielectric,” *Proc. IEE - Part B Radio Electron. Eng.*, vol. 106, no. 26, pp. 107–114, Mar. 1959.

[21] R. King, D. Thiel, and K. Park, “The synthesis of surface reactance using an artificial dielectric,” *IEEE Trans. Antennas Propag.*, vol. 31, no. 3, pp. 471–476, May 1983.

[22] C. R. Simovski, P. a Belov, A. V Atrashchenko, and Y. S. Kivshar, “Wire metamaterials: physics and applications.,” *Adv. Mater.*, vol. 24, no. 31, pp. 4229–48, Aug. 2012.

[23] D. Smith, W. Padilla, D. Vier, S. Nemat-Nasser, and S. Schultz, “Composite medium with simultaneously negative permeability and permittivity,” *Phys. Rev. Lett.*, vol. 84, no. 18, pp. 4184–7, May 2000.

[24] S. Tretyakov, *Analytical Modeling in Applied Electromagnetics*. Boston, MA London: Artech House, 2003.

[25] S. I. M. N. P.A. Belov, R.Marques, “Strong spatial dispersion in wire media in the very large wavelength limit,” *Phys. Rev. B*, vol. 76, 2003.

[26] P. J., H. A., and Y. I, “Extremely Low Frequency Plasmons in metallic microstructure,” *Phys Rev Lett.*, vol. 6, pp. 1–12, 1996.

[27] P. A. Belov, S. A. Tretyakov, and A. J. Viitanen, “Dispersion and Reflection Properties of Artificial Media Formed By Regular Lattices of Ideally Conducting Wires,” *J. Electromagn. Waves Appl.*, vol. 16, no. 8, pp. 1153–1170, Jan. 2002.

[28] S. I. Maslovski, S. A. Tretyakov, and P. A. Belov, “Wire media with negative effective permittivity: A quasi-static model,” *Microw. Opt. Technol. Lett.*, vol. 35, no. 1, pp. 47–51, Oct. 2002.

[29] F. Capolino, *Theory and Phenomena of Metamaterials*. Broken Sound Parkway: Taylor & Francis, 2009.

[30] I. D. Rukhlenko, P. a. Belov, and Litchinitser, “Modern trends in metamaterial applications,” *Adv. Optoelectron.*, vol. 2012, 2012.

[31] G. S. Turkmen, Oznur and R. W. Ziolkowski, “Single Dual and Triple band metamaterial-inspired electrically small planar magnetic dipole antennas.,” *Microw. Opt. Technol. Lett.*, vol. 56, no. 1, pp. 286–289, 2014.

[32] F. Zhu and J. Hu, “Improved patch antenna performance by using a metamaterial cover,” *J. Zhejiang Univ. Sci. A*, vol. 8, no. 2, pp. 192–196, Feb. 2007.

[33] M. Rahman, C. Mahdy, and R. A. Zuboraj, “Novel Application of MNG Metamaterial in Rectangular Microstrip Patch Antenna (Partially Loaded Case) for Dual Band Application,” in *Progress In Electromagnetics Research Symposium Proceedings*, 2011, pp. 935–938.

[34] A. Tomaz, J. J. Barroso, U. C. Hasar, and A. J. F. Orlando, “Directivity Enhancement of an X-band Horn Antenna Loaded by a Wire Medium,” in *PIERS Proceedings, Stockholm, Sweden*, 2013, vol. 1, no. 2, pp. 1128–1131.

[35] T. Chen, S. Li, and H. Sun, “Metamaterials application in sensing.,” *Sensors*, vol. 12, no. 3, pp. 2742–65, Jan. 2012.

[36] A. Remley, K.A., Weisshaar, “Design and analysis of a silicon-based antiresonant reflecting optical waveguide chemical sensor,” *Opt. Lett.*, vol. 21, no. 16, p. Pages 1241–1243, 1996.

[37] L. D. Jing Jing Yang, Ming Huang, Hao Tang, Jia Zeng, “Metamaterial Sensors,” *Int. J. Antennas Propag.*, vol. 2013, 2013.

[38] J. F. O’Hara, R. Singh, I. Brener, E. Smirnova, J. Han, A. J. Taylor, and W. Zhang, “Thin-film sensing with planar terahertz metamaterials: sensitivity and limitations,” *Opt. Express*, vol. 16, no. 3, p. 1786, 2008.

[39] W. Withayachumnankul, K. Jaruwongrungsee, C. Fumeaux, and D. Abbott, “Metamaterial-Inspired Multichannel Thin-Film Sensor,” *IEEE Sens. J.*, vol. 12, no. 5, pp. 1455–1458, May 2012.

[40] J. Y. Ou, E. Plum, L. Jiang, and N. I. Zheludev, “Reconfigurable photonic metamaterials.,” *Nano Lett.*, vol. 11, no. 5, pp. 2142–4, May 2011.

[41] S. Jindal and J. Sharma, “Review of Metamaterials in Microstrip Technology for Filter Applications,” *Int. J. Comput. Appl.*, vol. 54, no. 3, pp. 48–54, 2012.

[42] K. Chang, *Encyclopedia of RF and Microwave Engineering*. NJ, USA: Wiley & Sons, Inc., 2005.

[43] M. Gil, J. Bonache, and F. Martín, “Metamaterial filters: A review,” *Metamaterials*, vol. 2, no. 4, pp. 186–197, Dec. 2008.

[44] M. Gil, I. Gil, J. Bonache, J. García-García, and F. Martín, “Metamaterial transmission lines with extreme impedance values,” *Microw. Opt. Technol. Lett.*, vol. 48, no. 12, pp. 2499–2506, Dec. 2006.

[45] L. Jiusheng and D. Tieying, “Application of metamaterial unit cell in bandpass filter,” *Microw. Opt. Technol. Lett.*, vol. 49, no. 9, pp. 2109–2111, Sep. 2007.

[46] N. Benmostefa, M. Meliani, and H. Ouslimani, “Metamaterial Tunable Filter Design,” *J. Electromagn. Anal. Appl.*, vol. 05, no. 06, pp. 250–254, Jun. 2013.

[47] C. H. Gan and P. Lalanne, “Well-confined surface plasmon polaritons for sensing applications in the near-infrared.,” *Opt. Lett.*, vol. 35, no. 4, pp. 610–2, Feb. 2010.

[48] Z. Shi, G. Piredda, A. C. Liapis, M. A. Nelson, L. Novotny, and R. W. Boyd, “Surface-plasmon polaritons on metal-dielectric nanocomposite films.,” *Opt. Lett.*, vol. 34, no. 22, pp. 3535–7, Nov. 2009.

[49] A. Govyadinov and V. Podolskiy, “Metamaterial photonic funnels for subdiffraction light compression and propagation,” *Phys. Rev. B*, vol. 73, no. 15, p. 155108, Apr. 2006.

[50] W. T. Lu and S. Sridhar, “Slow light, open-cavity formation, and large longitudinal electric field on a slab waveguide made of indefinite permittivity metamaterials,” *Phys. Rev. A*, vol. 82, no. 1, p. 013811, Jul. 2010.

[51] Y. Huang, W. Lu, and S. Sridhar, “Nanowire waveguide made from extremely anisotropic metamaterials,” *Phys. Rev. A*, vol. 77, no. 6, p. 063836, Jun. 2008.

[52] M. Yan, L. Thylén, and M. Qiu, “Layered metal-dielectric waveguide: subwavelength guidance, leveraged modulation sensitivity in mode index, and reversed mode ordering.,” *Opt. Express*, vol. 19, no. 4, pp. 3818–24, Feb. 2011.

[53] E. Yablonovitch, T. Gmitter, and K. Leung, “Photonic band structure: The face-centered-cubic case employing nonspherical atoms,” *Phys. Rev. Lett.*, vol. 67, no. 17, pp. 2295–2298, Oct. 1991.

[54] A. A. Raad S. Fyath, “Performance Investigation of Photonic Crystal-Based Microring Resonator for Optical Signal Processing,” *Fiber Integr. Opt.*, vol. 28, no. 5, 2009.

[55] M. S. A. A. Ghaffari, F. Monifi, M. Djavid, “Analysis of photonic crystal power splitters with different configurations,” *J. Appl. Sci.*, vol. 8, no. 8, pp. 16–1425, 2008.

[56] G. Manzacca, D. Paciotti, A. Marchese, M. S. Moreolo, and G. Cincotti, “2D photonic crystal cavity-based WDM multiplexer,” *Photonics Nanostructures - Fundam. Appl.*, vol. 5, no. 4, pp. 164–170, Nov. 2007.

[57] T. T. Shih, Y. D. Wu, and J. J. Lee, “Proposal for Compact Optical Triplexer Filter Using 2-D Photonic Crystals,” *IEEE Photonics Technol. Lett.*, vol. 21, no. 1, pp. 18–20, Jan. 2009.

[58] Q. Wang, Y. Cui, J. Zhang, C. Yan, and L. Zhang, “The position independence of heterostructure coupled waveguides in photonic-crystal switch,” *Opt. - Int. J. Light Electron Opt.*, vol. 121, no. 8, pp. 684–688, Apr. 2010.

[59] P. Kanakis, T. Kamalakis, and T. Sphicopoulos, “Designing slow-light photonic crystal waveguides for four-wave mixing applications.,” *Opt. Lett.*, vol. 39, no. 4, pp. 884–7, Feb. 2014.

[60] S. Arezoomandan, K. Yang, and B. Sensale-Rodriguez, “Graphene-based electrically reconfigurable deep-subwavelength metamaterials for active control of THz light propagation,” *Appl. Phys. A*, vol. 117, no. 2, pp. 423–426, Aug. 2014.

[61] B. A. Slovick, Z. G. Yu, and S. Krishnamurthy, “Generalized effective-medium theory for metamaterials,” *Phys. Rev. B*, vol. 89, no. 15, p. 155118, Apr. 2014.

[62] F. Lemoult, N. Kaina, M. Fink, and G. Lerosey, “Wave propagation control at the deep subwavelength scale in metamaterials,” *Nat. Phys.*, vol. 9, no. 1, pp. 55–60, Nov. 2012.

[63] A. Boltasseva and V. M. Shalaev, “Fabrication of optical negative-index metamaterials : Recent advances and outlook,” *Metamaterials*, vol. 2, no. 1, pp. 1–17, 2008.

[64] A. Argyros, “Microstructures in Polymer Fibres for Optical Fibres, THz Waveguides, and Fibre-Based Metamaterials - Open Access Library.” [Online]. Available: http://www.oalib.com/paper/2813112#.U_EI7mPFNDQ. [Accessed: 17-Aug-2014].

[65] G. Dolling, C. Enkrich, M. Wegener, C. M. Soukoulis, and S. Linden, “Low-loss negative-index metamaterial at telecommunication wavelengths,” *Opt. Lett.*, vol. 31, no. 12, p. 1800, 2006.

[66] U. K. Chettiar, A. V. Kildishev, H.-K. Yuan, W. Cai, S. Xiao, V. P. Drachev, and V. M. Shalaev, “Dual-band negative index metamaterial: double negative at 813 nm and single negative at 772 nm,” *Opt. Lett.*, vol. 32, no. 12, p. 1671, 2007.

[67] T. Tomioka, S. Kubo, M. Nakagawa, M. Hoga, and T. Tanaka, “Split-ring resonators interacting with a magnetic field at visible frequencies,” *Appl. Phys. Lett.*, vol. 103, no. 7, p. 071104, Aug. 2013.

[68] L. J. Guo, “Nanoimprint Lithography: Methods and Material Requirements,” *Adv. Mater.*, vol. 19, no. 4, pp. 495–513, Feb. 2007.

[69] C. M. Soukoulis and M. Wegener, “Past Achievements and Future Challenges in 3D Photonic Metamaterials,” *Nat. Phot.*, vol. 5, pp. 523–530, 2011.

[70] J. K. Gansel, M. Thiel, M. S. Rill, M. Decker, K. Bade, V. Saile, G. von Freymann, S. Linden, and M. Wegener, “Gold helix photonic metamaterial as broadband circular polarizer.,” *Science*, vol. 325, no. 5947, pp. 1513–5, Sep. 2009.

[71] M. L. Tseng, P. C. Wu, S. Sun, C. M. Chang, W. T. Chen, C. H. Chu, P. Chen, L. Zhou, D. Huang, and T. Yen, “Fabrication of multilayer metamaterials by femtosecond laser-induced forward-

transfer technique," *Laser photonics Rev*, vol. 6, no. 5, pp. 702–707, 2012.

[72] G. W. B. M. A. van Poladian, Maryanne C. J. Large Leon, Eijkelenborg, *Microstructured Polymer Optical Fibres*. New York, USA: Springer Science and Business Media, LLC, 2008.

[73] "Max Planck Institute for the Science of Light, Photonic Crystal Fibre Science." [Online]. Available: http://www.mpl.mpg.de/en/russell/research/topics/fabrication.html.

[74] A. F. Abouraddy, M. Bayindir, G. Benoit, S. D. Hart, K. Kuriki, N. Orf, O. Shapira, F. Sorin, B. Temelkuran, and Y. Fink, "Towards multimaterial multifunctional fibres that see, hear, sense and communicate.," *Nat. Mater.*, vol. 6, no. 5, pp. 336–47, May 2007.

[75] M. Bayindir, F. Sorin, A. F. Abouraddy, J. Viens, S. D. Hart, J. D. Joannopoulos, and Y. Fink, "Metal-insulator-semiconductor optoelectronic fibres.," *Nature*, vol. 431, no. 7010, pp. 826–9, Oct. 2004.

[76] A. Mazhorova, J. F. Gu, A. Dupuis, M. Peccianti, O. Tsuneyuki, R. Morandotti, H. Minamide, M. Tang, Y. Wang, H. Ito, and M. Skorobogatiy, "Composite THz materials using aligned metallic and semiconductor microwires, experiments and interpretation.," *Opt. Express*, vol. 18, no. 24, pp. 24632–47, Nov. 2010.

[77] M. Bayindir, A. F. Abouraddy, O. Shapira, J. Viens, D. Saygin-Hinczewski, F. Sorin, J. Arnold, J. D. Joannopoulos, and Y. Fink, "Kilometer-Long Ordered Nanophotonic Devices by Preform-to-Fiber Fabrication," *IEEE J. Sel. Top. Quantum Electron.*, vol. 12, no. 6, pp. 1202–1213, Nov. 2006.

[78] G. Tao and A. F. Abouraddy, "Multimaterial fibers: a new concept in infrared fiber optics," in *SPIE Sensing Technology + Applications*, 2014, p. 90980V.

[79] C. C. C. Ricciar, *Lab-on-Fiber Technology*. Springer, 2015.

[80] B. Temelkuran, S. D. Hart, G. Benoit, J. D. Joannopoulos, and Y. Fink, "Wavelength-scalable hollow optical fibres with large

photonic bandgaps for CO2 laser transmission.," *Nature*, vol. 420, no. 6916, pp. 650–3, Dec. 2002.

[81] X. Zhang, Z. Ma, Z.-Y. Yuan, and M. Su, "Mass-Productions of Vertically Aligned Extremely Long Metallic Micro/Nanowires Using Fiber Drawing Nanomanufacturing," *Adv. Mater.*, vol. 20, no. 7, pp. 1310–1314, Apr. 2008.

[82] A. Tuniz, R. Lwin, A. Argyros, S. C. Fleming, E. M. Pogson, E. Constable, R. A. Lewis, and B. T. Kuhlmey, "Stacked-and-drawn metamaterials with magnetic resonances in the terahertz range.," *Opt. Express*, vol. 19, no. 17, pp. 16480–90, Aug. 2011.

[83] E. Badinter, A. Ioisher, E. Monaico, V. Postolache, and I. M. Tiginyanu, "Exceptional integration of metal or semimetal nanowires in human-hair-like glass fiber," *Mater. Lett.*, vol. 64, no. 17, pp. 1902–1904, Sep. 2010.

[84] A. Tuniz, B. T. Kuhlmey, R. Lwin, A. Wang, J. Anthony, R. Leonhardt, and S. C. Fleming, "Drawn metamaterials with plasmonic response at terahertz frequencies," *Appl. Phys. Lett.*, vol. 96, no. 19, p. 191101, May 2010.

[85] A. Tuniz, B. T. Kuhlmey, P. Y. Chen, and S. C. Fleming, "Weaving the invisible thread: design of an optically invisible metamaterial fibre.," *Opt. Express*, vol. 18, no. 17, pp. 18095–105, Aug. 2010.

[86] A. Wang, A. Tuniz, P. G. Hunt, E. M. Pogson, R. A. Lewis, A. Bendavid, S. C. Fleming, B. T. Kuhlmey, and M. C. J. Large, "Fiber metamaterials with negative magnetic permeability in the terahertz," *Opt. Mater. Express*, vol. 1, no. 1, p. 115, Apr. 2011.

[87] A. Tuniz, K. J. Kaltenecker, B. M. Fischer, M. Walther, S. C. Fleming, A. Argyros, and B. T. Kuhlmey, "Metamaterial fibres for subdiffraction imaging and focusing at terahertz frequencies over optically long distances.," *Nat. Commun.*, vol. 4, p. 2706, Jan. 2013.

[88] J. F. Gu, S. Gorgutsa, and M. Skorobogatiy, “Soft capacitor fibers using conductive polymers for electronic textiles,” *Smart Mater. Struct.*, vol. 19, no. 11, p. 115006, Nov. 2010.

[89] Y. D. J. F. Agassant, “An overview of molten polymer drawing instabilities,” *Int. Polym. Process.*, vol. 29, no. 1, pp. 128–139, 2014.

[90] D. S. Deng, J.-C. Nave, X. Liang, S. G. Johnson, and Y. Fink, “Exploration of in-fiber nanostructures from capillary instability.,” *Opt. Express*, vol. 19, no. 17, pp. 16273–90, Aug. 2011.

[91] M. M. Denn, “Continuous Drawing of Liquids to Form Fibers,” *Annu. Rev. Fluid Mech.*, vol. 12, no. 1, pp. 365–387, Jan. 1980.

[92] J. J. WYLIE, H. HUANG, and R. M. MIURA, “Thermal instability in drawing viscous threads,” *J. Fluid Mech.*, vol. 570, pp. 1–16, Jan. 2007.

[93] A. V. Neimark, “Thermodynamic equilibrium and stability of liquid films and droplets on fibers,” *J. Adhes. Sci. Technol.*, vol. 13, no. 10, pp. 1137–1154, Jan. 1999.

[94] A. L. Yarin, A. Oron, and P. Rosenau, “Capillary instability of thin liquid film on a cylinder,” *Phys. Fluids A Fluid Dyn.*, vol. 5, no. 1, pp. 91–98, Jan. 1993.

[95] J. S. Plateau, “Experimentale et Theorique des Liquids Soumis aux Seules Forces Moleculaire,” *Gauthiers-Villars*, vol. 2, 1873.

[96] Lord Rayleigh, “On the instability of a cylinder of viscous liquid under capillary force,” *Philos. Mag. Ser. 5*, vol. 34, no. 207, pp. 145–154, Aug. 1892.

[97] S. Tomotika, “On the instability of a cylindrical thread of viscous liquid surrounded by another viscous fluid,” *Proc. R. Soc. Ser. A, Math. Phys.*, vol. 153, p. 322−337, 1935.

[98] S. Shabahang, J. J. Kaufman, D. S. Deng, and a. F. Abouraddy, “Observation of the Plateau-Rayleigh capillary instability in multi-material optical fibers,” *Appl. Phys. Lett.*, vol. 99, no. 16, p. 161909, 2011.

[99] S. Danto, Z. Ruff, Z. Wang, J. D. Joannopoulos, and Y. Fink, "Ovonic Memory Switching in Multimaterial Fibers," *Adv. Funct. Mater.*, vol. 21, no. 6, pp. 1095–1101, Mar. 2011.

[100] "Indium Corporation." [Online]. Available: http://www.indium.com/products/indiummetal/physicalconstants.php.

[101] "Private communication with IPOS group (Dr. Ritchard), The Sydney University."

[102] T. W. Chapman, "The viscosity of liquid metals," *AIChE J.*, vol. 12, no. 2, pp. 395–400, Mar. 1966.

[103] D. W. G. White, "The surface tensions of indium and cadmium," *Metall. Trans.*, vol. 3, no. 7, pp. 1933–1936, Jul. 1972.

[104] F. Lemoult, M. Fink, and G. Lerosey, "Dispersion in media containing resonant inclusions: Where does it come from?," in *Quantum Electronics and Laser Science Conference,San Jose, California United States*, 2012, pp. 1–2.

Appendix

a- Flowchart for the program

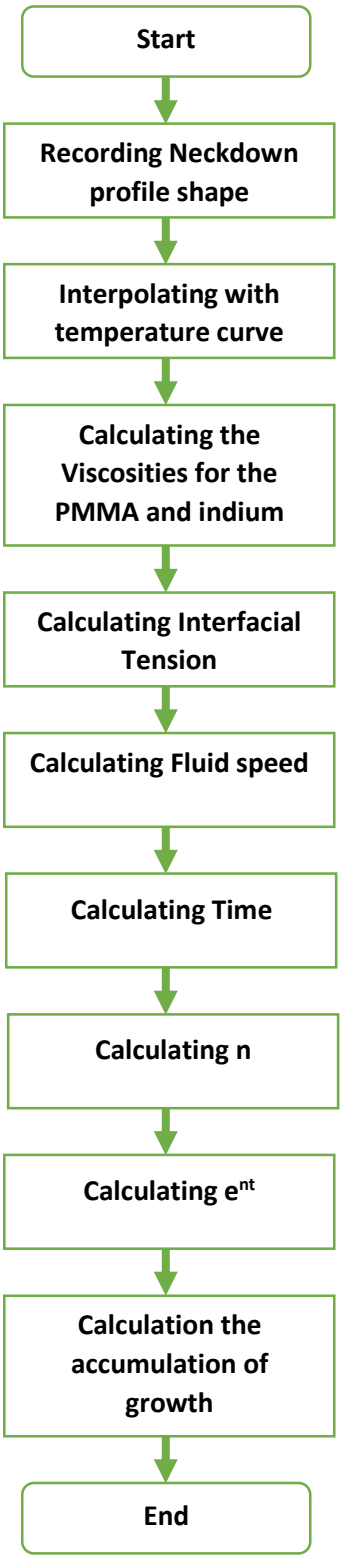

b- Matlab code for the modeling of the growth of the instability

```
clear

clc
% get data for lambdqa observed in 1000
LL = xlsread('SEM1000 flactuation.xls','1000')
LL(isnan(LL))=0
 % get the data for temp distribution along the length for Different conditions T=180,
 T=190 at two speeds)
p = xlsread('tempo.xlsx','tempr')
p(isnan(p))=0
pos180at2  =nonzeros (p(:,1));
temp180at2 =nonzeros (p(:,2));
pos180at4  =nonzeros (p(:,3));
temp180at4 =nonzeros (p(:,4));
pos190at2  =nonzeros (p(:,5));
temp190at2 =nonzeros (p(:,6));
pos190at4  =nonzeros (p(:,7));
temp190at4 =nonzeros (p(:,8));
% read the data of distance from top iris(mm) and the diameter(mm)in general case
model = xlsread('Neckdown dimensions.xlsx','1000mod');
model(isnan(model))=0;
Disg =nonzeros (model(:,1));
DPMMAg =nonzeros (model(:,2));
%input the velocity of the fluid at the first point (feeding velocity)=U1(m/s)
U1=(4/60000)
pos=pos190at4/1000     % change to m
temp=temp190at4        % in C
Dis  =Disg/1000;       % change to m
DPMMA =DPMMAg/1000000;    % change to m
[q,w]=size (Dis);
% ratio of Indium diameter to PMMA diameter
 R=((5.7)/6300)
 lam =[0:1*10^-4:1*10^-1];
f=1001;
for j=1:f
   lambda(1,j)=lam(j);
end

for j=1:f

for i=2:q
   lambda(i,j)=((DPMMA(i-1)/DPMMA(i))^2)*lambda(i-1,j);
end
end
for j=1:f
```

```
% calculation of U2(m/s) as well as average velocity Um(m/s)
U2(1)=((DPMMA(1))^2*U1)/(DPMMA(2))^2;
Um(1)=(U1+U2(1))/2;
for i=2:q-1
U2(i)=((DPMMA(i))^2*U2(i-1))/(DPMMA(i+1))^2;
Um(i)=(U2(i-1)+U2(i))/2;
end
%calculation of temperature for each position = T(K)
for i=1:q;
Tc(i)=interp1(pos,temp,Dis(i),'linear','extrap');
T(i)=Tc(i)+273;
end
% calculation of the viscosity of the PMMA at each point Vis(Pa.s)
for i=1:q
Vis(i)=(3.802*10^-14)*(exp((2.027*10^4)/T(i)));
end
% calculation of the viscosity of the indium at each point Vis(Pa.s)
for i=1:q
VisInd(i)= 0.000302*exp(800/T(i));
end
% calculation of the viscosity Ratio
for i=1:q
Rat(i)= VisInd(i)/Vis(i);
end
% calculation of distances between each two points= Diff(m).
for i=1:q-1
   Diff(i)=Dis(i+1)-Dis(i);
end
TT(1)=0
% calculation of time spend between two positions= Tim(s)
for i=1:q-1
Tim(i)=(Diff(i)/Um(i));
TT(i+1)=TT(i)+Tim(i)
end
Time=TT(1:q-1);
% calculation of surface tension= ST(N/m)
for i=1:q
ST(i)=(0.546)-((9 *10^-5)*(T(i)));
End

% calculation on (1-x^2)* phi(x)value where x=KR
for i=1:q
x(i,j)=(pi*DPMMA(i)*R(i))/lambda(i,j);
I0(i,j)= besseli(0,x(i,j));
I1(i,j)= besseli(1,x(i,j));
K0(i,j)= besselk(0,x(i,j));
K1(i,j)= besselk(1,x(i,j));
```

```
d1(i,j) = det([(x(i,j)*I0(i,j)-I1(i,j)) K1(i,j) (-x(i,j)*K0(i,j)-K1(i,j));I0(i,j)+x(i,j)*I1(i,j)
-K0(i,j) (-K0(i,j)+x(i,j)*K1(i,j));Rat(i)*x(i,j)*I0(i,j) K1(i,j) -x(i,j)*K0(i,j)]);
d2(i,j) = det([I1(i,j) K1(i,j) -x(i,j)*K0(i,j)-K1(i,j);I0(i,j) -K0(i,j) -
K0(i,j)+x(i,j)*K1(i,j); Rat(i)*I1(i,j) K1(i,j) -x(i,j)*K0(i,j)]);
d3(i,j) = det([I1(i,j) x(i,j)*I0(i,j)-I1(i,j) -x(i,j)*K0(i,j)-K1(i,j);I0(i,j)
I0(i,j)+x(i,j)*I1(i,j) -K0(i,j)+x(i,j)*K1(i,j);Rat(i)*I1(i,j) Rat(i)*x(i,j)*I0(i,j) -
x(i,j)*K0(i,j)]);
d4(i,j) = det([I1(i,j) x(i,j)*I0(i,j)-I1(i,j) K1(i,j);I0(i,j) I0(i,j)+x(i,j)*I1(i,j) -
K0(i,j);Rat(i)*I1(i,j) Rat(i)*x(i,j)*I0(i,j) K1(i,j)]);
N(i,j) = I1(i,j)*d1(i,j)-(x(i,j)*I0(i,j)-I1(i,j))*d2(i,j);
D(i,j) = Rat(i)*(x(i,j)*I0(i,j)-I1(i,j))*d1(i,j)-Rat(i)*((x(i,j)^2+1)*I1(i,j)-
x(i,j)*I0(i,j))*d2(i,j)-(x(i,j)*K0(i,j)+K1(i,j))*d3(i,j)-
((x(i,j)^2+1)*K1(i,j)+x(i,j)*K0(i,j))*d4(i,j);
phi(i,j)=N(i,j)/D(i,j);
O(i,j)=(1-x(i,j)^2)*phi(i,j);
if x(i,j)>1;O(i,j)=0;
end
end
% calculation of n(1/s) with and without (1-x^2)phi(u/u') term.
%Here we multiply DPMMA by R to get Indium   diameter=DInd(m)
% also the calculation of exp (nt)
%e1 with and e2 without considering the (1-x^2)phi(u/u') term
for i=1:q-1;
   DInd(i)=DPMMA(i+1)*R(i);


n1(i,j)=O(i+1,j);% we increase 1 since the n is calculated at first for the second point


n2(i)= (ST(i+1))/(DInd(i)*Vis(i+1));
e1(i,j)=exp(n1(i,j)*Tim(i));
e2(i)=exp(n2(i)*Tim(i));
e3(i,j)=exp(n1(i,j)*n2(i)*Tim(i));
end
% calculations of accumulation of exp(nt)
acce1(1,j)=e1(1,j);
acce2(1)=e2(1);
acce3(1,j)=e3(1,j);
for i=2:q-1;
acce1(i,j)=e1(i,j)*acce1(i-1,j);
acce2(i)=e2(i)*acce2(i-1);
acce3(i,j)=e3(i,j)*acce3(i-1,j);
end
%change the dimension of the distance to fit with the dimensions of n,exp(nt), acce
Diss=Dis(1:q-1);
DPMMAA=DPMMA(1:q-1);
Time=TT(1:q-1);
end
```

```
[maxi,i]=max(acce3(q-1,:))
a=lambda(q,i)
b=lam(i)

figure(1)
plot (lambda(q,:),acce3(q-1,:),a,acce3(q-1,:)) % for the lmabda_end
ylabel('accumlated Exp(nt)','FontSize',12,'FontWeight','bold')
xlabel('\lambda final(m)','FontSize',12,'FontWeight','bold')
%xlim([0 .5])

figure(2)
plot (lam,acce3(q-1,:),b,acce3(q-1,:)) % for the lmabda_0
ylabel('accumlated Exp(nt)','FontSize',12,'FontWeight','bold')
xlabel('\lambda_0 (m)','FontSize',12,'FontWeight','bold')


lamf3=lambda(q,:)
acc3=acce3(q-1,:)
save ('3.mat','lamf3','acc3')
```

الخلاصة

اشباه المواد هي مواد مركبه اصطناعية ذات تركيب يجعلها تظهر خصائص لا توجد عادة في المواد الطبيعية. استخدمت طريقة سحب الالياف في إنتاج اشباه مواد من بوليمر الميتاكريليت بولي ميثيل (PMMA) وأسلاك الانديوم .PMMA والإنديوم لهما نفس درجة حرارة الانصهار نسبيا مما يجعلهما مناسبان للسحب معا. يجب سحب خيوط الألياف إلى أقطار أصغرللحصول على استجابه بتردد اعلى. في هذه الأبعاد تصبح الخيوط المعدنية داخل الألياف غير مستقرة وتتقطع بمسافات عشوائية. ويرجع هذا عدم الاستقرار الى ظاهرة تعرف باسم عدم الاستقرار لبلاتو-رايلي.

تم تعديل النموذج المعروف ل Tomotika للنمو في الانتفاخات في سطح السائل يمتد داخل سائل آخر لوصف الاضطرابات (عدم الاستقرار) في اقطار اسلاك اشباه المواد المسحوبة داخل الفرن الإشعاعي. نموذج Tomotika المعدل تم استخدامه لدراسة زيادة عدم الاستقرار لقطر سلك الإنديوم المسحوب داخل بوليمرال PMMA.

المعلم الاساسي لتقطع السلك هو الطول الموجي للاضطرابات. تم بناء نموذج ببرنامج ال MATLAB لوصف السحب بنسبة صغيرة (إهمال تأثير الطول الموجي للاضطراب). النتائج التجريبية والنمذجة تتطابق تقريبا عند حدوث اختلاف صغير جدا في درجة الحرارة. وبالتالي فإن الاختلافات التي لوحظت في اقطارالاسلاك يمكن تفسيرها بعدم استقراريه بلاتو-رايلي.

للتقلبات الكبيرة (نسبة السحب كبير) تم تحليل الطول الموجي للتقلبات ولوحظ تتقطع متتالي باطوال مختلفة. تم استدلال حدود اقطار السلك التي يمكن الحصول عليها باستخدام المواد المذكورة وتحديد مسار لتوسيع طرق السحب لصنع اسلاك بقطر اصغر

وأخيرا، تم إجراء محاكاة انتشار الموجات بابعاد باجزاء الطول الموجي داخل اسلاك من اشباه المواد اعتمادا على التلاعب بوحدة الخلية. تم استخدام برنامج استوديو الميكروويف لمحاكاة انتشار الموجات داخل الموجهات الخطية والزاوية 90° ، وكذلك داخل مقسم شعاع متساوي الاذرع (50/50). بدت امكانية توجيه موجه ذات طول موجي 40سم داخل موجه بعرض حوالي 2.4 سم

وزارة التعليم العالي والبحث العلمي
جامعة بغداد
معهد الليزر للدراسات العليا

التحقق من تأثير عدم استقرارية بلاتو-رايلي في عملية سحب ليف شبه المواد انديوم-بوليمر

رسالة مقدمة إلى
معهد الليزر للدراسات العليا
جامعة بغداد
لاستكمال متطلبات نيل درجة
دكتوراه فلسفة في الليزر/ الهندسة الالكترونية والاتصالات

من قبل

احمد عبد الكريم علي
بكلوريوس هندسة الليزر والالكترونيات البصرية 2005
ماجستير هندسة الليزر والالكترونيات البصرية 2008

باشراف
أ.د. عبد الهادي مطشر الجنابي

1436 هـ **2015 م**